

Spectral Properties of Phase Noises and the Impact on the Performance of Optical Interconnects

By

Mustafa AL-QADI

M.Sc., Electronic and Communications Engineering, 2012

B.Sc., Electronic and Communications Engineering, 2008

© Copyright 2019

Submitted to the graduate degree program in the Department of Electrical Engineering and
Computer Science and the Graduate Faculty of the University of Kansas in partial fulfillment of
the requirements for the degree of
Doctor of Philosophy in Electrical Engineering

Chairperson: Dr. Rongqing Hui

Dr. Christopher Allen

Dr. Erik Perrins

Dr. Victor Frost

Dr. Jie Han

Date defended:

The dissertation committee for Mustafa AL-QADI certifies that this is the approved version of the following dissertation:

“Spectral Properties of Phase Noises and the Impact on the Performance of
Optical Interconnects”

Chairperson: Dr. Rongqing Hui

Date approved:

Abstract

The non-ending growth of data traffic resulting from the continuing emergence of Internet applications with high data-rate demands sets huge capacity requirements on optical interconnects and transport networks. This requires the adoption of optical communication technologies that can make the best possible use of the available bandwidths of electronic and electro-optic components to enable data transmission with high spectral efficiency (SE). Therefore, advanced modulation formats are required to be used in conjunction with energy-efficient and cost-effective transceiver schemes, especially for medium- and short-reach applications. Important challenges facing these goals are the stringent requirements on the characteristics of optical components comprising these systems, especially laser sources. Laser phase noise is one of the most important performance-limiting factors in systems with high spectral efficiency. In this research work, we study the effects of the spectral characteristics of laser phase noise on the characterization of lasers and their impact on the performance of digital coherent and self-coherent optical communication schemes. The results of this study show that the commonly-used metric to estimate the impact of laser phase noise on the performance, laser linewidth, is not reliable for all types of lasers. Instead, we propose a Lorentzian-equivalent linewidth as a general characterization parameter for laser phase noise to assess phase noise-related system performance. Practical aspects of determining the proposed parameter are also studied and its accuracy is validated by both numerical and experimental demonstrations. Furthermore, we study the phase noises in quantum-dot mode-locked lasers (QD-MLLs) and assess the feasibility of employing these devices in coherent applications at relatively low symbol rates with high SE. A novel multi-heterodyne scheme for characterizing the phase noise of laser frequency comb sources is also proposed and validated by experimental results with the QD-MLL. This proposed scheme is capable of measuring the differential phase noise between

multiple spectral lines instantaneously by a single measurement. Moreover, we also propose an energy-efficient and cost-effective transmission scheme based on direct detection of field-modulated optical signals with advanced modulation formats, allowing for higher SE compared to the current pulse-amplitude modulation schemes. The proposed system combines the Kramers-Kronig self-coherent receiver technique, with the use of QD-MLLs, to transmit multi-channel optical signals using a single diode laser source without the use of the additional RF or optical components required by traditional techniques. Semi-numerical simulations based on experimentally captured waveforms from practical lasers show that the proposed system can be used even for metro scale applications. Finally, we study the properties of phase and intensity noise changes in unmodulated optical signals passing through saturated semiconductor optical amplifiers for intensity noise reduction. We report, for the first time, on the effect of phase noise enhancement that cannot be assessed or observed by traditional linewidth measurements. We demonstrate the impact of this phase noise enhancement on coherent transmission performance by both semi-numerical simulations and experimental validation.

Acknowledgements

First, I owe a great debt of gratitude to my mentor and advisor Dr. Rongqing Hui for the thoughtful guidance and support he has provided to me throughout the journey towards my Ph.D. He has always been a great source of inspiration in learning and working hard.

Second, I would like to express my sincere thanks to all the professors who have provided me with excellent insight and deeper understanding of the foundational knowledge in the field of communications engineering. Especially, Dr. James Stiles, Dr. Glenn Prescott and Dr. Erik Perrins for their excellent teaching of the related topics in the coursework I have studied at the University of Kansas.

Third, I would also like to thank many colleagues and friends who have helped make the journey more delightful and enjoyable. Without the help of them, I would not have achieved this work in the same way I have.

Fourth and last, but not least, I cannot find words to describe my gratitude to my family for the great encouragement and support that they have always been providing to me.

Table of Contents

Abstract	ii
List of Figures	vii
List of Abbreviations	xi
Chapter 1: Introduction	1
1.1 Motivation and Outline	1
1.2 Evolution of Transmission Technologies in Fiber Optic Communications.....	6
1.3 Background Information	9
1.3.1 Direct vs. Coherent Detection Systems	9
1.3.2 Self-Coherent Optical SSB Modulation and the Kramers-Kronig Receiver	16
1.3.3 Laser Phase and Intensity Noises and their Measurements	24
Chapter 2: Spectral Properties of Phase Noise and the Performance of Digital Coherent Systems	29
2.1 Introduction.....	30
2.2 Laser Phase Noise Characterization.....	31
2.2.1 General Characterization	31
2.2.2 Characterization of Lasers with Non-white FM Noise	33
2.3 Experimental Setup and Laser Phase Noise Measurements	37
2.4 Performance in Digital CPR Algorithms	40
2.4.1 Impact of Non-white FM Noise on Averaging Window Length	45
2.4.2 Phase Estimation Efficiency and Performance Prediction Accuracy	49
2.5 Conclusion	53
Chapter 3: Phase Noises in Quantum-Dot Mode-Locked Multi-Wavelength Light Sources	55
3.1 Introduction.....	56
3.2 Phase Noise Spectral Properties Across Individual Comb Lines in Quantum-Dot Mode-Locked Lasers	57
3.2.1 Experimental Procedure and Device Characterization	57
3.2.2 Performance in Digital Coherent Systems.....	61
3.3 Differential Phase Noise Properties in QD-MLL and its Performance in Coherent Transmission Systems.....	64
3.3.1 Experimental Procedure and DPN Characterization.....	65

3.3.2 Performance of DPN in Digital CPR	67
3.4 Coherent Multi-Heterodyne for Phase Noise Characterization of Frequency Comb Sources	68
3.4.1 Theoretical Background	70
3.4.2 Comb Source Characterization with Multi-Heterodyne Technique	71
3.4.3 Experimental Setup and Results	74
Chapter 4: Optical Comb-Based SSB Superchannel Generation with Kramers-Kronig Reception	89
4.1 Introduction	90
4.2 SSB-Modulated Superchannel Generation	93
4.2.1 The Kramers-Kronig Self-Coherent Scheme	93
4.2.2 The Proposed SSB Superchannel Generation Scheme	95
4.3 Experimental Setup and QD-MLL Characterization	98
4.4 System Performance Semi-Numerical Simulation Results	102
4.5 Conclusions	108
Chapter 5: Phase Noise Enhancement in Saturated SOA used for RIN Reduction	111
5.1 Introduction	111
5.2 Device Modeling and Simulations	113
5.3 Experimental Setup and Results	117
5.4 Conclusion	122
Chapter 6: Proposed Future Work	125
References	127

List of Figures

Fig. 1.1. Generic schematic of (a) direct detection and (b) digital coherent transmission system. OA: optical amplifier.	10
Fig. 1.2. General functional blocks of (a) transmitter and (b) receiver in a PDM digital coherent communication system.....	14
Fig. 1.3. General functional blocks of (a) transmitter and (b) receiver in a self-coherent SSB DD system.	17
Fig. 1.4. Time trajectory on the complex plane for (a) $S(t)$: 16-QAM signal pulse-shaped by a RC filter ($\beta=0.1$); (b), (c), and (d) show $E_{Rx}(t)=E_c+S(t)$ at different values of CSRR.....	22
Fig. 1.5. Block diagram of the receiver DSP with Kramers-Kronig field reconstruction algorithm.	23
Fig. 1.6. RIN measurement of different practical lasers.	25
Fig. 1.7. (a) Time evolution of the phase and (b) the field spectrum of a DFB laser obtained by a coherent receiver.	27
Fig. 1.8. Constellations of a 16-QAM signal at 28 GBd and SNR of 23 dB (a) without and (b) with the effect of phase noise from a laser with a linewidth of 100 kHz.....	28
Fig. 2.1. (a) Simulated FM noise PSDs before (blue) and after (yellow and orange) spectral modifications; and (b) corresponding optical field spectra (each normalized to its maximum PSD).	35
Fig. 2.2. Lorentzian-equivalent linewidths of the phase noise sequences used to obtain Fig. 2.1, (a) without and (b) with the effect of additive instrumentation noise included..	36
Fig. 2.3. Schematic of the experimental setup used for phase noise acquisition..	38
Fig. 2.4. (a) Experimental FM-noise PSD for different lasers, and (b) Lorentzian-equivalent linewidths calculated at different sample interval τ	39
Fig. 2.5. Simulated BER performance for differential 16-QAM at 10 GBd for the measured phase noises and ideal Lorentzian phase noises with (a) BPS and (b) M th-power CPR..	41
Fig. 2.6. Experimental B2B BER performance as a function of OSNR with differential 16-QAM at 5 GBd for the 25GHz-MLL and an ECL at the Tx side..	43
Fig. 2.7. Simulated E_b/N_0 penalty error between the actual performance and the LEL estimates as a function of sampling frequency..	44

Fig. 2.8. Phase estimation mean squared error components for Eqns. (2.7-2.9) evaluated over 10^5 samples for different window lengths.....	47
Fig. 2.9. E_b/N_0 penalty at BER= 10^{-3} for 10 GBd differential 16-QAM for (a) BPS and (b) M th-power CPR.....	49
Fig. 2.10. Phase estimation efficiency η versus averaging window half-length for the BPS and the M th-power CPR for a 16-QAM signal at 10 GBd with SNR=17dB.....	50
Fig. 2.11. SNR penalty and optimum window length versus F_l for differential 16-QAM at 10 GBd with BPS algorithm and initial ideal Lorentzian laser linewidth of (a) 500 kHz and (b) 1 MHz. 52	
Fig. 3.1. (a) Optical spectra of the QD-MLL (RBW=0.01nm) for two different bias and temperature cases, and (b) measured linewidths of 10 different comb lines.....	58
Fig. 3.2. (a) FM-noise PSD of four different comb lines at Case 2 (18°C, 370mA), and (b) corresponding LELs vs. frequency.	60
Fig. 3.3. Schematic of the B2B coherent transmission experimental setup.....	61
Fig. 3.4. (a) Experimental BER vs. OSNR, and (b) experimental R-OSNR at 10^{-3} BER.	62
Fig. 3.5. Simulation setup used to measure the performance at different symbol rates from the measured phase noise waveforms.	63
Fig. 3.6. Semi-numerical simulations of required E_b/N_0 for differential 16-QAM at different system baud.....	64
Fig. 3.7. (a) FM-noise PSD profiles of DPN compared to CMPN and ECLs; and (b) Lorentzian-equivalent linewidths at different sampling frequencies.	66
Fig. 3.8. BER vs. E_b/N_0 for the 11GHz-MLL DPN and ECLs with 16-QAM at 5 GBd and 64-QAM at 10 GBd.	68
Fig. 3.9. (a) Illustration of coherent I/Q mixing between CUT with a repetition frequency F and a LO with a single spectral line. (b) Coherent I/Q mixing between CUT and a reference comb with a repetition frequency $F+\delta f$..	72
Fig. 3.10. (a) Optical spectral density of the QD-MLL measured with 0.01nm resolution bandwidth, and (b) RF spectra of the 1 st and the 2 nd order beating notes and Lorentzian fitting, where the frequency has been shifted by the central frequency f_n ($n = 1, 2$) of each peak.....	75
Fig. 3.11. (a) Example of measured spectrum of heterodyne detection using a tunable external cavity laser as the local oscillator, (b) measured spectral linewidths (square markers) of spectral lines at different wavelengths by tuning the LO wavelength across the window, and parabolic fitting (solid line); inset in (b) is an example of phase noise PSD and -20 dB/decade fitting, and (c) spectral linewidth extracted from the phase of each spectral line in (a) below in multiheterodyne measurement.	77

Fig. 3.12. Experimental setup for multi-heterodyne experiment, where a reference comb is generated by a re-circulating loop resonator.....	79
Fig. 3.13. Measured optical spectra of the comb laser source (blue) plotted together with the reference comb (red) in the 1542.3-1546.5-nm wavelength window.....	80
Fig. 3.14. RF spectra obtained by Fourier transform of (a) $i_I(t) - j i_Q(t)$ and (b) $i_I(t) + j i_Q(t)$	81
Fig. 3.15. Positive-frequency side of the multi-heterodyne RF spectrum, (b) Spectrum obtained after removing the common-mode phase noise using the first spectral line ($m = 1$) as the reference, (c) same as (b) but the 25 th spectral line ($m = 25$) is used as the phase reference.	82
Fig. 3.16. (a) Differential phase $\Delta\phi_{mn}(t)$ of lines 1, 10, 20, 30 and 40 as the function of time with $m = 1$ as the reference line, and (b) differential phase normalized by line separation with the reference line m	83
Fig. 3.17. Same as Fig. 3.16, except that $m = 25$ is chosen as the reference line.	84
Fig. 3.18. FWHM spectral linewidth as the function of the spectral line index for reference line chosen as $m = 1$ (a) and $m = 25$ (b). Examples of spectral line shapes (inset in (a)), and phase noise power spectral densities (insets in (b)) of $n = 2$ (red), 25 (black), and 48 (blue).....	84
Fig. 3.19. Optical phase of spectral lines $n = 5, 10, 20, 30$ and 40 shown in the spectrum of Fig. 3.15(a) without common-mode phase noise cancelation.....	86
Fig. 3.20. Comparison between common-mode phase noise (red) and IDMP noise (black) waveforms.....	87
Fig. 4.1. Schematic of the proposed SSB superchannel transmitter..	96
Fig. 4.2. Ideal transfer function of the 37.5GHz-75GHz asymmetric (30%/70%) de-interleaver used to separate comb lines.....	97
Fig. 4.3. Experimental and simulation setup schematics..	99
Fig. 4.4. (a) Optical spectrum of the 25GHz QD-MLL and linewidth of some selected comb lines, (b) field spectra of two adjacent comb lines from the middle of the comb band with a Lorentzian fitting corresponding to their average linewidth, and their differential phase spectrum, (c) RIN spectral profiles of some selected wavelengths, and (d) simulated OSNR penalty from laser phase noise in 23 GBd 16-QAM KK transmission using the QD-MLL measured phase noise waveforms, compared to using independent lasers with different linewidths.....	101
Fig. 4.5. (a) Spectrum of the generated optical superchannel in simulation, (b) B2B BER performance versus OSNR for different values of CSPR, and (c) required OSNR at the 7% HD-FEC threshold (3.8×10^{-3}) for different CSPR values. Dotted-dashed line shown in (b) represents system performance with ideal optical and electrical components at 7-dB CSPR.	105

Fig. 4.6. (a) BER versus CSPR at optimum launch power values for different link lengths, and (b) BER versus launch optical power per channel for 3 spans (240 km) at different values of CSPR.	106
Fig. 4.7. (a) BER versus KK oversampling ratio for 240 km with optimum CSPR (8 dB) and launch power (0 dBm), and (b) OSNR penalty [dB] at BER= 10^{-3} versus receiver optical filter frequency drift for 3 rd and 7 th order super-Gaussian filter response in B2B configuration with noise loading. EVM values of constellations in insets of (a) are 10.8% and 14.9% for 6 Sam/Sym and 3 Sam/Sym, respectively.	108
Fig. 5.1. Simulation results for (upper) RIN and (lower) FM-noise PSD before and after passing through SOA with linear ($P_{in} = -20$ dBm) and saturated ($P_{in} = 0$ dBm) operation regimes..	115
Fig. 5.2. Schematic of the experimental setup used for phase and intensity noise measurements and back-to-back coherent transmission. Dashed-outlined blocks are used only for the coherent transmission setup.	118
Fig. 5.3. Measured (upper) RIN and (lower) FM-noise PSDs before and after passing through the SOA with saturated ($P_{in} = 0$ dBm) gain. The insets in (a) display the complex-plane scatter plots of the normalized complex envelopes without and with passing through the SOA, within 5 GHz bandwidth.	119
Fig. 5.4. IMDD performance experimental setup.	120
Fig. 5.5. (Left): BER as a function of received optical power for PAM4 at 10 GBd; and (right): BER as a function of OSNR for a 16-QAM coherent link at 5 GBd, both with and without SOA-based RIN reduction. ECL with RIN <-140 dB/Hz was used as the transmitter CW source for comparison.	121
Fig. 5.6. Simulation results of the difference of required E_b/N_0 with and without SOA-based RIN reduction as a function of symbol rate.	122

List of Abbreviations

ADC	Analog to digital converter
ASE	Amplified spontaneous emission
ASIC	Application-specific integrated circuit
B2B	Back to back
BER	Bit error ratio
BPSK	Binary phase shift keying
CD	Chromatic dispersion
CMPN	Common mode phase noise
CPR	Carrier phase recovery
CW	Continuous wave
CWDM	Coarse wavelength division multiplexing
DCI	Data center interconnect
DFB	Distributed feedback (laser)
DPN	Differential phase noise
DSP	Digital signal processing
E_b/N_0	Bit energy/noise power spectral density
ECL	External cavity laser
EDC	Electronic dispersion compensation
EDFA	Erbium-doped fiber amplifier
EEPON	Equalization-enhanced phase noise
ESA	Electrical spectrum analyzer
FEC	Forward error correction
FIR	Finite impulse response
FM	Frequency modulation
FO	Frequency offset
FOC	Frequency offset compensation
FWHM	Full width at half maximum
GBd	Giga baud (Giga symbol/second)
HD-FEC	Hard decision - forward error correction

IDMP	Intrinsic differential mode phase
IMDD	Intensity modulation and direct detection
KK	Kramers-Kronig
LEL	Lorentzian-equivalent linewidth
LO	Local oscillator
LUT	Laser under test
MZM	Mach-Zehnder modulator
NG-PON	Next generation - passive optical network
NRZ	Non-return to zero
OA	Optical amplifier
O-BPF	Optical - bandpass filter
OPLL	Optical phase-locked loop
OSA	Optical spectrum analyzer
OSNR	Optical signal to noise ratio
OTN	Optical transport network
PAM4	Pulse amplitude modulation with 4 levels
PAPR	Peak to average power ratio
PBC	Polarization beam combiner
PD	Photodiode (photodetector)
PDM	Polarization division multiplexing
PIC	Photonic integrated circuit
PLC	Planar lightwave circuit
PM	Polarization maintaining, <u>OR</u> Polarization multiplexing
PMD	Polarization mode dispersion
PNT	Phase noise trajectory
PON	Passive optical network
PSD	Power spectral density
PSK	Phase shift keying
QAM	Quadrature amplitude modulation
QD-MLL	Quantum dot - mode locked laser
RBW	Resolution bandwidth

RC	Raised cosine
RRC	Root raised cosine
RIN	Relative intensity noise
ROADM	Reconfigurable optical add/drop multiplexer
R-OSNR	Required - optical signal to noise ratio
RTOSO	Real-time sampling oscilloscope
Rx	Receiver
RZ	Return to zero
SDH	Synchronous digital hierarchy
SE	Spectral efficiency
SGDBR	Sampled grating distributed Bragg reflector (laser)
SNR	Signal to noise ratio
SOA	Semiconductor optical amplifier
SONET	Synchronous optical network
SSB	Single sideband
SSBI	Signal to signal beat interference
SSMF	Standard single mode fiber
TDM	Time division multiplexing
TIA	Trans-impedance amplifier
Tx	Transmitter
WDM	Wavelength division multiplexing
WGN	White Gaussian noise

Chapter 1

Introduction

1.1 Motivation and Outline

Driven by the growing use of internet traffic in a wide range of applications that require high data throughput, such as ultra-high definition video streaming and gaming, cloud computing, and modern mobile network services, there is a huge demand for optical communication networks to cope with the required transmission capacities. This growth includes all the different scales of optical networks, ranging from short interconnects used to transmit data between network elements in the same datacenter room, to metro, regional, long-haul, and submarine transmission systems that can extend to thousands of kilometers in reach, operating at multiple tera bit per second (Tb/s) rates for each optical fiber link. This growing demand of higher network capacity requires existing systems to upgrade in a scalable fashion, with minimum cost and energy per transmitted bit. This can only be achieved by developing modern transmission technologies with high spectral efficiency (SE) to upgrade the current optical networks represented by the deployed fiber infrastructures and the photonic system components comprising the wavelength division multiplexing (WDM) network nodes, like optical amplifiers, filters, and (de)multiplexers. Furthermore, dynamic reconfigurability of optical networks is also required to address the time-changing nature of traffic demands and desired service availability and survivability with reconfigurable optical add-drop multiplexing (ROADM) capabilities at high transport efficiency.

Therefore, advanced transmission schemes with higher spectral efficiency and robustness against transmission impairments are needed to meet these requirements in the current and next generation of optical transmission systems.

Current high-speed optical links used in medium- and short-reach optical interconnects operate at data rates of 10 to 200 Gb/s per wavelength, carrying time-division-multiplexed (TDM) and Ethernet packet data. This includes different commercial standards. For example, the *synchronous optical network* (SONET) and the *synchronous digital hierarchy* (SDH) as TDM standards, the modern *optical transport network* (OTN) standard [1], and the packet-based optical client interface standards of (ultra-)high-speed Ethernet services ranging from the 1 GbE to the 200 GbE standards [2]. The current efforts of standardization organizations are focused on standardizing the 400 GbE and 800 Gbps interfaces for the next generation of optical interconnects [3]. Technology forecasts show a potential demand for interconnect technologies operating at > Tb/s rates in the foreseeable future. Transceivers operating at these high data rates are required to have high energy efficiency, low system complexity and cost, and small transceiver footprint to allow higher port density. This is important especially for systems employing nested client interfaces on the front panels of data equipment boards in high-capacity packet-network routers and datacenters, comprising most practical systems using these high throughput technologies today. Intensity modulation and direct detection (IMDD) schemes, known for their low system complexity and cost, are the dominant technologies used in the current standards of these short-reach applications. For instance, the 4-level pulse amplitude modulation (PAM4) is the modulation scheme used in the modern standards of 200 GbE and 400 GbE. The practical SE of < 2 bit/s/Hz of this modulation scheme mandates the use of multiple coarse WDM (CWDM) channels to achieve the required ≥ 200 Gb/s rates, with the highest available bandwidths of the electronic and

electro-optic components limited to only tens of GHz [3]. The link reach of these schemes can extend to only a few kilometers before the linear fiber impairments, such as power losses and chromatic dispersion, become unmanageable. Digital coherent technology, on the other hand, can provide much higher SE by enabling high-order quadrature amplitude modulation (QAM) formats and polarization multiplexing. However, this technology has relatively higher complexity and cost stemming from the stringent requirements on the specifications of subsystem components such as the laser sources, optical modulators and receivers, and the essential digital signal processing (DSP) units. These requirements have limited the use of coherent technology primarily to high-capacity long reach applications that require high performance and resilience to severe channel impairment conditions. Employing the coherent technologies in short and medium reach applications only recently became a very active area of research in academic and industrial communities, with various schemes and technologies demonstrated to achieve high spectral efficiency and channel impairment mitigation capabilities. Therefore, ongoing research works aim, generally, to make the best utilization of the bandwidths of state-of-the-art electronic and electro-optic components at the lowest possible complexity, cost, and energy consumption.

The focus of this dissertation is to investigate, in depth, one of the major concerns in the design and implementation of coherent optical transceivers for short reach applications: laser phase noise. Phase noise is one of the performance-limiting factors in coherent communication systems in which the information is carried by both the phase and the intensity of the optical carrier. In general, phase noise can be induced by transmitter and receiver laser sources, nonlinear effects in the fiber channel or other system components such as the optical amplifiers, limited accuracy of the compensation of frequency offset between the transmitter and receiver laser sources, or by some digital signal processing stages, such as the equalization-enhanced phase noise (EEPN) [4-

6]. The overall phase perturbations from these different sources must be tracked and compensated at the receiver side by (digital or analog) signal processing before making decisions on the received signals to recover the transmitted information bits. High-quality laser sources with low levels of phase noise, typically, external cavity lasers (ECLs), are usually used in coherent systems that are developed for long reach applications. However, these lasers are usually associated with high fabrication complexity, high costs, and relatively large footprints. This limits the feasibility of using these types of lasers for short reach coherent applications, where lasers are the main sources of phase noise. Although laser phase noise is a well-known and extensively studied impairment, there is still a lack of systemic investigations to embrace lasers with non-white phase noise and specify their impact on the performance of DSP-enabled coherent optical systems. To this end, this dissertation provides an insight into studying the characteristics, specifications, and measurements of laser phase noises and their impact in system performance. An emphasis on a special class of multi-wavelength (or multi-mode) semiconductor laser sources is made, namely, quantum-dot mode-locked lasers (QD-MLL). The dissertation is organized as follows:

- The rest of **Chapter 1** will provide an overview on the evolution of the transmission technologies adopted by optical communication networks; describe the basic structures of generic IMDD, coherent, and self-coherent optical communication systems; and will give a basic description of laser phase and intensity noises and their measurements.
- **Chapter 2** will establish the foundation of the contributions of this research work in the characterization of laser phase and the assessment of its impact in digital coherent systems. The major focus of this study is on the spectral properties of laser phase noise and their relationship with the measured spectral linewidth, as well as the performance of coherent systems. The study is intended to be generic to include lasers with various

phase noise features, and the investigations include theoretical modeling, numerical simulations, and experimental validation.

- **Chapter 3** presents a detailed study of the properties of phase noises in QD-MLLs. These devices generate multiple spectral lines simultaneously, with unique phase noise properties. Based on the analysis and assessment criteria provided in Chapter 1, the performance of intra- and inter-line phase noises from these comb sources is assessed with support of experimental demonstrations. Also presented in this chapter is a coherent multi-heterodyne technique used for simultaneous measurement of phase noises from all comb lines of an optical comb source.
- **Chapter 4** presents a novel system structure that simultaneously generates multiple single-sideband (SSB) field-modulated channels from a single QD-MLL comb source for self-coherent DD systems. The proposed system utilizes the mutual coherence between adjacent comb lines and provides a low-complexity, cost effective, and energy efficient way to transmit multiple SSB channels with QAM modulation formats for simple direct detection reception at the receiver side. Theoretical analysis is performed to understand the effects of phase and intensity noises in the proposed scheme. Simulations based on experimentally measured complex optical field waveforms from a practical QD-MLL source were used for the assessment of system performance.
- **Chapter 5** is dedicated to the study of phase noise properties when an unmodulated optical carrier passes through a semiconductor optical amplifier (SOA) operating in the saturation regime, used to suppress the laser intensity noise. We found that associated with the intensity noise reduction was a phase noise enhancement. Despite that this phase noise enhancement is not measurable by conventional linewidth measures, it can

deteriorate the performance in coherent systems. Theoretical, simulation, and experimental results are provided to explain the observed effect.

- Finally, **Chapter 6** is dedicated to the proposed directions for potential extensions of the current work.

1.2 Evolution of Transmission Technologies in Fiber Optic Communications

Most commercial high-speed optical transmission systems used IMDD schemes carrying binary modulation formats until the early 2000s. A common modulation scheme for these systems was the IMDD of non-return-to-zero (NRZ) line coding format, wherein the maximum theoretical spectral efficiency was limited to only 1 bit/s/Hz. These links operated at rates of up to 10 Gb/s per a single WDM channel in standardized synchronous networks. During that time, several lab demonstrations were reported for systems operating at 40 Gb/s per single WDM channel [7,8]. This was only achieved with high-complexity systems that required careful optical management of linear and nonlinear fiber channel impairments, along with the use of high-performance and expensive optical modulators and electronic subsystems. The need for higher link capacities drove the research efforts to focus on higher SE systems to avoid the proportional increase in optical and electrical bandwidth with the transmitted channel data rate. The high SE requirement revived the research interest in coherent detection systems, after they gradually lost attention in the years following 1990 due to the high costs of low-phase-noise lasers and the commercial emergence of erbium-doped fiber amplifiers (EDFAs) [9]. In fact, in these early years, the major purpose of employing coherent detection was to improve receiver sensitivity and extend repeaterless transmission distances [10,11].

The initial research efforts that were made in the early 2000s targeting higher spectral efficiency resulted in developing schemes employing differential coherent detection of quaternary phase shift keying (QPSK) optical signals, which modulates binary data on each of the in-phase (I) and quadrature (Q) components of the complex optical field. This results in a theoretical spectral efficiency of 2 bit/s/Hz for each single optical channel [12,13]. Increasing the data rate for these schemes would require higher electrical bandwidth at the transmitter and receiver electronics, which hindered these systems from addressing the increasing capacity demands, and limited their transmission rates to operate at 40 Gb/s per WDM channel. This increase in required bandwidth not only influences system complexity and cost, but also increases the effects of linear channel impairment, like chromatic dispersion (CD) and polarization-mode dispersion (PMD), which limits the repeaterless link reach, given that the tolerance to these effects reduces about 4 times when the symbol rate is doubled [14]. To double the spectral efficiency of these systems, polarization division multiplexing was also investigated to modulate two independent data channels on the two polarizations of the optical signal within the same bandwidth [15]. In these systems, unfortunately, dynamic polarization control was required at the receiver to follow the time-varying rotations in the state of polarization, which adds more cost and complexity and limits system design flexibility. *Homodyne* coherent optical transmission was demonstrated by many groups with the potential to achieve SE of >2 bit/s/Hz. However, these systems suffered from the high cost and complexity in the optical phase-locking loop (OPLL) required to lock the optical frequency and phase of an optical local oscillator (LO) laser with that of the incoming optical signal [16]. Implementing the phase locking in the RF domain with the optical *heterodyne* scheme would increase the required receiver electrical bandwidth further.

The advancement in DSP systems has paved the way in the mid 2000s for the implementation of coherent communication systems with free running LO lasers, in what is known today as *digital coherent receivers* [17-20]. These systems use the *intradyne* scheme, where the LO laser operates at a frequency as close as possible to the center frequency of the incoming data signal, without the use of OPLL. Therefore, all the associated DSP algorithms are applied on the complex data signals in the baseband. The residual difference in frequency is compensated in the digital domain by a frequency estimation and compensation algorithm. Phase mismatch and fluctuations are tracked and compensated by dedicated DSP algorithms within the digital receiver as well. Nonetheless, linear transmission impairments can also be compensated for digitally, and polarization tracking can be done digitally as well with the use of adaptive DSP filters with dynamic coefficients. These attractive capabilities of digital coherent systems have revolutionized the optical communications research and industry and added much flexibility to link and network design with powerful capabilities. Since its first commercial introduction in 2008, digital coherent technology has been the dominant technology in the metro scale and longer reach networks. Nevertheless, coherent technology for applications with shorter reach is being explored by academic and industrial research groups and standardization organizations [21,22].

The intradyne digital coherent receiver, as will be shown below, requires a hybrid optical network to mix the incoming optical signal with that from the LO. In addition, four PDs, two transimpedance amplifiers (TIAs), and two analog-to-digital converters (ADCs) are typically required at the receiver side to recover the I and Q components from each orthogonal polarization of the complex envelope of the received optical signal [23]. This scheme is still considered of high complexity for cost-sensitive applications, compared to DD systems that require only a single PD, TIA and, optionally, an ADC at the receiver. Therefore, there has been an increasing interest in

developing single PD-based DD schemes with SE values exceeding that of the PAM4 for cost sensitive and high transceiver density applications. This can be achieved by SSB complex modulation of QAM formats at the transmitter, with DD and DSP at the receiver. The DSP at the receiver is required to mitigate a known problem in this DD scheme: the signal-signal beat interference (SSBI), where each different spectral component within the data band mixes with the other components due to the nonlinear transfer function of the PD. The adoption of DSP at the receiver also enables electronic dispersion compensation (EDC) to mitigate the chromatic dispersion effect for applications that extend for tens of kilometers with standard single-mode fibers. Furthermore, demultiplexing two orthogonal polarizations has also been demonstrated in SSB-DD schemes with the aid of adaptive DSP. Several effective DSP schemes have been proposed in the years 2015-2016 to mitigate the effect of SSBI [24-28]. The Kramers-Kronig (KK) *field reconstruction* scheme [28] has been proven to exhibit superior performance compared to the other proposed schemes that are typically based on SSBI calculation and *compensation* [29]. Therefore, this scheme is chosen as the SSBI mitigation scheme in the work presented in Chapter 4. The basic structure and operation principle of this scheme will be provided in Sec. 1.3.2.

1.3 Background Information

This section will provide some background and introductory information about the main underlying topics comprising the rest of the chapters in this dissertation.

1.3.1 Direct vs. Coherent Detection Systems

Optical communication systems can be divided into two main categories according to the method they modulate the data on the optical carrier and the way they retrieve the information from the signal at the receiver: *direct* and *coherent* detection systems. In direct detection systems the data

is modulated on the intensity of the optical carrier and detected at the receiver by simply applying the received optical signal onto a photodetector diode (PD) which will convert the optical intensity variations into an electric current according to the square-law detection; hence the name IMDD. Modulation at the transmitter can be done either in direct modulation, or by an external modulation technique. In the case of direct modulation, the data signal is used to control the bias current of the laser source and, therefore, the output signal intensity is modulated accordingly. Whereas in external modulation, the intensity of a continuous wave (CW) signal output from the laser source is altered by an external electro-optic modulator according to the level of the modulating data symbol [30,31]. Common modulation formats in such systems are the NRZ, return-to-zero (RZ), PAM4, and DD orthogonal frequency-division multiplexing (OFDM) [31,32]. As was mentioned above, for its low complexity and cost effectiveness, the IMDD scheme is the most common scheme for cost-sensitive and short distance applications. The schematic of a generic IMDD system with external modulation is shown in Fig. 1.1(a).

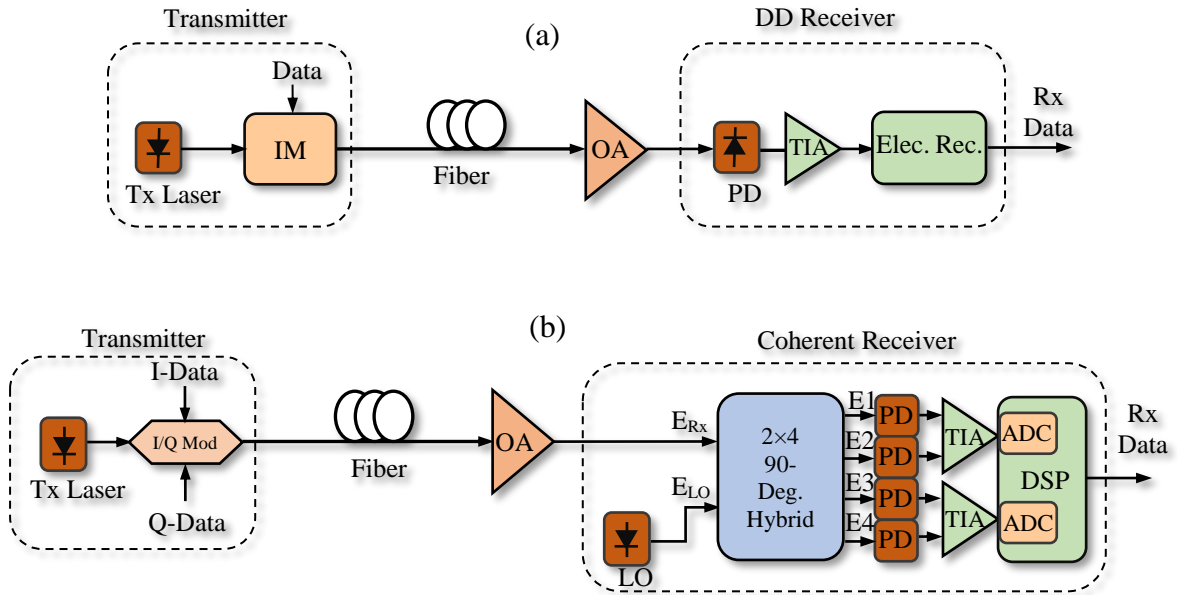


Fig. 1.1. Generic schematic of (a) direct detection and (b) digital coherent transmission system. OA: optical amplifier.

As shown in Fig. 1.1, the output photocurrent from the photodetector is converted into a voltage signal through the TIA, after which the signal is processed in the electronic receiver either in its analog form or in the digital domain after being converted into the digital form by an ADC, depending on the modulation format, performance requirements, and system design. Equalization and clock and data recovery are the main processing stages required in these receivers.

On the other hand, in coherent communication systems the information can be modulated on the phase of the carrier (in addition to the intensity) through an external phase modulator or I/Q complex modulator [31]. Phase shift keying (PSK) modulation can be implemented in such systems using optical phase modulators, without modulating the magnitude [33]. Examples of common PSK levels used in such systems are the binary PSK (BPSK), QPSK, and 8-PSK formats. M -QAM formats can be obtained when an I/Q optical modulator is used, allowing for theoretical SE values of $\log_2(M)$ bit/s/Hz per single polarization. The receiver in coherent systems must recover the phase of the incoming modulated signal. Homodyne and heterodyne optical coherent receiver techniques can be used for this purpose. However, their high implementation complexity makes the digital (intradynic) coherent receiver scheme the dominant, practical technique in modern high-speed systems [16,31]. In digital coherent receivers the incoming optical signal is mixed with an LO optical signal in a 90-degree optical hybrid so that the I and Q components of the modulated complex data signal are recovered. To utilize all the available degrees of freedom in an optical signal, independent QAM data can be modulated on the two orthogonal polarization components of the optical carrier to double the transmission data rate and SE in what is called polarization division multiplexing (PDM) [23]. The schematic of a generic, single polarization digital coherent receiver is shown in Fig. 1.1(b). The I/Q modulator consists of two Mach-Zehnder

modulators (MZMs) and a 90-degree phase shifter to modulate the I and Q components of the baseband complex data symbols on the I and Q components of the optical carrier [23,31,34]. Following the notations in Fig 1.1(b), the field of the received optical signal, $E_{Rx}(t)$, and the LO, $E_{LO}(t)$, can be expressed as

$$E_{Rx}(t) = A_{Rx}(t)e^{i[\omega_{Rx}t + \varphi_{Rx}(t)]} \quad (1.3)$$

$$E_{LO}(t) = A_{LO}e^{i[\omega_{LO}t + \varphi_{LO}(t)]} \quad (1.4)$$

where $A_{Rx}(t)$ is the complex amplitude of the received signal, A_{LO} is the constant amplitude of the LO, and $\omega_{Rx,LO}$ and $\varphi_{Rx,LO}(t)$ are the optical angular frequency and phase of the signals denoted by the subscripts, respectively. The optical signals at the outputs of the phase diversity 90-degree 2×4 optical hybrid can be expressed as

$$\begin{aligned} E1 &= E_{Rx} + E_{LO} , & E2 &= E_{Rx} - E_{LO} \\ E3 &= E_{Rx} + iE_{LO} , & E4 &= E_{Rx} - iE_{LO} \end{aligned} \quad (1.5)$$

The corresponding photocurrents generated at the photodiodes are expressed by [23,31]:

$$\begin{aligned} I_1 &= \Re|E1|^2 = \Re[P_{Rx}(t) + P_{LO} + 2\Re\{E_{Rx}(t)E_{LO}^*(t)\}] \\ I_2 &= \Re|E2|^2 = \Re[P_{Rx}(t) + P_{LO} - 2\Re\{E_{Rx}(t)E_{LO}^*(t)\}] \\ I_3 &= \Re|E3|^2 = \Re[P_{Rx}(t) + P_{LO} + 2\Im\{E_{Rx}(t)E_{LO}^*(t)\}] \\ I_4 &= \Re|E4|^2 = \Re[P_{Rx}(t) + P_{LO} - 2\Im\{E_{Rx}(t)E_{LO}^*(t)\}] \end{aligned} \quad (1.6)$$

where \Re is the PD responsivity, P is the optical power of the signal denoted by the subscript, and $\Re\{\cdot\}$, $\Im\{\cdot\}$, and $*$ denote the real, imaginary, and complex conjugate of a complex quantity, respectively. The first two terms in the right-hand side of Eq. (1.6) represent DC components, assuming $P_{LO} \gg P_{Rx}$, and are cancelled out by subtracting I_2 from I_1 and I_4 from I_3 to get the normalized beat terms of interest as

$$I_I = I_1 - I_2 = \Re\{E_{Rx}(t)E_{LO}^*(t)\}, \text{ and}$$

$$I_Q = I_3 - I_4 = \text{Im}\{E_{Rx}(t)E_{LO}^*(t)\} \quad (1.7)$$

Note from Eq. (1.3) and (1.4) that if $\omega_{LO} = \omega_{Rx}$ the I_I and I_Q in Eq. (1.7) represent the I and Q components of the received optical signal, and, ideally, the transmitted data symbols. However, these frequencies are practically separated by a frequency offset (FO) that must be estimated and compensated for by receiver DSP [23,35]. Furthermore, the phase of the received optical signal $\varphi_{Rx}(t)$ not only contains the phase-modulated data, but also the transmitter laser phase noise and some other channel-induced phase noises. These phase noises and the LO phase noise can be estimated and compensated for to some extent using DSP-based carrier phase recovery (CPR) algorithms [4,5,23,35].

In the case of polarization-division multiplexing (PDM) transmission the 2×4 optical hybrid shown in Fig. 1.1(b) is replaced by a 2×8 optical hybrid with polarization diversity and, accordingly, the number of PDs and TIAs is doubled to handle the complex information on the two polarizations [23,35]. To support PDM transmission, the transmitter generates two independent I/Q-modulated optical signals from the same laser source and combine them with orthogonal polarization states using a polarization beam combiner (PBC). Figure 1.2 shows the structure of a PDM transmitter and the polarization diversity digital coherent receiver with the main DSP blocks of each part. At the transmitter, the binary data is first encoded using a forward error correction (FEC) scheme and the encoded data is fed to the QAM modulator block for bits-to-symbol mapping. In general, this mapping block can employ any PSK or QAM constellations. Geometric and/or probabilistic constellation shaping can be implemented within these two blocks as well [36,37]. The output QAM data samples are up-sampled and fed into the spectral shaping filters for temporal (pulse) and spectral shaping, which can be implemented either in the time or frequency domain [35]. Raised-cosine or root-raised-cosine filters are typically used as Nyquist

pulse shaping filters [23,35]. Spectral shaping may include digital pre-emphasis (pre-distortion) to compensate for optical modulators' and DACs frequency roll-off responses [38-40]. The digital output signals from the shaping filters are then converted into the analog domain through four DACs [41] and used to drive the I and Q inputs of the two optical I/Q modulators to map the complex QAM signals to the complex envelopes of the two orthogonal polarizations of the optical signal. The outputs of these modulators are combined orthogonally by the PBC and amplified before being launched into the fiber channel.

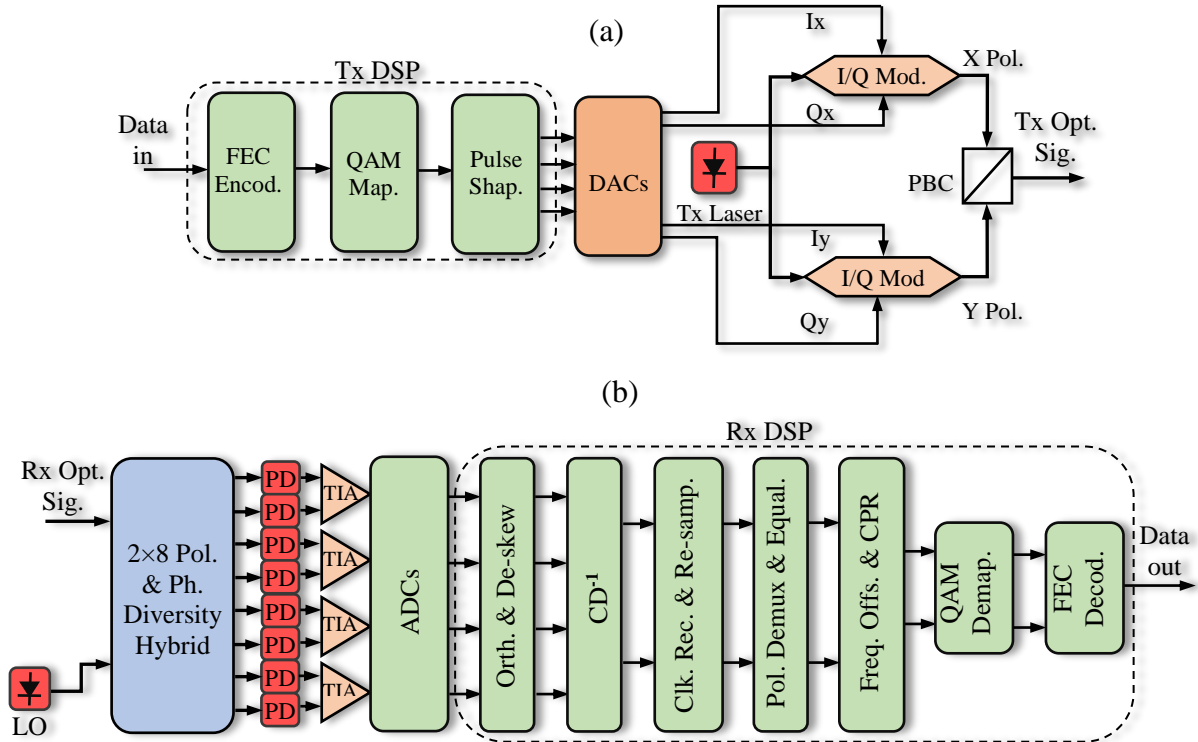


Fig. 1.2. General functional blocks of (a) transmitter and (b) receiver in a PDM digital coherent communication system.

The receiver contains the main DSP blocks that enable the mitigation and compensation of transmission channel impairments and transceiver component imperfections. As shown in Fig. 1.2(b), the received optical signal is input to a polarization and phase diversity 2x8 optical hybrid. The four photocurrent signals, comprising the I and Q components of the two polarizations, are amplified through the TIAs and the analog signals are then converted to the digital domain through

the four ADCs operating at a sampling frequency higher than the transmission symbol rate [41]. The first DSP block is the orthogonalization and de-skew which compensates for the imperfections in the receiver front end components, like the non-perfectly orthogonal 90-degree phase shifters and the relative time delays between the I and Q components arriving the PDs [35,42]. This can also compensate for the PDs' responsivity and TIAs' gain mismatches. Gram-Schmidt or Löwdin procedure can be employed for signal orthogonalization, and time de-skew can be achieved through nonlinear interpolation [42,43]. The chromatic dispersion incurred by the propagation through the fiber channel is then compensated either by linear convolution in the time domain by employing finite impulse response (FIR) filters, with impulse responses representing the inverse of the CD effect, or in the frequency domain, by multiplying the Fourier transform of the signal by the channel transfer function [35,42,44]. After dispersion compensation, the clock frequency is recovered from the data and the signal is resampled to a specific oversampling rate, typically with oversampling of 2 Sa/Sym . The output from the clock recovery process may be sent in a feedback loop to the ADCs for stabilization [42]. The resampled output is fed to adaptive equalization blocks which compensate for the PMD and demultiplexes the orthogonal polarization components [35]. Residual frequency offset between the signal carrier and the LO signal is estimated and compensated by a frequency offset compensation (FOC) algorithm [35,45-48]. CPR is then applied to compensate for the phase noise before symbol-to-bits de-mapping and FEC decoding [4,5,35,42].

The functional blocks shown in Fig. 1.2(b) represent the mandatory building blocks in a digital coherent receiver required to ensure practical functionality of the receiver. Several receiver architectures can be built with some modifications to the order of some of these blocks. Feedback and control loops may be used between different blocks, not shown in the schematic above for

simplicity. Examples of feedback signals can be from the frequency estimation block to the LO drive circuit to limit the range of frequency drifting, which may reach up to 5 GHz for free-running practical tunable lasers before their end of life [49]; or from the carrier phase estimation to the frequency estimation for increasing the operational accuracy of the latter [42]; or from the output of the CPR block to the adaptive equalization filters to update the filter tap values in the case of decision-directed equalization [35].

1.3.2 Self-Coherent Optical SSB Modulation and the Kramers-Kronig Receiver

The single-PD DD system shown in the previous section (Fig. 1.1(a)) supports only intensity modulation with PAM formats at the transmitter side, i.e., IMDD. In which case the modulation is a double-sideband (DSB) modulation and the optical signal bandwidth is, typically, equal to double the value of the symbol rate of the transmitted signal, resulting in a relatively low optical SE. Furthermore, because of the square law detection at the receiver PD, IMDD schemes cannot use receiver-side EDC to compensate for the CD induced by the fiber channel [31,50,51]. This is because the electrical signal generated at the output of the photodetector is proportional to only the intensity of the optical signal and it does not preserve information about the phase of the optical signal, which is required for the EDC process [35]. Therefore, to increase the SE and enable EDC in DD systems, it is required to exploit the field of the optical signal for both phase and amplitude data modulation. This can be achieved by modulating the complex envelope of the transmitted optical signal with single-sideband (SSB) modulation, which can be done by the same technique as in coherent systems with an I/Q optical modulator at the transmitter side. SSB modulation not only enables the adoption of M -QAM formats that can outperform the IMDD formats in SE, but also provides the possibility of implementing EDC by receiver DSP.

An unmodulated optical CW signal is required to be added with the SSB modulated signal for DD with a single-PD reception. This CW tone must have an optical frequency out of the spectral band of the SSB modulated signal to mix with every spectral component of the SSB signal at the PD receiver without spectral interference. The CW component is either injected at the receiver side before the PD detection [52] or transmitted along with the modulated signal band at the transmitter side [53-56]. Systems with the latter option are referred to as *self-coherent*. After DD in a PD, the electrical signal is sampled by an ADC and fed into the DSP unit for further processing.

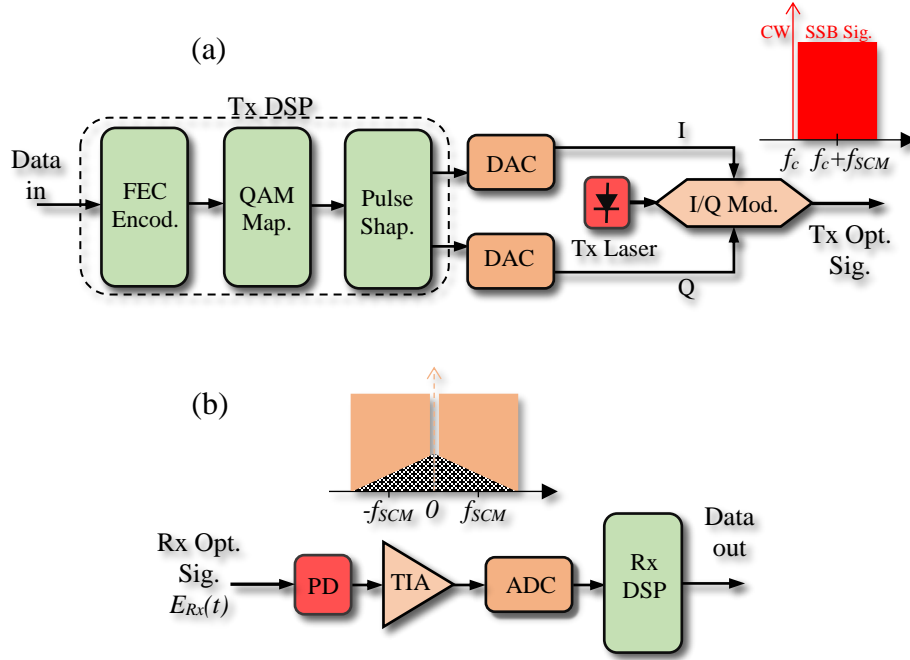


Fig. 1.3. General functional blocks of (a) transmitter and (b) receiver in a self-coherent SSB DD system.

Figure 1.3 shows a generic structure of self-coherent SSB DD system in which the transmitted signal is generated by modulating a QAM signal (either single-carrier or in OFDM) on a single side of the main optical carrier using an optical I/Q modulator. This modulation is similar to that in a coherent system, with the only difference being the I and Q electrical signals fed into the modulator's input in this scheme are frequency shifted in transmitter DSP to an RF frequency.

This is done so that the center frequency of the modulated optical band does not sit at the center of the optical carrier. The modulator bias is tuned so that a component of the carrier is output without being totally suppressed, to provide the CW tone required for the DD, as shown in the inset of Fig. 1.3(a). This SSB modulation is also referred to as *sub-carrier modulation* (SCM) [29,53]; and the CW tone at the side (or the edge) of the signal band is considered equivalent to a local oscillator signal.

Another method of generating the SSB signal with a CW carrier component at one side is by modulating the baseband of the I and Q components on the center of the optical carrier with total carrier suppression, just like what is done in a typical coherent system, and adding the carrier in the optical domain. The carrier in this case can be generated from another laser source or by using a separate modulator to produce a frequency-shifted version of the original carrier after tapping that signal from the laser source [56]. Alternatively, a carrier tone can be generated at the edge of the complex baseband data in the electrical domain before the optical modulation, which will reflect to an optical carrier after normal optical I/Q modulation. This can be implemented either in the digital [54] or the analog domain [55,56].

A known intrinsic problem in SSB modulation with DD schemes is the signal-to-signal beat interference (SSBI) resulting from the nonlinear mixing between the spectral components of the modulated data band at the PD in the square law detection operation. To better understand this, the complex envelope of the received optical signal, $E_{Rx}(t)$, at the PD can be expressed as

$$E_{Rx}(t) = E_c + S(t) \exp(j\pi Bt) \quad (1.8)$$

where E_c is the unmodulated CW carrier component and $S(t)$ is the QAM signal with total bandwidth of B . The frequency component in the second term, $\exp(j\pi Bt)$, indicates that $S(t)$ is frequency shifted from the carrier tone E_c by $B/2$ Hz, or equivalently, the carrier component E_c is

sitting at the edge of the spectrum of $S(t)$, as shown in the inset of Fig. 1.3(a). The photocurrent generated at the PD output is

$$i(t) = |E_{Rx}(t)|^2 = E_c^2 + |S(t) \exp(j\pi Bt)|^2 + E_c^* \cdot S(t) \exp(j\pi Bt) + E_c \cdot S^*(t) \exp(-j\pi Bt) \quad (1.9)$$

where x^* indicates the complex conjugate notation of x , and the PD responsivity is assumed to be unity. The first term in the right-hand side is (ideally) a constant DC term. The second term is the SSBI term that falls within the same frequency band of the useful term, the third term, and corrupts the data signal $S(t)$. The last term is a conjugated version of the useful signal at the other side of the spectrum and can be cancelled out by a simple digital filtration operation. The spectrum of $i(t)$ is shown in the inset in Fig. 1.3(b). Note that as $i(t)$ is a real and positive signal, it has a DC component and its spectrum has even symmetry around the origin. The spectrum of the SSBI term is represented by the dark component in the spectrum, which typically has stronger components at low frequencies and its spectral density tends to decrease at higher frequencies. This SSBI can be avoided by leaving a sufficient frequency guard band between the data-bearing band and the unmodulated carrier tone. But this results in reduced system SE, and will require double the bandwidth for the receiver optical and electronic components, which violates the high-SE goal of this modulation and detection scheme. Instead, an electronic SSBI cancellation procedure based on DSP can be adopted to remove (or reduce) the effect of SSBI and improve system performance. After applying the SSBI cancellation algorithm, EDC can be applied before the signal undergoes consequent demodulation processing.

Several SSBI cancellation schemes, also known as *receiver-linearization schemes*, with different advantages and drawbacks have been proposed. The most known schemes are: the single-stage linearization filter [24]; the two-stage linearization filter [25]; the SSBI estimation and

cancellation filter [26]; the iterative linearization filter [27]; and the Kramers-Kronig (KK) field reconstruction algorithm [28].

The first four schemes assume that the SSBI is a perturbation that can be calculated or estimated and subtracted from the signal. The KK scheme is based on field reconstruction from the intensity of the signal that satisfies a specific condition called the *minimum-phase* condition, which is related to the carrier-to-signal power ratio (CSPR). The CSPR is defined as the ratio of the optical power of the unmodulated CW carrier to the power of the data-bearing signal. That is

$$CSPR = 10 \times \text{Log}_{10}(P_c/P_s) \text{ [dB]} \quad (1.10)$$

where $P_c = E_c^2$ and $P_s = \langle |S(t)|^2 \rangle$ are the optical powers of the unmodulated carrier and the modulated signal, respectively, and $\langle \cdot \rangle$ represents time averaging. Regardless of which SSBI cancellation scheme is used, CSPR is a significant parameter in determining the performance of SSB DD systems.

As was mentioned above, the KK field reconstruction algorithm has been shown to provide superior results compared to all the other proposed SSBI cancellation schemes [29]. To understand the physical meaning of the *minimum phase* condition required for successful reconstruction of the complex field from the intensity of the signal, let us consider the complex envelope of the optical SSB signal given by Eq. (1.8), that is

$$E_{Rx}(t) = E_c + S(t) \exp(j\pi Bt)$$

The signal $E_{Rx}(t)$ is said to be of minimum phase only when its time trajectory does not wind around the origin of the complex plane. To satisfy this condition, the magnitude of the CW tone E_c has to be larger than the maximum magnitude in the signal $S(t)$, i.e., $|E_c| > \max\{|S(t)|\}$. Therefore, this condition is directly related to the CSPR defined by Eq. (1.10) and the peak-to-average power ratio (PAPR) of $S(t)$. Figure 1.4 shows examples of the time trajectories of $E_{Rx}(t)$

with different values of the ratio $|E_c|/\max\{|S(t)|\}$, where 16-QAM is assumed for $S(t)$. Note that since CSPR is calculated with the average of $|S(t)|^2$ over time other than the maximum value, and the PAPR of a signal is calculated as

$$PAPR_{S(t)} = \max\{|S(t)|^2\} / \langle |S(t)|^2 \rangle, \quad (1.11)$$

we can write the CSPR of $E_{Rx}(t)$ from (1.10) and (1.11) as

$$CSPR_{E_{Rx}(t)} = \frac{|E_c|^2}{\langle |S(t)|^2 \rangle} = \frac{|E_c|^2}{\max\{|S(t)|^2\}} PAPR_{S(t)} \quad (1.12)$$

Equation (1.12) states that for a signal to satisfy the minimum phase condition ($|E_c| > \max\{|S(t)|\}$) the CSPR of $E_{Rx}(t)$ should be higher than the PAPR of modulated signal $S(t)$. In other words, the required power of the unmodulated carrier tone to satisfy the minimum phase condition not only depends on the average power of the modulated signal $S(t)$, but also on the PAPR of the signal. The PAPR depends on different parameters like the modulation format and the pulse shaping filter used to limit the signal bandwidth in Nyquist QAM signals. For instance, the signal in Fig. 1.4(b) has a $|E_c|/\max\{|S(t)|\}$ ratio of 1, and its CSPR is 3.8 (or 5.8 dB) because $S(t)$ is a Nyquist 16-QAM signal shaped by a raised-cosine (RC) filter with a roll-off factor of $\beta = 0.1$, having a PAPR of 3.8 (5.8 dB).

When a signal satisfies the minimum phase condition, there is a unique relation between its instantaneous intensity and phase, the KK relation [28]. Therefore, the phase of the optical signal can be uniquely resolved from the intensity detected by the PD, i.e., the complex signal $S(t) \exp(j\pi Bt)$ can be reconstructed from $i(t) = |E_{Rx}(t)|^2$. Figure 1.5 shows the block diagram of the KK receiver algorithm. First, the positive, real-valued digital sequence from the ADC, representing the photocurrent $i(t)$, is normalized and resampled with an oversampling factor of ≥ 4 Sa/Sym. Next, the *phase* of the optical signal $E_{Rx}(t)$ is calculated by applying the Hilbert Transform to the natural logarithm of the square root of the data samples as

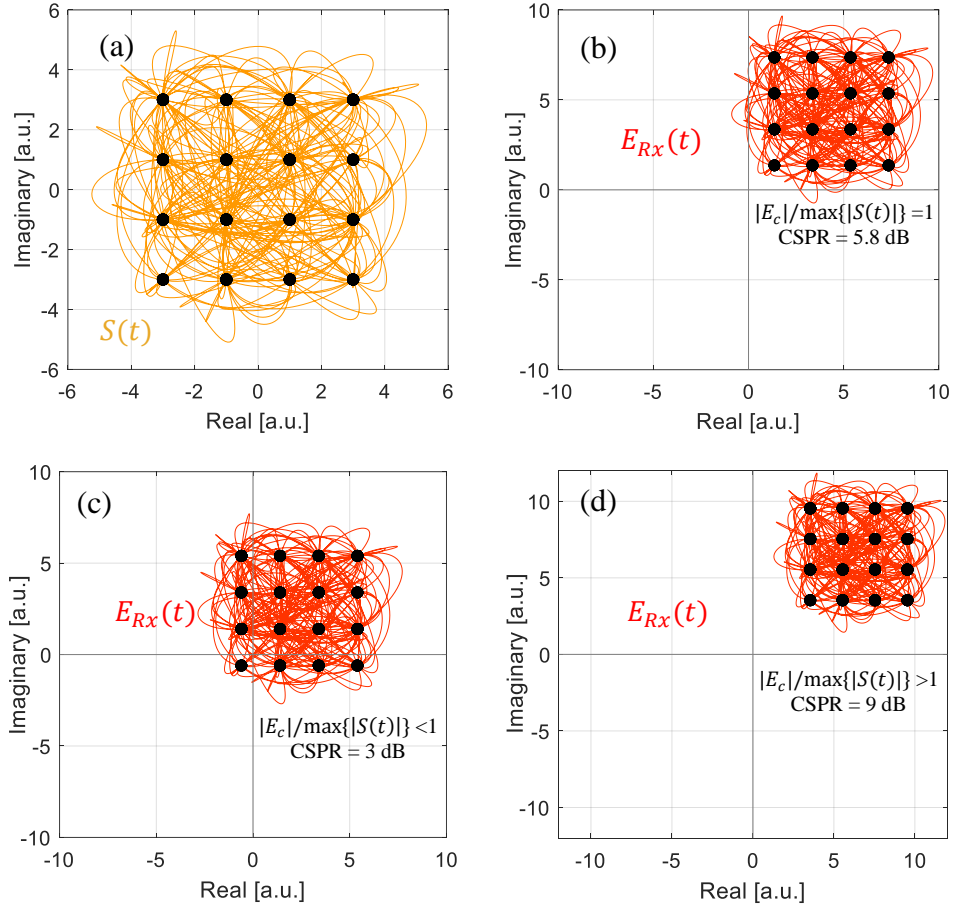


Fig. 1.4. Time trajectory on the complex plane for (a) $S(t)$: 16-QAM signal pulse-shaped by a RC filter ($\beta=0.1$); (b), (c), and (d) show $E_{Rx}(t)=E_c+S(t)$ at different values of CSRR. Black markers indicate samples at the center of symbols. $S(t)$ is assumed in the baseband in (b)-(d) for clarity.

$$\phi_E(t) = \mathcal{H} \left\{ \log \left(\sqrt{i(t)} \right) \right\} \quad (1.13)$$

where $\mathcal{H}\{\cdot\}$ represents the Hilbert Transform operation given by

$$\mathcal{H}\{f(t)\} = \frac{1}{\pi} p.v. \int_{-\infty}^{\infty} \frac{f(\tau)}{t - \tau} d\tau \quad (1.14)$$

where $p.v.$ is the integration principal value. This transform operation can also be conveniently implemented in the frequency domain as

$$\Phi_E(\omega) = j \cdot \text{sgn}(\omega) \cdot \mathcal{F} \left\{ \log \left(\sqrt{i(t)} \right) \right\} \quad (1.15)$$

where $\mathcal{F}\{\cdot\}$ is the Fourier Transform operation and $\text{sgn}(\cdot)$ is the signum function. Then $\phi_E(t)$ can be recovered from $\Phi_E(\omega)$ by the inverse Fourier transformation. After obtaining the phase of $E_{Rx}(t)$, the complex field can be simply constructed as

$$E_{Rx}(t) = \sqrt{i(t)} \exp[j \cdot \phi_E(t)] \quad (1.16)$$

The baseband complex data signal $S(t)$ can then be obtained by suppressing E_c and frequency down shifting as

$$S(t) = \{E_{Rx}(t) - E_c\} \cdot \exp(-j\pi Bt) \quad (1.17)$$

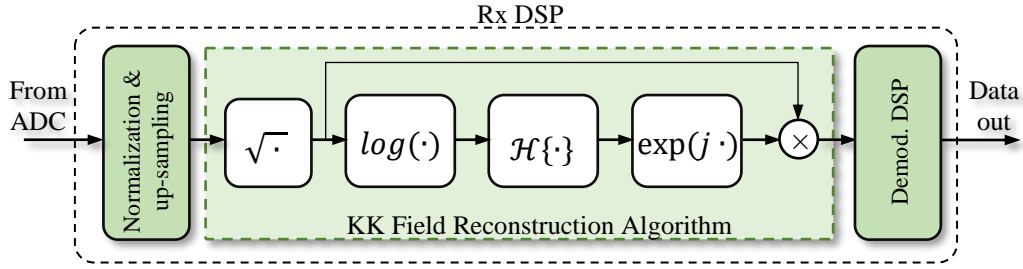


Fig. 1.5. Block diagram of the receiver DSP with Kramers-Kronig field reconstruction algorithm.

Consequent demodulation DSP can be implemented after digital down-sampling of the reconstructed field, including EDC, equalization, FOC, CPR, and de-mapping into original binary data. It is worth mentioning here that the purpose of up-sampling the data before applying the KK algorithm is to deal with the bandwidth broadening that happens because of the nonlinear operations, the square root and natural logarithm functions. This oversampling adds computational complexity to DSP implementation [57]. Nonetheless, a DSP-efficient implementation of the KK algorithm without up-sampling has been proposed in [58], with minimal performance penalty compared to the conventional algorithm discussed above [59].

1.3.3 Laser Phase and Intensity Noises and their Measurements

Laser sources transmit optical signals at a specific optical frequency, determined by the natural frequency of the lasing mechanism, and a specific optical power level. An ideal source would produce a constant-amplitude pure sinusoidal wave at a single optical frequency with an infinitesimal width in the frequency spectrum of the electric field of the light signal. The complex electric field of such an ideal signal can be expressed as

$$E(t) = E_0 e^{i\omega_0 t}, \quad (1.18)$$

where E_0 is the field amplitude, related to the signal optical power P_0 as $E_0 = \sqrt{P_0}$, and ω_0 is the optical angular frequency given by $\omega_0 = 2\pi c/n\lambda$, where c is the speed of light in vacuum, λ is the signal wavelength, and n is the refractive index of propagation medium. However, practical laser sources have amplitude and phase (frequency) perturbations around the average values for the power and center frequency of the generated optical signal, respectively. To include these noise components, the expression in Eq. (1.18) can be recast to

$$E(t) = E_0(t) \exp(i[\omega_0 t + \varphi(t)]), \quad (1.19)$$

where $E_0(t) = \sqrt{P(t)}$ is the time-dependent instantaneous field magnitude, and $\varphi(t)$ is the phase noise component, which is, like $E_0(t)$, a nondeterministic random perturbation that can be characterized by its statistical measures. The magnitude and phase perturbations are attributed in semiconductor lasers mainly to the spontaneous emission events inside the laser active cavity [30]. Other physical sources of intensity perturbations can be the reflections caused by externally-formed cavities in the optical system connected to the laser, like cavities created by multiple reflections between fiber connectors [60]. Typically, the intensity (magnitude) noise is characterized by the relative-intensity noise (RIN), defined as the ratio between the noise power spectral density (PSD) and the square of the average power and is usually measured in units of

dB/Hz (or dBc/Hz, referencing to the carrier power) [30,31]. If the optical signal is detected by a PD, the RIN can be calculated from the electrical signal as

$$RIN(f) = \frac{S_e(f)}{P_e} \quad (1.20)$$

where $S_e(f)$ is the electrical noise PSD resulting from the optical intensity noise and P_e is the average electrical power determined by the average optical power and PD responsivity. It should be noted here that in practical measurement of $S_e(f)$ the contributions of the instrumentation thermal noise and the signal-dependent shot noise should be subtracted from the total measured PSD at the electrical spectrum analyzer (ESA) [30]. Another parameter used for quantifying the RIN is by measuring the ratio between the statistical variance and the mean of the electrical signal from the PD, giving the average RIN, RIN_{avg} , i.e.,

$$RIN_{avg} = \frac{\sigma^2}{m^2} \quad (1.21)$$

where σ^2 and m are the variance and mean of the voltage $v(t)$ measured at the output of the PD receiver, respectively. Note that σ^2 is a function of the electrical bandwidth of the measurement, hence the measurement bandwidth should be specified when using RIN_{avg} to quantify the RIN.

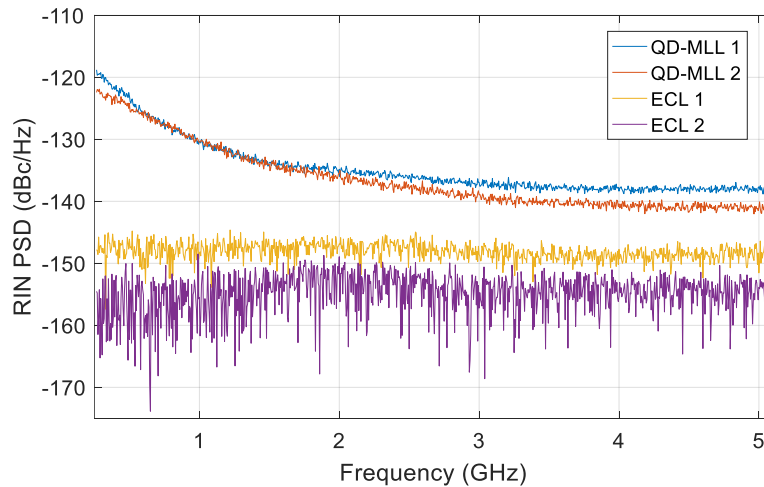


Fig. 1.6. RIN measurement of different practical lasers.

Figure 1.6 shows different examples of RIN measurements of practical lasers with different RIN spectral profiles. These are: individual comb lines from two different QD-MLLs; and two ECLs from different manufacturers. These measurements were obtained by a calibrated PD and an ESA, as given by Eq. (1.20), after subtracting the contributions from the instrumentation thermal noise and the PD shot noise on the measured PSDs.

The phase noise from a laser source is typically quantified by the spectral broadening of the optical field spectrum; namely, by the full-width at half-maximum (FWHM) linewidth of the spectrum of the envelope of the optical signal. This is also called the -3dB linewidth of the laser. Note that since the intensity perturbations are relatively small, the broadening of the spectrum of the optical signal from a laser is mainly attributed to the frequency (phase) modulation by the phase noise. The spectrum of the optical field can be measured after down-shifting the signal from the optical to the RF domain. This can be done by heterodyning the optical signal with another signal of a different optical frequency in a PD and measuring the spectrum of the beating tone by an ESA [30]. The optical signal can be self-heterodyned with a frequency-shifted and decorrelated version of itself in what is known as the *delayed self-heterodyne* setup [30,61,62]. In this case, the measured linewidth in the ESA is double the actual linewidth of the laser, because the resulting RF spectrum represents the frequency-domain convolution of the signal with its delayed version. Due to measurement resolution limitations, the spectrum width at low power levels (e.g., at -20 dB relative to the peak level) are measured and a Lorentzian function fitting is used to estimate the FWHM [30].

Spectral measurement of the linewidth does not reveal the temporal properties of the phase perturbations, which have significant importance in the impact on system performance in coherent communication application. An alternative way to characterize laser phase noise is by using digital

coherent receivers with real-time sampling oscilloscopes (RTSOs) to capture the beating tone of the laser signal with an optical LO [63,64]. Spectral and temporal characteristics of the phase perturbations can be obtained by offline processing of the phase noise trajectories (PNT) of the complex envelope of the captured waveforms. Figure 1.7 shows the time evolution and the spectrum of the measured phase noise from a distributed-feedback (DFB) laser. The measurement setup is similar to that shown in Chapter 2, with an ECL used as the LO at the coherent receiver.

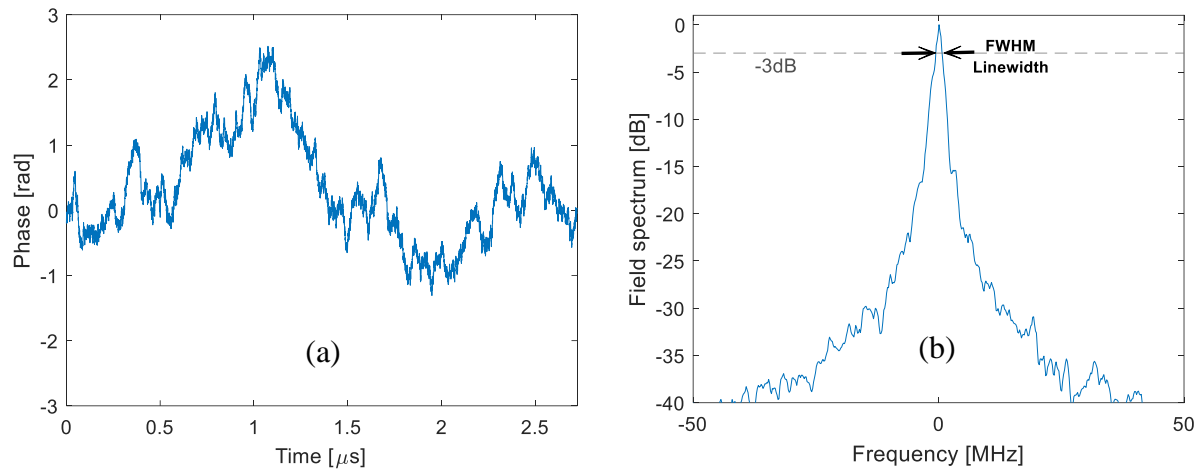


Fig. 1.7. (a) Time evolution of the phase and (b) the field spectrum of a DFB laser obtained by a coherent receiver.

RIN is one of the factors that may limit the performance of optical communication systems due to the interference of the random noise intensity variations with the information-carrying variations modulated on the intensity of the optical signal. The effect of RIN on transmission performance becomes seriously detrimental when it has high spectral components extending to frequency ranges comparable to the symbol rate of data transmission. Phase noise has significant effects on the performance of coherent transmission systems that utilize the phase of the optical signal for data modulation, and should be addressed very carefully in system design. Figure 1.8 shows the constellation diagrams of numerical simulations of a 28 GBd 16-QAM signal with a signal-to-noise ratio (SNR) of 23 dB without and with the effect of the phase noise from a single

laser with a 100 kHz linewidth. Note that the QAM symbols are severely displaced from their original locations and symbol decisions cannot be made without phase noise correction by CPR.

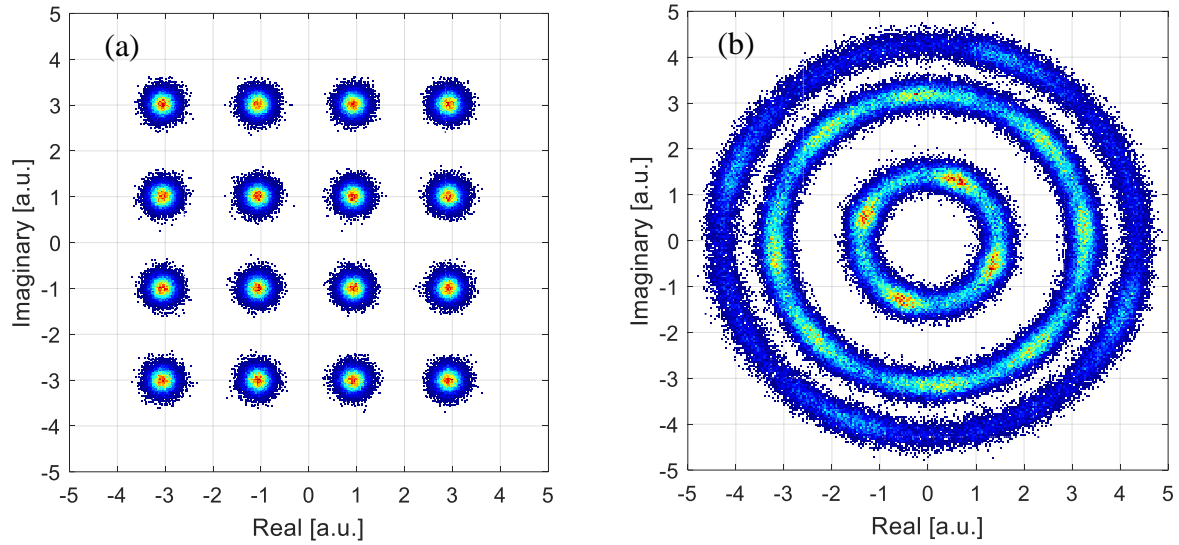


Fig. 1.8. Constellations of a 16-QAM signal at 28 GBd and SNR of 23 dB (a) without and (b) with the effect of phase noise from a laser with a linewidth of 100 kHz. Burst length = 2×10^5 symbols.

The impact of the phase noise in a digital coherent system is determined by three major factors: the modulation type, the transmission symbol rate, and the linewidths of the transmitter and LO lasers. In the next chapter, however, it will be shown that a more detailed study of the phase noise characteristics is required to accurately estimate system performance in presence of phase noise.

Chapter 2

Spectral Properties of Phase Noise and the Performance of Digital Coherent Systems

In this chapter we study the measurements the FM-noise power spectral density of different lasers and compare this to their measured linewidths as predictors of performance in a digital coherent system. Investigation of system performance with simulations based on the measured phase sequences and back-to-back coherent transmission experiments show that QD-MLLs with linewidths of several MHz can have comparable performance to that of a laser with only a few hundreds of kHz of Lorentzian linewidth, due to the non-white part of their FM noise. We show that spectral linewidths of lasers with similar spectral properties can underestimate their performance in coherent systems, regardless of the linewidth measurement technique used. We propose a “*Lorentzian-equivalent linewidth*” measure to characterize lasers with non-white FM noise and to estimate their impact in digital coherent optical systems. This measure is obtained from phase variations at frequencies higher than typical frequencies often used to characterize lasers with white FM noise, and comparable to the system baud. The proposed measure is shown to be a better predictor of system phase noise-related performance than the measured linewidth, for lasers with non-white FM noise. The impact of non-white FM noise on the optimization of carrier phase recovery and system performance is also discussed.

2.1 Introduction

Since its commercial introduction in 2008, digital coherent transmission has become a dominant technology for optical transport and datacenter interconnect (DCI). Continued progress in optical, electro-optic and application-specific integrated circuit (ASIC) technologies enable coherent transmission for short reach low power applications [21,65-67]. These are expected to include intra-DCIs, next-generation passive optical networks (NG-PONs) and modern mobile network backhaul/fronthaul systems. Laser phase noise can limit coherent transmission performance [4,5,23,68]. This noise, together with some phase noise induced by non-linear transmission, is tracked by a carrier phase recovery (CPR) circuit implemented in digital signal processing (DSP) at the receiver. The associated transmission signal-to-noise ratio (SNR) penalty is proportional to the amount of phase noise induced by the transmitter (Tx) and receiver (Rx) lasers. Laser phase noise is often characterized by a spectral linewidth, as a full-width at half-maximum (FWHM) of the power spectral density (PSD) of the unmodulated optical signal. A narrow laser linewidth, corresponding to low phase noise, can result in better system performance. Given this phase noise measure, laser linewidth \times symbol period product ($\Delta\nu \cdot T_s$) is often used to estimate laser phase noise related system performance limit [4,5,68-76]. In practice, the tolerable value of $\Delta\nu \cdot T_s$ depends on the CPR algorithm in use, modulation format, as well as the SNR margin of the system. Based on the $\Delta\nu \cdot T_s$ product criterion, combined Tx and Rx laser linewidth must decrease with symbol rate to preserve CPR performance. Narrow linewidths can lead to higher laser part costs that may compromise the feasibility of the aforementioned applications at low baud. Furthermore, although coherent systems are typically required to operate at high symbol rates (e.g., 28 GBd or higher), digital subcarrier multiplexing [21] within each wavelength channel is sometimes used to enhance system resilience to different channel impairments and this reduces the symbol rate of

each subcarrier. Therefore, more in-depth investigations of the opportunities of using the currently available laser technologies in these different applications are warranted.

Distributed-feedback (DFB) lasers and external cavity lasers (ECLs) are used in communication applications. These lasers generally have white frequency modulation (FM) noise PSD, $S_{FM}(f)$, and, consequently, have a phase noise that can be suitably characterized by the FWHM, $\Delta\nu$, of their Lorentzian optical PSD [61,63,64,77]. Other types of lasers, notably quantum-dot(dash) mode-locked lasers (QD-MLLs), have a non-white FM noise PSD and, consequently, their optical PSD is not Lorentzian. QD-MLLs are multi-wavelength (comb) sources and are attractive for multi-channel applications. For these lasers, linewidth does not adequately specify the phase noise that is operative in coherent systems at different symbol rates. Thus, the $\Delta\nu \cdot T_s$ measure does not apply in assessing phase noise related system performance [77]. In this study, detailed analysis about the impact of non-white FM noise in digital coherent system performance is reported for the first time. A blind phase search (BPS) and the M th-power CPR are used and compared in the system performance study. Their optimization is considered in the light of linewidth and FM noise PSD.

2.2 Laser Phase Noise Characterization

2.2.1 General Characterization

As was mentioned in Chapter 1, for the phase noise caused by spontaneous emission, phase evolution of an optical field is a random stochastic process. In the absence of intensity noise, the normalized optical field at a laser output is $E(t) = \exp\{i[\omega_0 t + \varphi(t)]\}$, where ω_0 is the optical angular (carrier) frequency and $\varphi(t)$ is the phase noise. Typically, the phase noise is constrained by specifying a FWHM linewidth, $\Delta\nu$, of the PSD of the envelope of $E(t)$, $S(f)$. This can be

measured, for example, with a delayed self-heterodyne (DSH) detection [61] or phase noise trajectory (PNT) digital methods [63,64]. In a measurement system, when $\varphi(t)$ is sampled at a sampling period of τ , the *phase difference* between adjacent samples is

$$\Delta\varphi_\tau(t) = \varphi(t) - \varphi(t - \tau) \quad (2.1)$$

This phase difference is a zero-mean Gaussian process with a variance of $\sigma_\varphi^2(\tau)$, which can be used to quantify the phase noise. The corresponding FM noise is defined as

$$\Delta f(t) = \frac{\Delta\varphi_\tau(t)}{2\pi\tau}, \quad (2.2)$$

and the variance $\sigma_\varphi^2(\tau)$ is related to the FM noise by [64]:

$$\sigma_\varphi^2(\tau) = 4 \int_0^\infty \left(\frac{\sin(\pi f \tau)}{f} \right)^2 S_{FM}(f) df \quad (2.3)$$

where $S_{FM}(f)$ is the PSD of FM noise $\Delta f(t)$.

When $\varphi(t)$ is a Wiener process with $\Delta\varphi_\tau(t)$ a zero-mean “white” Gaussian process, $S_{FM}(f)$ should also have a white profile, according to Eq. (2.2). In this case, the integration in Eq. (2.3) results in $\sigma_\varphi^2(\tau) = 2\pi^2 \tilde{S}_{FM} \tau$, where \tilde{S}_{FM} is a frequency-independent FM spectral density, and the PSD of $E(t)$ has a Lorentzian shape given by

$$S(f) = \frac{\Delta\nu}{2\pi \left[f^2 + \left(\frac{\Delta\nu}{2} \right)^2 \right]} \quad (2.4)$$

where $\Delta\nu = \pi \tilde{S}_{FM}$ is the FWHM of the Lorentzian function [64]. Therefore, in this model $\Delta\nu$ is linearly related to $\sigma_\varphi^2(\tau)$ for a given τ as

$$\sigma_\varphi^2(\tau) = 2\pi\Delta\nu\tau \quad (2.5)$$

It can be inferred from Eq. (2.5) that in this model the measurement of $\Delta\nu$ based on $\sigma_\varphi^2(\tau)$ is independent of the parameter τ , because the variance $\sigma_\varphi^2(\tau)$ itself is linearly proportional to τ (a

well-known property for a Wiener process). Thus, for white FM noise and Lorentzian optical PSD, $\Delta\nu \cdot \tau$ determines phase noise variance. If, on the other hand, $S_{FM}(f)$ is not white, Eqs. (2.4) & (2.5) no longer apply and the variance given by Eq. (2.3) is no longer linear with τ . Instead, $\sigma_\phi^2(\tau)$ at every value of τ will depend on the specific spectral profile of $S_{FM}(f)$, as will be shown next.

2.2.2 Characterization of Lasers with Non-white FM Noise

Although many DFB lasers and ECLs have white FM noise spectra, not all practical lasers for coherent detection have the same characteristics. QD-MLLs and sampled-grating distributed Bragg reflector (SGDBR) lasers are examples of semiconductor lasers with non-white FM noise PSDs [78-81]. These have relatively high FM noise PSDs at the low frequency region below tens of MHz. A contrasting example is the *differential* phase noise between adjacent spectral lines of a QD-MLL, whose FM noise PSD in the low frequency region (below 10 MHz) can be an order of magnitude lower than that at frequencies around 1 GHz [82]. Measurements of different FM noise PSD profiles will be presented in the following section.

With a semi-analytic model supported by experimental demonstration, it was suggested in Refs. [83,84] that $\Delta\nu$ can be estimated by integrating $S_{FM}(f)$ only in the low frequency region from DC up to the point of intersection between $S_{FM}(f)$ and an FM index line given by $(8 \log(2)f)/\pi^2$. This line is called the *β -separation line* and is shown as a dashed line in Fig. 2.1(a). Similarly, another model based on the power area method was also introduced in Ref. [85], which agrees with the findings in Ref. [83]. High frequency contents of $S_{FM}(f)$ mainly contribute to the wings of $S(f)$ at frequencies higher than those used to evaluate the FWHM spectral linewidth. On the other hand, Eq. (2.3) indicates that the variance $\sigma_\phi^2(\tau)$ depends on $S_{FM}(f)$ at all frequencies. Thus, two lasers with the same $\sigma_\phi^2(\tau)$ when evaluated at the same interval τ can have

different $\Delta\nu$ if their $S_{FM}(f)$ spectra are not the same. For the impact in the coherent system performance, CPR-related penalty is more sensitive to the untracked part of the carrier phase, largely determined by the high frequency region of $S_{FM}(f)$.

We use $\sigma_\phi^2(\tau)$ evaluated at the system symbol interval (i.e., at $\tau = T_s$) to bound coherent CPR-related penalty for lasers with non-white FM noise. The choice of symbol interval stems from the fact that CPR algorithms operate on T_s -spaced samples. However, signal to noise ratio constraints in the measurement setup may limit the feasible choice of τ to values longer than T_s in practical systems, as will be shown below. For comparison with laser sources with Lorentzian-only phase noise, the variance $\sigma_\phi^2(\tau)$ of non-Lorentzian phase noise can be represented by a *Lorentzian-equivalent linewidth* (LEL) by means of Eq. (2.5). We will show that, once optimized for a given non-white FM noise, the CPR algorithm performance is very close to that of a white FM noise laser with linewidth equal to the specified LEL [77].

Following this discussion, Fig. 2.1 shows numerically-generated phase noise with white PSD profile before (blue) and after (yellow and orange) applying spectral modifications to produce non-white FM noise. In this example, the spectral modification mask is applied to enhance the low-frequency components of $S_{FM}(f)$ with a factor of G up to a specific frequency F_l . A slope of -10 dB/decade is used for the transition between the low-frequency region (up to F_l Hz) and the high-frequency region (starts at F_2 Hz) of the spectrum. 2 million white phase noise samples were generated in the simulation at 20 GS/s with an ideal Lorentzian linewidth of 1 MHz ($\sigma_\phi^2(\tau) = \pi \times 10^{-4} \text{ rad}^2$). Two different examples of spectral modification masks are applied with $\{F_l, G\} = \{10 \text{ MHz}, 20\}$ and $\{F_l, G\} = \{50 \text{ MHz}, 10\}$, labeled as “Modified 1” and “Modified 2” in Fig. 2.1, respectively, to represent two different lasers with non-white FM noise characteristics. The phase difference variance $\sigma_\phi^2(\tau)$ was re-set to its original value ($\pi \times 10^{-4} \text{ rad}^2$) after applying the

spectral modification. Note that since the frequency is shown in logarithmic scale, PSD reduction at high frequencies is barely noticeable. Figure 2.1(b) displays the optical field PSDs corresponding to the three FM noise PSDs in Fig. 2.1(a), showing significant FWHM linewidth $\Delta\nu$ enhancement due to the increase of low frequency FM noise components. With the FM noise spectral modification, $\Delta\nu$ is increased from 1 MHz to >8 MHz despite the same value of $\sigma_\phi^2(\tau)$. $\Delta\nu$ of each spectrum in Fig. 2.1(b) was estimated through Lorentzian fitting, commonly used in DSH or a coherent receiver setup, by measuring the -20-dB linewidth $\Delta\nu_{-20dB}$ so that $\Delta\nu = \Delta\nu_{-20dB}/\sqrt{99}$ [86,87].

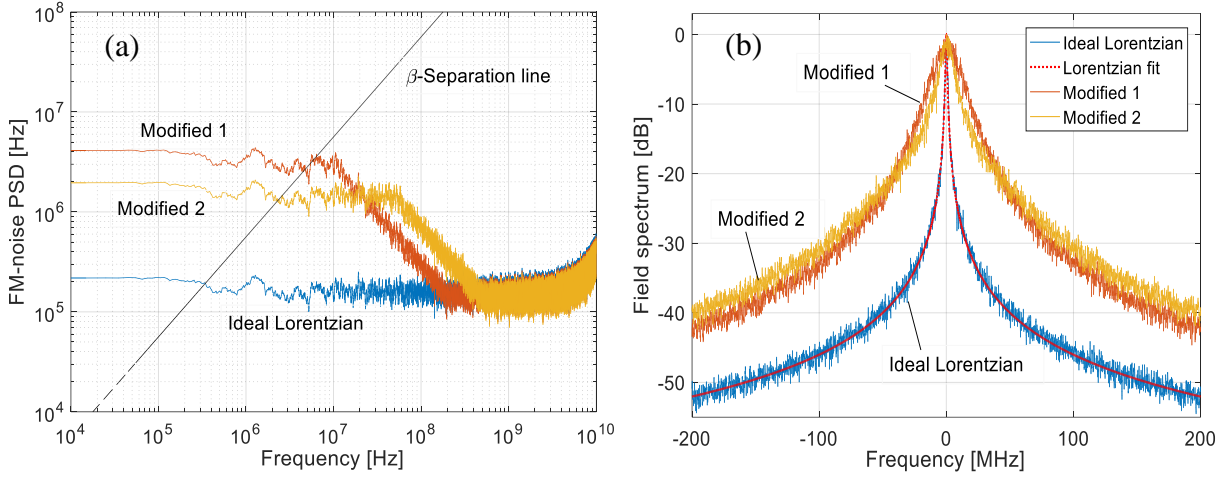


Fig. 2.1. (a) Simulated FM noise PSDs before (blue) and after (yellow and orange) spectral modifications; and (b) corresponding optical field spectra (each normalized to its maximum PSD).

Figure 2.2(a) shows the LELs evaluated by Eq. (2.5) at different sampling intervals of τ . The value of τ was changed by decimating the phase sequences which were originally generated at a high sampling rate of 20 GS/s. No anti-alias filtering was used in this process because we are interested in studying the relation between $\sigma_\phi^2(\tau)$ of the non-white FM noise and the sampling frequency while avoiding possible measurement bandwidth limitation that would underestimate the actual phase variance [87]. Note that we will use the term “sampling frequency” hereinafter (with a unit of Hz) to represent $1/\tau$ of decimated sequences, not to be confused with the sampling

rate (with a unit of Sample/s) used to generate the original phase sequences (or to acquire digital sequences in a measurement setup).

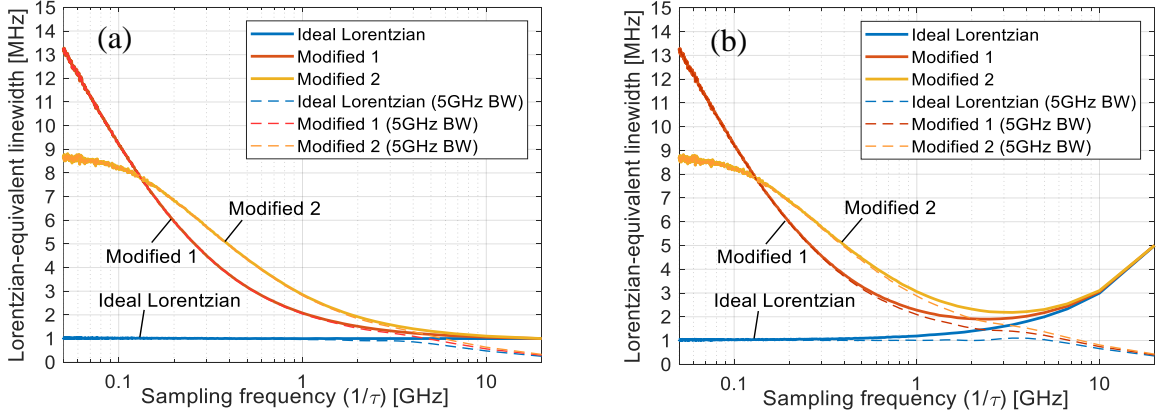


Fig. 2.2. Lorentzian-equivalent linewidths of the phase noise sequences used to obtain Fig. 2.1, (a) without and (b) with the effect of additive instrumentation noise included. BW: bandwidth.

As expected, the results show that for the white FM noise, the linewidth (1 MHz in this case) is obtained from phase variance through Eq. (2.5) independent of the sampling frequency. Thus, a low-speed digital receiver with a bandwidth of only a few hundred MHz may suffice for characterizing the phase noise through linewidth estimation [64]. On the other hand, the measured LEL can vary drastically with the change of sampling frequency for non-white FM noise. Therefore, much higher sampling frequencies are required to evaluate $\sigma_\phi^2(\tau)$ at frequencies comparable to the symbol rate in practical coherent systems (usually >5 GBd). Ideally, sampling the phase noise information at the transmission symbol rate would be desirable to measure the phase noise variance for assessing the CPR performance, which operates typically on T_s -spaced samples, as will be demonstrated in Sec. 2.4. However, additive noise commonly exists in the measurement setup (induced by, e.g., photodiode shot noise, and electronic circuit noise) can drastically overestimate the measured phase noise variance if wide measurement bandwidths are used [87]. Thus, limiting the measurement bandwidth is also required to reduce the impact of instrumentation noise. Nevertheless, Fig. 2.2(a) shows that even with non-white FM noise, the

LELs evaluated at 5 GHz sampling frequency can be reasonably accurate to represent high frequency $\sigma_\phi^2(\tau)$. In fact, limiting the signal bandwidth to 5 GHz (± 2.5 GHz) affected the measurement of the LEL only marginally at the sampling frequency ($1/\tau$) of 5 GHz. Figure 2.2(b) shows the effect of additive noise on the measurement with and without applying the 5 GHz bandwidth limitation. In the simulation, before extracting the signal phase, instrumentation noise was added to the unity power signal optical field with a white Gaussian PSD of -68 dB/Hz for the real and imaginary parts; resulting in a total SNR of 35 dB over a 10 GHz bandwidth. Even with this high SNR, the LELs at 20 GHz were overestimated by approximately 400%. Limiting the measurement bandwidth to 5 GHz resulted in more accurate estimation of the LEL at the 5 GHz sampling frequency for all three examples of FM noise used in this simulation, with only ~23% of average overestimation. In practice, the optimum measurement bandwidth will depend on the level of the additive noise and the specific phase noise characteristics of the laser. However, the examples here suggest that a sampling frequency of 5 GHz is sufficient in setups used to measure the LELs for lasers of similar non-white FM noise profiles with the wide range of $\{F_l, G\}$ parameters used for the examples shown in Fig. 2.1. This also dictates that a digital receiver with a sampling rate of at least 5 GS/s is required for the characterization purpose.

2.3 Experimental Setup and Laser Phase Noise Measurements

Several lasers with different measured FM noise PSDs were used in this experimental study. These include: an ECL; a DFB laser; and two single-section InAs/InP QD-MLLs with different repetition frequencies. QD-MLLs are mode-locked laser sources that produce multiple spectral lines with equal spacing over a wide range of wavelengths [78,88]. Their application has been demonstrated in multiple-lane and WDM systems [89-92]. Both QD-MLLs used in this work operate in the C-band with 11-GHz and 25-GHz frequency spacing between adjacent spectral lines, hereinafter

denoted by “11G-MLL” and “25G-MLL”, respectively. A phase-diversity coherent receiver, comprising a 2×4 optical hybrid, two balanced photodetectors and transimpedance amplifiers, was used to down-shift the complex field envelope of the optical signal to the RF domain through heterodyne detection [63,64], as shown in Fig. 2.3. The local oscillator (LO) is a tunable ECL with <50-kHz linewidth. A 1-nm tunable optical bandpass filter was used to select only a few spectral lines when measuring QD-MLLs. This was followed by a polarization controller to maximize the mixing efficiency between the laser under test (LUT) and the LO. A dual-channel real-time sampling oscilloscope (RTSO) operating at 50 GS/s with 23-GHz RF bandwidth was used to capture the in-phase (I) and the quadrature-phase (Q) components of the RF beat tone. Multiple sets of data, each of 10^6 samples, were recorded from each LUT over 20 μ s of measurement time. Offline PC processing in MATLAB was used for phase noise analysis and CPR performance estimation [64].

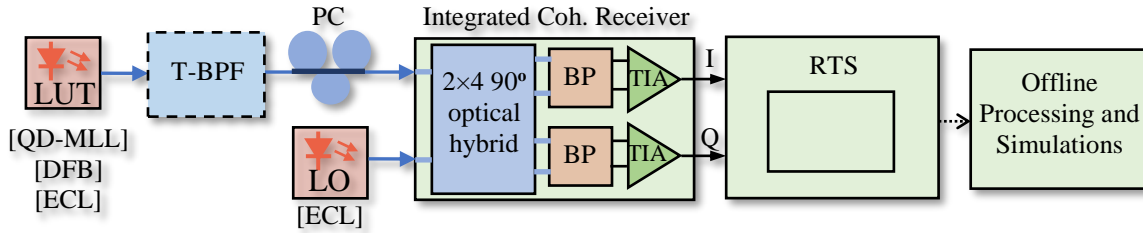


Fig. 2.3. Schematic of the experimental setup used for phase noise acquisition. T-BPF: tunable bandpass filter; PC: polarization control; BPD: balanced photodetector.

To process the signal, the intermediate frequency (IF) of each captured RF waveform was shifted to the origin and the bandwidth of the heterodyne complex beat tone was then limited by a 5 GHz ideal brick-wall filter. Signal optical phase $\varphi(t)$ was then obtained by unwrapping the phase of the trajectories of recorded sample points.

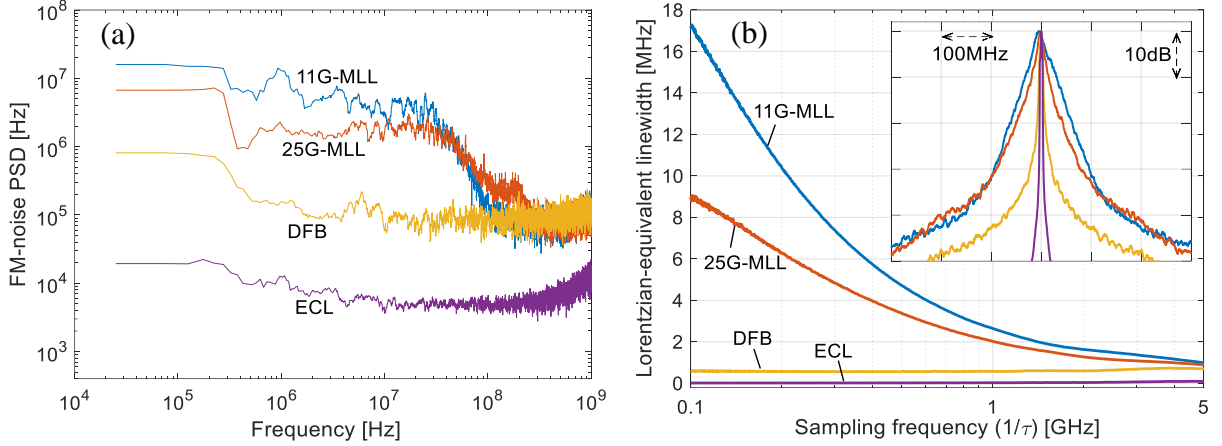


Fig. 2.4. (a) Experimental FM-noise PSD for different lasers, and (b) Lorentzian-equivalent linewidths calculated at different sample interval τ . Inset in (b) shows the corresponding field spectra.

Figure 2.4(a) shows the $S_{FM}(f)$ profiles of the 4 lasers used in this experiment. Both the ECL and the DFB lasers have relatively flat PSD profiles. In contrast, both QD-MLLs exhibit more than an order of magnitude higher PSDs in the low-frequency region extending up to tens of MHz, compared to those at the high frequency region around 1 GHz. It is important to note that these results are a property of the QD-MLLs used in this investigation [77,79], not to be confused with the enhancement of $S_{FM}(f)$ at low frequencies stemming from extended measurement times and reported elsewhere (e.g., Ref. [64]). Figure 2.4(b) shows the LELs calculated from $\sigma_\phi^2(\tau)$ evaluated at different sampling intervals. Here τ was changed by decimating the phase sequence $\phi(t)$ originally captured at 50 GS/s. Due to their white FM noise, the ECL and DFB laser used in this experiment have relatively constant LELs over the entire sampling frequency range. In comparison, the LELs of QD-MLLs vary by a factor of >10 within the same sampling frequency range. FWHM linewidths, $\Delta\nu$, measured from the PSDs of the beat tones, shown in the inset of Fig. 2.4(b), were comparable to the LELs calculated at the lowest sampling frequency of 0.1 GHz for all lasers. This is because low sampling frequencies are closer to the flat low-frequency region of the FM-noise PSDs (see Fig. 2.4(a)) for these lasers, which is closely related to the FWHM

linewidths, as was explained in Sec. 2.2. The results in Fig. 2.4 illustrate the ambiguity of $\Delta\nu$ as a parameter to describe phase noise of lasers with non-white FM noise. Furthermore, the QD-MLLs with $\Delta\nu$ values of 17 MHz and 9 MHz for the 11G-MLL and the 25G-MLL, respectively, have LELs of 1 MHz and 900 kHz near 5 GHz sampling frequency, comparable with the 700 kHz linewidth of the DFB laser. Note that if τ is equal to the symbol period T_s in a digital coherent receiver, the abscissa in Fig. 2.4(b) represents the symbol rate of the system. In the next section, we show that despite their relatively large FWHM linewidths, QD-MLLs exhibits similar performance as the DFB laser in coherent systems at practical symbol rates.

2.4 Performance in Digital CPR Algorithms

Digital CPR algorithms can be implemented in single or multiple stages and they vary in performance and implementation complexity. For example, feed-forward CPR algorithms are practical and often used at high symbol rates [68-76]. These schemes typically use the blind phase search (BPS) [4] and/or the M th-power [70] algorithm as the main (or the only) functional stage. These two schemes are feed-forward schemes, hence convenient for parallel hardware implementations. Details about the structures and working mechanisms of these algorithms can be found in Ref. [4] and Ref. [70]. As such, we restrict our CPR performance evaluations to these two feed-forward methods. Without loss of generality, differential QAM encoding/decoding will be used to accommodate any quadrant jump events (or cycle slips) resulting from excess phase noise. Differential encoding induces unwanted optical SNR (OSNR) penalty overhead. However, differential encoding can be avoided only when the probability of cycle slip is very low ($\sim 10^{-18} <$ target post-FEC BER), which can be attained only in systems operating at high symbol rates and with high-quality lasers of very low phase noise [69].

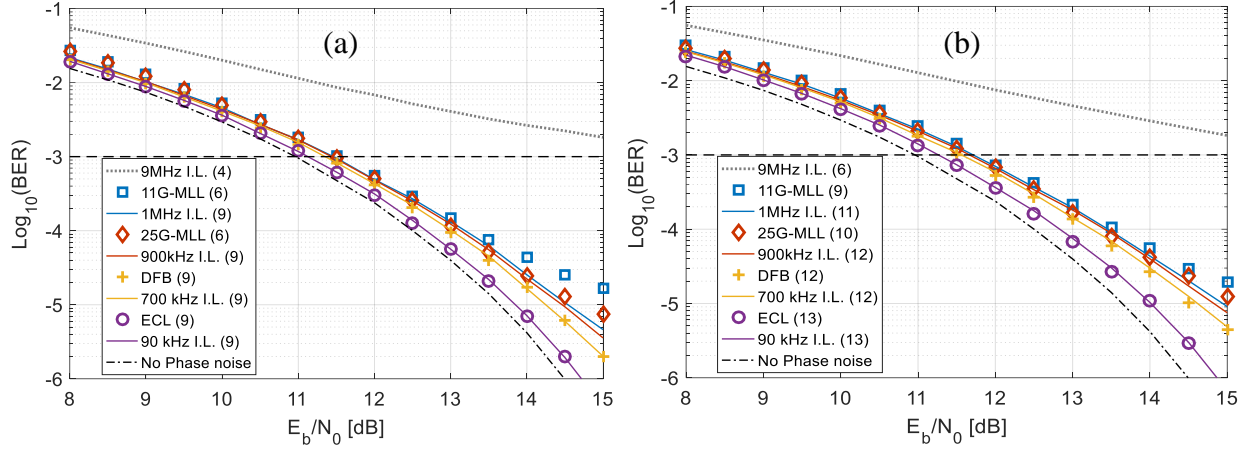


Fig. 2.5. Simulated BER performance for differential 16-QAM at 10 GBd for the measured phase noises and ideal Lorentzian phase noises with (a) BPS and (b) M th-power CPR. Optimum half-window length used for each case is shown in the parenthetical numbers in the legends. I.L.: Ideal Lorentzian.

In this study, measured phase sequences $\varphi(t)$ from all lasers were down-sampled by decimation to 10 GS/s and imposed on differentially-encoded 16-QAM symbols for system performance simulation. The signal-to-noise ratio per bit (E_b/N_0) was varied in the simulation by loading additive white Gaussian noise to the modulated signal before CPR and symbol-to-bit differential de-mapping. Perfect frequency offset compensation and symbol-timing recovery were asserted in the simulation to restrict the investigation to the penalty caused by residual phase noise only. A single-stage BPS with $B = 64$ test points was used [4]. The M th-power CPR algorithm is a constellation-partitioned 4th-power algorithm with sliding window [70]. The averaging window size was optimized in both CPR algorithms around the value of E_b/N_0 that results in $\text{BER}=10^{-3}$ for every laser. Simulated 10 GBd BER performance versus E_b/N_0 is shown in Fig. 2.5. To compare the system BER performance, ideal Lorentzian phase noises were generated numerically with the FWHM linewidths equal to the measured LELs of the LUTs evaluated at 5 GHz (see Fig. 2.4(b)). At least 5 million QAM symbols were simulated and 100 bit errors were counted for each data point for BER estimation. Also shown in Fig. 2.5 is the simulated BER performance of ideal Lorentzian phase noise with the FWHM linewidth equal to the FWHM linewidth of the 25G-MLL

($\Delta\nu = 9$ MHz). As a reference, the dotted-dashed curve in Fig. 2.5 shows the BER performance in the absence of laser phase noise.

The performances of both MLLs are very close to the ideal Lorentzian phase noises with FWHM linewidths equal to the LELs of MLLs sampled at 5 GHz, except for BER floors observed at values below 10^{-5} (\ll typical FEC thresholds) for MLLs. For the MLLs with strong low-frequency FM noise PSDs, FWHM linewidths, mainly determined by the low-frequency components, significantly overestimate the system impact of phase noise. In fact, for a FWHM linewidth of 17 MHz, the product " $\Delta\nu \cdot T_s$ " of this system would be 1.7×10^{-3} , which is an order of magnitude higher than a reported limit of 1.4×10^{-4} for 16-QAM for a SNR penalty of 1 dB (based on the ideal Lorentzian model) for both CPR schemes [4,70]. Whereas system performance of the 11G-MLL with 17 MHz FWHM linewidth is comparable with the DFB laser of a FWHM of only 700 kHz. These results indicate that if FM noise is non-white, laser phase noise cannot be characterized by the FWHM linewidth, and the " $\Delta\nu \cdot T_s$ " criterion is not adequate to assess phase-noise-induced system penalty.

To further confirm these results, we used the 25GHz-MLL in a back-to-back (B2B) coherent communication experiment and compared it to an ECL as the Tx light source. A single comb line at 1537.34 nm wavelength was used to carry a differentially encoded Nyquist 16-QAM signal at 5 GBd with a roll-off factor of 0.1. The choice of this relatively low symbol rate was intentionally made to demonstrate the concept at an extreme condition. The output from the bandpass filter in Fig. 2.3, representing the selected comb line, was amplified by an Erbium-doped fiber amplifier (EDFA) and fed into an optical I/Q modulator followed by another EDFA and noise loading stage to change the OSNR of the modulated signal. The optical signal is then passed through a bandpass filter and sent to a polarization control and consequently the coherent receiver.

The rest of the setup is the same as shown in Fig. 2.3. The I and Q components of the received signal were captured by the RTSO at a rate of 25 GS/s and processed offline. The offline receiver DSP comprised resampling to 2 Sam/Sym, frequency offset compensation, root-raised cosine matched filtering, symbol timing recovery, adaptive equalization, CPR, and differential symbol-to-bit de-mapping for BER counting. The BPS with $B = 64$ was used for CPR. The QD-MLL was then replaced by an ECL similar to the one used as the LO (with a linewidth of <50 kHz) in the transmission experiment for comparison.

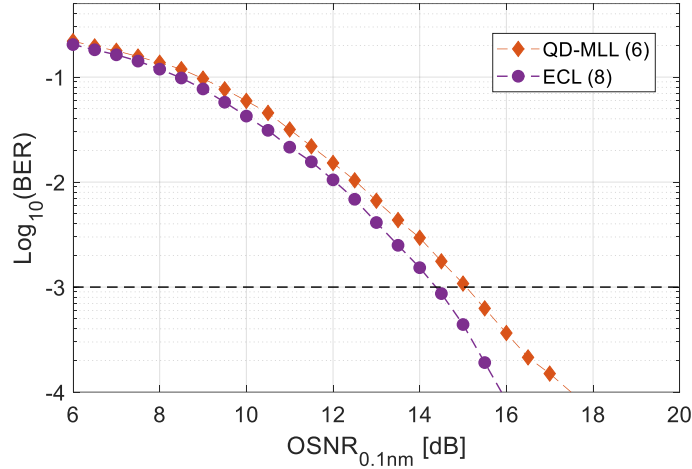


Fig. 2.6. Experimental B2B BER performance as a function of OSNR with differential 16-QAM at 5 GBd for the 25GHz-MLL and an ECL at the Tx side. BPS was used as the CPR with $B = 64$. Parenthetical numbers in the legend represent the optimum half-window length used for each case.

Figure 2.6 shows the BER as a function of OSNR for both the QD-MLL and the ECL as the Tx light sources. The OSNR penalty of using the QD-MLL at BER of 10^{-3} is only ~ 0.7 dB compared to the case of the ECL. This result comes in line with the semi-numerical simulation results shown in Fig. 2.5. This result also demonstrates the feasibility of adopting QD-MLLs for relatively low-baud coherent applications despite their broad linewidths.

The results presented above show that for a laser with non-white FM noise, the LEL is dependent on the measurement sampling frequency, and the impact of phase noise in a coherent

system is more relevant to the LEL evaluated at a relatively high sampling frequency. Next, we investigate how the accuracy of SNR penalty estimation is affected by the choice of sampling frequency in the measurement of LEL.

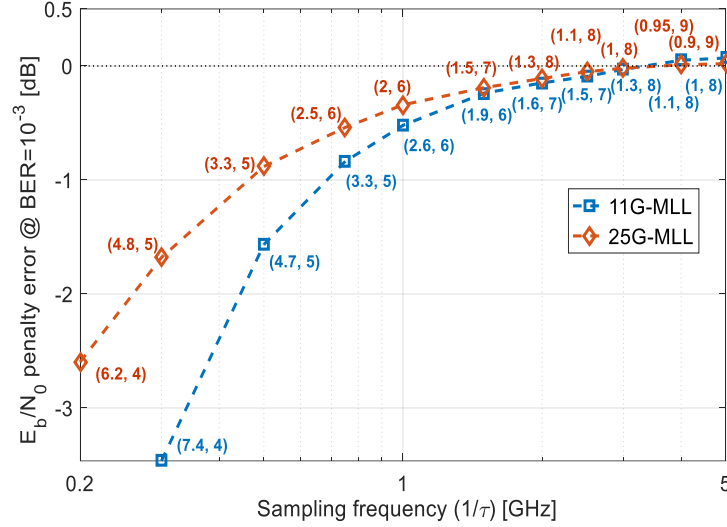


Fig. 2.7. Simulated E_b/N_0 penalty error between the actual performance and the LEL estimates as a function of sampling frequency. Numbers in parentheses represent the Lorentzian-equivalent linewidth in MHz and the optimum half-window length used in the BPS CPR, respectively.

Figure 2.7 shows the system penalty error of using Lorentzian-equivalent linewidth measured at different sampling frequencies. The system penalty error is defined as the difference of the required E_b/N_0 (to achieve $\text{BER}=10^{-3}$) between using the actual phase noise $\varphi(t)$ of the MLLs and the numerically generated ideal Lorentzian phase noises with FWHM linewidths equal to the LELs obtained from $\varphi(t)$ decimated at different sampling frequencies. BPS was used for CPR and with optimized averaging window size for each case. The penalty errors shown in Fig. 2.7 diminish at relatively high sampling frequencies of higher than 3 GHz, which agrees with the results suggested by Fig. 2.2 for measuring LELs. Thus 5 GHz sampling frequency is generally sufficient for accurately characterizing this type of lasers for use in coherent systems. This result comes in contrast to the case of a laser with white FM noise (e.g., DFB or ECL), in which FWHM

linewidth is always equal to the LEL, independent of the sampling frequency, and thus a receiver with a few hundred MHz bandwidth would be sufficient [63], [64].

2.4.1 Impact of Non-white FM Noise on Averaging Window Length

In general, all CPR algorithms in digital coherent receivers average the phase estimates over an adequate number of consecutive symbols, or window length, to reduce the effect of additive noise on the phase estimation accuracy. A longer window reduces the influence of additive noise, but also averages out instantaneous phase variations within the window and reduces the accuracy of phase estimation. Thus, window length is optimized for different phase noise and additive noise levels to achieve the best effect. It can be noted from the legends in Fig. 2.5 that the optimum window size is shorter for the case of non-white FM noise, compared to the ideal Lorentzian phase noise of the same Lorentzian-equivalent linewidth. To explain this effect, we consider non-white FM noise on a QPSK modulated optical signal (or, equivalently, 4-QAM), and apply the M th-power algorithm, in which the phase estimate at the k th symbol is calculated as

$$\hat{\phi}(k) = \frac{1}{4} \arg \sum_{m=k-l}^{m=k+l} (r_m)^4 \quad (2.6)$$

where $r_m = d_m + n_m$ is the m th received complex symbol consisting of the data symbol with phase noise (d_m) and an additive zero-mean noise (n_m), and the window length is $N = 2l + 1$. For a non-white FM noise with strong low-frequency components, the mean phase averaged over a certain window length will vary more compared to white FM noise scenario with equal phase variance σ_ϕ^2 . This increased variation of averaged phase will likely to require a shorter averaging time window to optimize the system performance. This can be clearly observed in the absence of additive noise. With the consideration of additive noise as a random process statistically

independent of the phase noise, the total mean squared error of the phase estimate can be approximated as

$$\sigma_{err}^2(N) \cong \langle e_{\hat{\varphi},n}(k, N)^2 \rangle + \langle e_{\hat{\varphi},pn}(k, N)^2 \rangle \quad (2.7)$$

where the phase estimate total mean squared error $\sigma_{err}^2(N)$ represents the variance of the difference between the Tx-Rx combined laser phase noises and the estimated phase, i.e., $\sigma_{err}^2(N) = \text{var}[\varphi(k) - \hat{\varphi}(k, N)]$, $\langle e_{\hat{\varphi},n}(k, N)^2 \rangle$ is the variance of phase *estimate error* induced by the additive noise in absence of phase variations within the averaging window N , and $\langle e_{\hat{\varphi},pn}(k, N)^2 \rangle$ is the variance of phase *estimate error* induced by instantaneous phase noise variations within the averaging window N in the absence of additive noise. According to Eq. (2.6), these quantities can be evaluated as

$$\langle e_{\hat{\varphi},n}(k, N)^2 \rangle = \text{var}[e_{\hat{\varphi},n}](N) = \text{var} \left[\frac{1}{4} \arg \sum_{m=k-l}^{m=k+l} (1 + n_m)^4 \right] \quad (2.8)$$

$$\langle e_{\hat{\varphi},pn}(k, N)^2 \rangle = \text{var}[e_{\hat{\varphi},pn}](N) = \text{var} \left[\varphi(k) - \frac{1}{4} \arg \sum_{m=k-l}^{m=k+l} e^{i4\varphi(m)} \right] \quad (2.9)$$

We emphasize on that $\sigma_{err}^2(N)$ in Eq. (2.7) is only an approximation and the exact mean squared error is not a straightforward summation of the presented terms; nonetheless, it will be shown next that this is a very good approximation and it gives exact results in terms of the values of N at which minimum values of $\sigma_{err}^2(N)$ occur, which is the main focus of this analysis. The received symbols in Eq. (2.8) are assumed here to have a unity power and a mean phase of 0 for simplicity. However, any constant mean phase value could have been assumed without changing the results (e.g., $\pi/4$ for 4-QAM). The additive noise, n_m , is modeled as a complex Gaussian random sequence of zero mean and variance of $1/(2SNR)$ for both the real and the imaginary parts. Figure 2.8 shows the numerical evaluations of Eqs. (2.7)-(2.9) for ideal Lorentzian phase noise with $\Delta\nu = 500$ kHz and non-white FM noise of the same variance generated by using the spectral

modification parameters $\{F_l, G\} = \{50 \text{ MHz}, 10\}$ as was described in Sec. 2.2. Both phase noises have equal variance $\sigma_\phi^2(\tau) = \pi \times 10^{-4} \text{ rad}^2$ at 10 GS/s ($\tau = 100\text{ps}$). The SNR was set to 13 dB and each data point was calculated over 10^5 samples. As shown in the figure, $\text{var}[e_{\hat{\phi},pn}](N)$ increases linearly with N for ideal Lorentzian noise; but increases super-linearly for the non-white FM noise. Note that the second term on the right-hand side of Eq. (2.9) is equivalent to a non-weighted moving-average filter applied to the phase sequence $\phi(k)$, known to have a linear relation between the estimate error variance and filter length when $\Delta\phi(k) = \phi(k) - \phi(k-1)$ has a white Gaussian distribution [94].

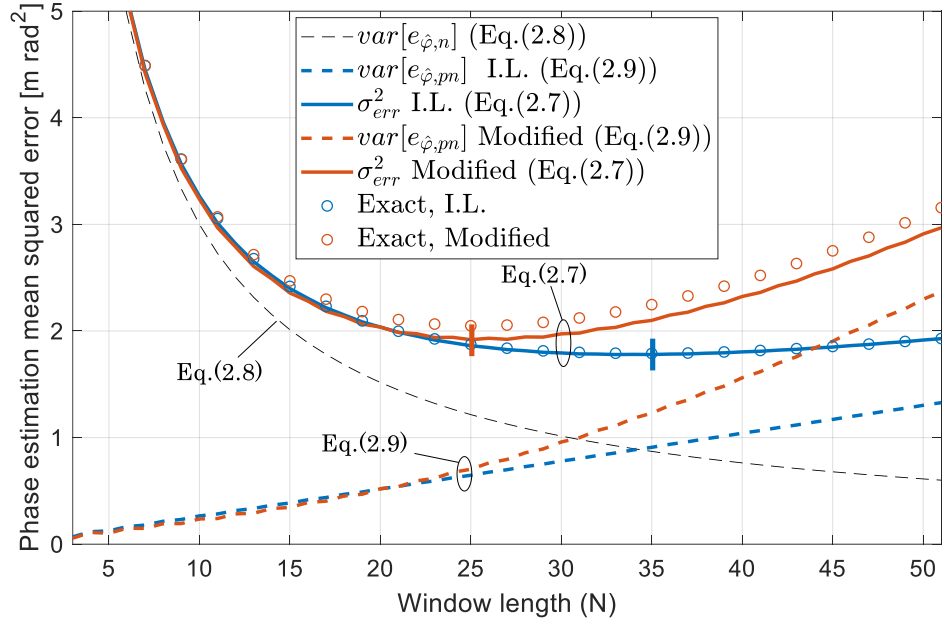


Fig. 2.8. Phase estimation mean squared error components for Eqns. (2.7-2.9) evaluated over 10^5 samples for different window lengths. Vertical bars indicate points of minima on corresponding curves. I.L.: Ideal Lorentzian.

The moving-average filter has low-pass characteristics with a cut-off frequency inversely proportional to the filter (window) length. This emphasizes the impact of low-frequency noise portion of $S_{FM}(f)$. As the sum of two contributions, the total mean square error σ_{err}^2 in Eq. (2.7) has window length-dependent minima, which are demarked by vertical bars in Fig. 2.8. Each

minimum identifies an optimum window length, which can be different for different combinations of modulation format, phase noise variance and spectral profile, and SNR . We observe this optimum window length contracts (from 35 to 25) for the spectrally modified phase noise due to its non-white spectral profile. The circled markers show the results of the exact values of $\sigma_{err}^2(N)$ obtained after modulating random QPSK symbols with the same phase noise sequences and SNR value and comparing the estimated phase noise from the M th-power CPR, by means of Eq. (2.6), to the original phase noise. They show that Eq. (2.7) gives very accurate results for the ideal Lorentzian case and fairly close values for the non-white FM noise case. Note that for either case the value of N at which the minimum σ_{err}^2 occurs coincides with the prediction of Eq. (2.7), which shows the accuracy of the approximation made in this analysis. This result explains the reason why the optimized window lengths are shorter for the non-white FM noise of MLLs shown in Fig. 2.5 (and Fig. 2.6) for both CPR algorithms, compared to the ideal Lorentzian phase noise of similar LELs. For the case of non-white FM noise, the phase estimation error is more sensitive to the variation of window length, and the minimum estimation error at the optimum window length is also slightly higher than that obtained with the white FM noise. This will be further discussed in the next section.

Following the analysis of optimum averaging window length, the results are confirmed by BER simulations using the measured phase noise of the 25G-MLL. Differentially encoded 16-QAM symbols were modulated on the phase sequences decimated at 10 GS/s to simulate a 10 GBd system. Both M th-power and BPS based algorithms were used to obtain system penalties at $BER = 10^{-3}$ for the ideal Lorentzian phase noise and the phase noise measured from the MLL at different averaging window lengths. As shown in Fig. 2.9(a) & (b), the predictions obtained from the analysis above are confirmed for different CPR algorithms. The optimum window shifts to a

smaller size for non-white $S_{FM}(f)$ as was predicted from Fig. 2.8. The increased sensitivity of system penalty to the choice of window length for non-white FM noise indicates that the CPR optimization in system design may be based on measured phase noise sequences rather than an ideal Lorentzian model.

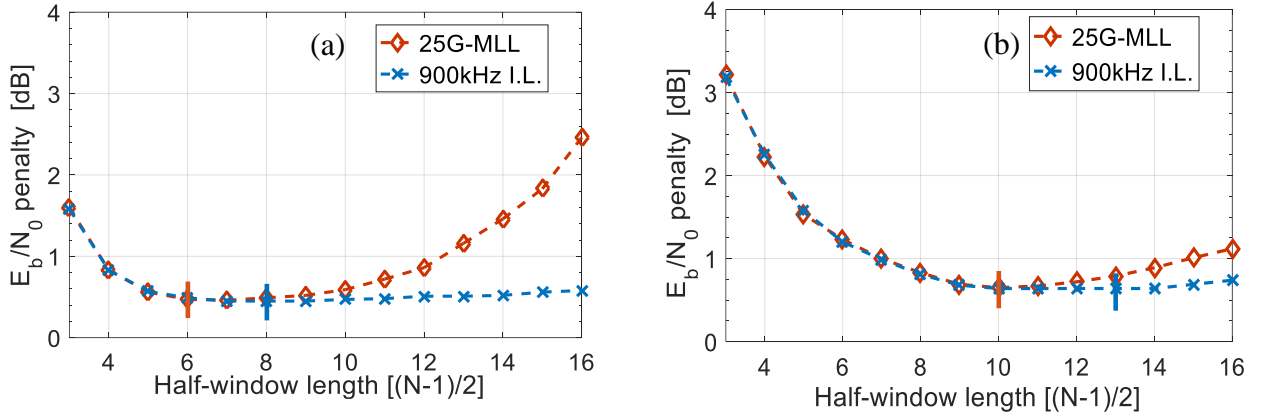


Fig. 2.9. E_b/N_0 penalty at $\text{BER}=10^{-3}$ for 10 GBd differential 16-QAM for (a) BPS and (b) M th-power CPR. Penalties are calculated with reference to the ideal case in the absence of phase noise. Vertical bars indicate points of minima.

2.4.2 Phase Estimation Efficiency and Performance Prediction Accuracy

For the case of non-white FM noise, the minimum σ_{err}^2 at the optimum window length is higher than that of white FM noise as shown in Fig. 2.8. This can be regarded as a reduced efficiency of phase estimation, which introduces additional system SNR penalty. Note that this increase of penalty was not clear in the results shown in Fig. 2.9(a) & (b), which we attribute to a slight overestimation of the LEL due to the instrumentation noise. In this section, the efficiency of phase estimation is studied for different $S_{FM}(f)$ profiles and CPR algorithms, and the related residual SNR penalty is quantified. CPR estimation efficiency can be measured by the ratio between the mean squared error σ_{err}^2 and the theoretical minimum achievable error expressed by the Cramér-Rao lower bound ($CRLB$) [95]. For square QAM signals with practical SNR values, $CRLB=1/(2N \cdot SNR)$ [96]. The phase estimation efficiency can thus be expressed as

$$\eta(N) \equiv \frac{CRLB(N)}{\sigma_{err}^2(N)} = \frac{(2N \cdot SNR)^{-1} * 100}{var[\varphi(k) - \hat{\varphi}(k, N)]} \leq 100\% \quad (2.10)$$

where SNR is the ratio between the average symbol energy and the power spectral density of additive noise, that is $E_s/N_0 = \log_2(M) \cdot E_b/N_0$.

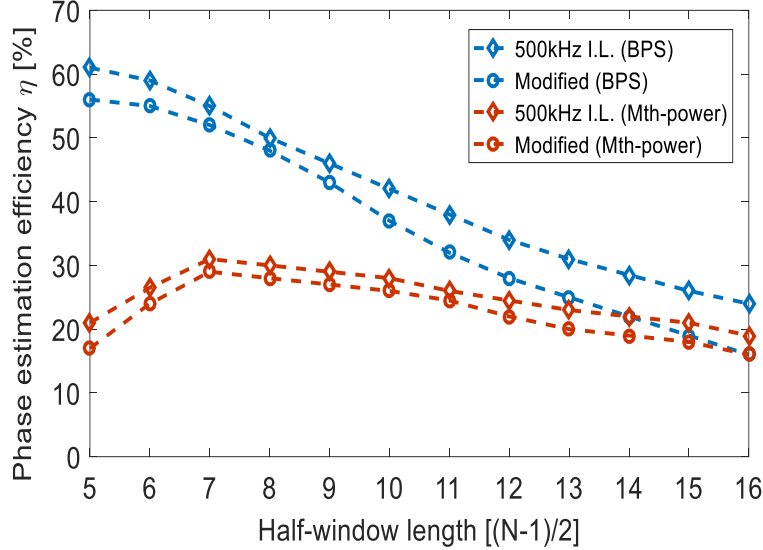


Fig. 2.10. Phase estimation efficiency η versus averaging window half-length for the BPS and the M th-power CPR for a 16-QAM signal at 10 GBd with $SNR=17$ dB.

Figure 2.10 shows the calculated phase estimation efficiency versus half-window length for an ideal Lorentzian phase noise with 500 kHz linewidth and a non-white phase noise for both the M th-power and the BPS CPR algorithms. The non-white noise was generated with spectral modification as shown in Fig. 2.1(a) with parameters $\{F_l, G\}=\{50 \text{ MHz}, 10\}$, and slope = -10 dB/decade. Both the white and the non-white phase noises have the same phase difference variance $\sigma_\varphi^2(\tau) = \pi \times 10^{-4} \text{ rad}^2$ sampled at 10 GS/s ($\tau = 100$ ps). The optical field with phase noise was loaded with 16-QAM symbols, and the SNR was set to 17 dB through noise loading. In comparison to the M th-power CPR, BPS algorithm has better phase estimation efficiency, especially for short averaging windows. The phase estimation efficiency is lower for the laser with non-white FM noise compared to that with white FM noise for both CPR algorithms, and this difference is more

pronounced for the BPS at long window lengths. This agrees with the fast increase of SNR penalty with the window length shown in Fig. 2.9(a) for the non-white FM noise sequences of the 25G-MLL.

Note that although system penalty due to phase noise is closely related to phase estimation efficiency, it cannot be assessed solely by this efficiency. This is because BER is also affected by the probability of cycle slips which are not included in the calculation of phase estimation efficiency, as have been removed before calculating the estimation error in the denominator of Eq. (2.10). The probability of cycle slip events can vary for different profiles of $S_{FM}(f)$. Therefore, for the case of non-white FM noise, it is more accurate to investigate the phase-noise-induced SNR penalty directly from the BER calculation after CPR.

To investigate the impact of non-white FM noise on SNR penalty without the ambiguity of laser characterization errors, we run a computer simulation using digitally generated phase noise sequences with increased low-frequency components in $S_{FM}(f)$ as described in Sec. 2.2. Ideal Lorentzian phase noise was first generated with a linewidth of 500 kHz or 1 MHz. Spectral modification was then applied to generate the non-white FM noise with $G = 10$ and 20. The parameter F_l was swept from 0 to 300 MHz in 20 equal steps on the logarithmic frequency scale, representing different bandwidths of low-frequency excess FM noise. The phase difference variance $\sigma_\phi^2(\tau)$ of the spectrally-modified non-white FM noise is then rescaled to its original value before spectral modification [$\sigma_\phi^2(100\text{ ps}) = 2\pi \times 10^{-4}$ or $\pi \times 10^{-4} \text{ rad}^2$ at 10 GS/s]. This assures that all phase noise sequences with different spectral profiles have the same LEL at $\tau = 100$ ps, although they may have very different FWHM linewidths. The results of this simulation will also show the accuracy of using LEL sampled at the signal symbol rate in predicting system performance, regardless of the actual FWHM linewidth of the laser and measurement-induced errors.

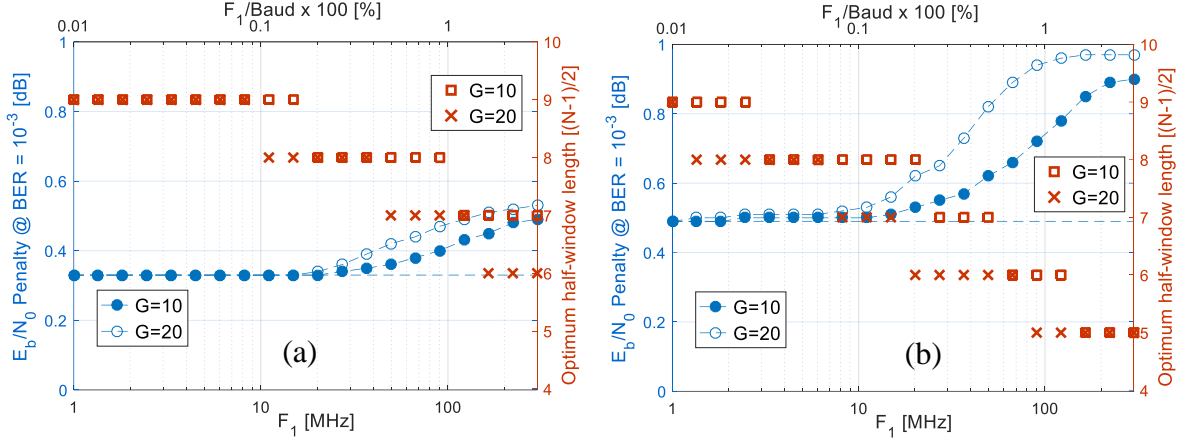


Fig. 2.11. SNR penalty and optimum window length versus F_l for differential 16-QAM at 10 GBd with BPS algorithm and initial ideal Lorentzian laser linewidth of (a) 500 kHz and (b) 1 MHz.

Figures 2.11(a) and (b) show the E_b/N_0 penalty (for $\text{BER} = 10^{-3}$) as the function of F_l for the LELs of 1 MHz and 500 kHz, respectively. 16-QAM differential encoding is used to generate the 10 GBd signal with 5 million data symbols simulated at each point. BPS is employed for CPR with $B = 64$ [4]. The optimum window length (indicated by the right y-axes in the figures) was optimized for each value of F_l . The penalty was calculated with reference to the ideal case without phase noise and was found to be 0.33 dB and 0.49 dB for the ideal Lorentzian phase noise without spectral modification, for the linewidths of 500 kHz and 1 MHz, respectively (see horizontal dashed lines in the figures). With the increased low frequency components of $S_{FM}(f)$ through spectral modification, the penalty starts to increase when the frequency F_l reaches to a few 10s of MHz ($\sim 0.1\%$ of symbol rate), and the optimum window length is reduced accordingly with the increase of F_l . For the case shown in Fig. 2.11(a), the spectral modification increases the FWHM linewidths from 500kHz to 4 MHz and 6 MHz, with $F_l = 100$ MHz and $G = 10$ and 20, respectively, but the system penalty is only increased by less than 0.2 dB. Given that $\sigma_\phi^2(\tau)$ is kept constant (sampled at the system symbol rate), so as the LEL, this 0.2 dB discrepancy represents the inaccuracy of using LEL to estimate system SNR penalty. Similarly, for Fig. 2.11(b) the FWHM

linewidth is increased from 1 MHz to 6 MHz and 8 MHz for $F_l = 100$ MHz and $G = 10$ and 20, respectively. The highest discrepancy of system SNR penalty evaluated based on the LEL system is less than 0.45 dB even with a relatively high F_l of 300 MHz (3% of symbol rate) and an enhancement factor G of 20. This discrepancy is much less than what would be expected based on the FWHM linewidth (e.g., >4 dB for FWHM of 9 MHz, see Fig. 2.5(a) & (b)), indicating that LEL is a much more accurate parameter to specify the system impact of lasers with non-white FM noise.

2.5 Conclusion

We have measured phase noise and spectral linewidths of different laser diodes and found that FM noise spectral profiles of these lasers are not always white and can have significant variations at different frequencies for some types of lasers. Excess low-frequency FM noise components may extend up to tens of MHz in some types of lasers, like the QD-MLLs, with more than an order of magnitude ratio compared to higher frequencies. This non-white characteristic of FM noise is found to affect the use of spectral linewidth when estimating the performance of optical systems that require CPR. Based on measured optical phase noise waveforms of different types of lasers, we have shown that the spectral FWHM linewidth alone is not sufficient to characterize phase noise, or to determine its impact on the design of an optimum CPR for coherent receivers for non-white FM noise. Using the measured phase noise from different QD-MLLs with several MHz FWHM linewidths, we have shown by simulation comparable system performance to a DFB laser of only a few hundred kHz FWHM linewidth, due to dissimilarity in their FM noise spectral profiles. This result was further supported by a B2B 16-QAM transmission experiment comparing a QD-MLL with an ECL at a low symbol rate of 5 GBd. The OSNR penalty was found to be only ~0.7 dB when replacing the ECL (<50 kHz FWHM linewidth) with the QD-MLL (>8 MHz

FWHM linewidth) in the experiment, with optimizing the CPR averaging window size. We have also shown that a “Lorentzian-equivalent linewidth”, evaluated by sampling the phase noise waveform at a relatively high sampling frequency, can be a reliable and accurate parameter for assessing the impact of laser phase noise in the digital coherent system. The choice of a practical sampling frequency may depend on the characteristics of the phase noise and the SNR in measurement setup. However, we have shown that for a wide practical range of non-white FM noise profiles a sampling frequency at 5 GHz is adequate. Furthermore, by semi-analytical analysis and supporting results from the experimental measurements, the optimum averaging window length in CPR algorithms was shown to be shorter for non-white phase noise with enhanced low-frequency phase noise power spectral density at fixed phase difference variance. This observation suggests that CPR algorithms should be optimized in system design stage based on the actual phase noise data of the laser rather than relying on the ideal Lorentzian model.

Chapter 3

Phase Noises in Quantum-Dot Mode-Locked Multi-Wavelength Light Sources

Quantum-dot(dash) mode-locked lasers (QD-MLLs) are multi-wavelength light sources that can generate multiple optical carriers by a simple DC bias electrical current injection. This chapter provides a detailed study of the phase noises of individual comb lines and the *differential phase noise* (DPN) between adjacent comb lines in QD-MLLs. The conclusions from the investigations presented in Chapter 1 are used as a foundation for the studies presented here. First, we study phase-noise spectral properties of comb lines from a QD-MLL and show that their large linewidth variability attributes to the low-frequency phase variations. Semi-numerical and experimental simulations show that these variations have minimal effect on coherent system performance at practical symbol rates. Second, we show that the DPN between adjacent comb lines in QD-MLLs may exhibit higher phase noise impacts in (self-)coherent transmission systems than their apparent narrow linewidths, due to unique spectral profiles. Finally, we present a coherent multi-heterodyne technique used to instantaneously measure multiple comb lines from a QD-MLL. This technique enables the measurement of inter- and intra-line phase noises of any comb source by a single measurement, which also enables the measurement of temporal properties of the optical signal when the comb source is considered as an optical pulse train generator.

3.1 Introduction

Optical datacenter interconnects (DCIs) are expected to provide >400 Gb/s data rate capabilities in the foreseeable future, driven by the continuing growth of internet applications and centralized cloud services. At these throughputs, coherent solutions can rival and best IMDD by measure of density, power per bit and reach [97-99]. Coherent transmission can also improve system reach and spectral efficiency for applications with relatively lower symbol rates, such as passive optical networks (PONs) and mobile network backhaul systems [100,101]. QD-MLLs are attractive multi-wavelength light sources by virtue of their small footprint, energy efficiency, and integrability in photonic integrated circuits (PICs) [78,102,103]. QD-MLLs can simultaneously generate tens of CW signals (or *comb lines*) equally spaced by a specified repetition frequency over a wavelength window of typically ~ 10 nm [78,102-104]. The demonstration of these devices with desired line spacing on the order of tens of GHz shows that they are suitable for WDM applications. Therefore, detailed understanding of the phase noises in these sources is of high importance. In general, these devices can suffer from relatively high phase noise exhibited by individual comb lines compared to high-quality DFB lasers and ECLs commonly used in coherent communication applications [77,78,104]. It has been shown that the linewidths of comb lines of a QD-MLL vary with the wavelength parabolically [78,102,104]. However, these studies quantified the phase noise only by means of the FWHM linewidths of individual lines, without investigating the properties of their phase noises. In this chapter, Sec. 3.2 we will study the spectral properties of the phase noise of ~ 40 individual comb lines across the emission window of a QD-MLL with 25 GHz line spacing. Section 3.3 will study the DPN between adjacent comb lines and show its impact in self-coherent applications. Finally, Sec. 3.4 will present the coherent multi-heterodyne technique used to characterize phase noises in a QD-MLL with 11 GHz line spacing.

3.2 Phase Noise Spectral Properties Across Individual Comb Lines in Quantum-Dot Mode-Locked Lasers

In this section we study the FM noise spectral profiles of different comb lines across the emission window and show that the variation of linewidths as the function of wavelength is mainly caused by the variation of low-frequency components of the FM noise of these spectral lines. Although the linewidth varies by $>500\%$ across the emission band, we show that the system performance using these spectral lines as light sources only change slightly. We also show that with proper device biasing, and careful receiver CPR design, all comb lines of a QD-MLL can be used for coherent transmission, even at relatively low symbol rates. This is due to the relatively low FM noise components at the high frequency for all comb lines. This avoids the need for linewidth reduction techniques such as feed-forward [105] or feedback injection locking [106].

3.2.1 Experimental Procedure and Device Characterization

The QD-MLL used in our experiment is a single section InAs/InP operating in the lower half of the C-band from 1531 to 1541 nm with 25 GHz comb line spacing. Figure 3.1(a) shows the optical spectrum of the device with two different bias current and device temperature combinations chosen to align the same comb lines to the 25-GHz ITU-T Grid. The spectra were obtained by an optical spectrum analyzer (OSA) with a resolution bandwidth (RBW) of 0.01 nm. To characterize spectral properties of individual comb lines, we used a 25:50 GHz interleaver followed by a tunable bandpass filter and an EDFA to select and amplify individual comb lines. The experimental setup used here is similar to that shown in Fig. 2.3 in Chapter 2. An integrated phase-diversity coherent receiver with a tunable ECL (linewidth <30 kHz) as the LO was employed to downshift the selected comb line to the RF domain. The I and Q components of the RF signal were captured at 50 GS/s by a real-time oscilloscope with an electrical bandwidth of 23 GHz and a nominal vertical

resolution of 10 bits. The temperature sensitivity of QD-MLL comb line wavelength was found to be $\sim 0.1 \text{ nm}/^\circ\text{C}$. We chose four cases of the set temperature from 16°C to 22°C in a step of 2°C (0.2 nm wavelength change) to align the comb to the 25-GHz grid. At the same time, the bias current was reduced in every step to re-align the same comb line back to the same original wavelength (see the legend of Fig. 3.1(b)). On the other hand, the required current change ranges from 55mA to 85mA (depending on the temperature) to create a 0.2-nm wavelength change. Change of frequency spacing between comb lines due to temperature and current change was not observed for the given range of measurements.

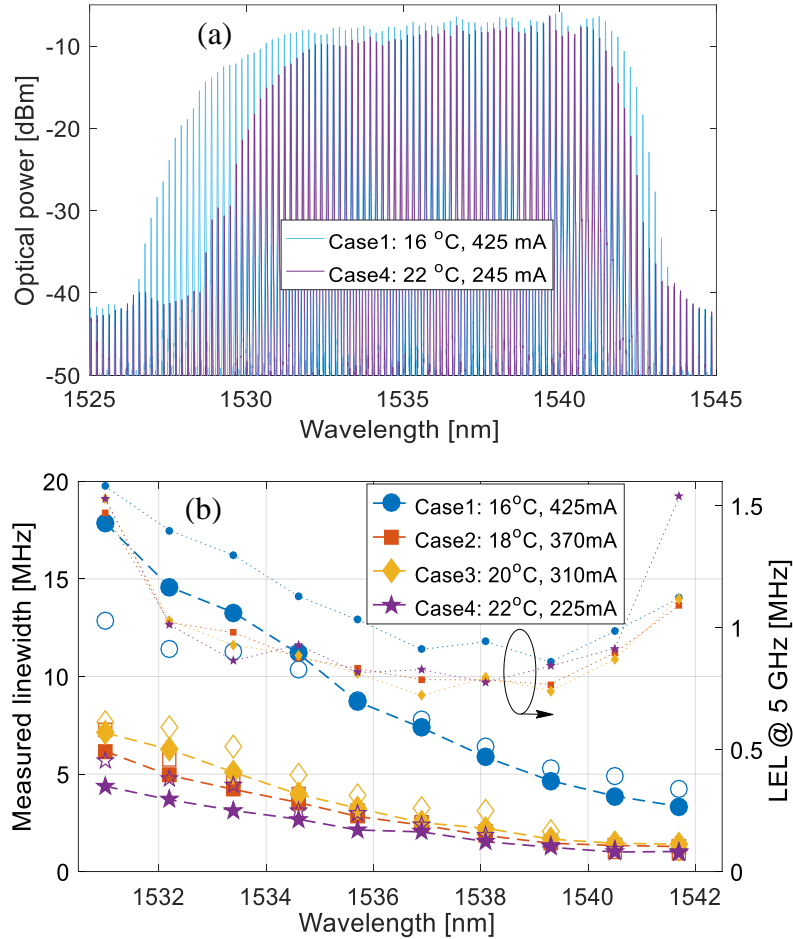


Fig. 3.1. (a) Optical spectra of the QD-MLL (RBW=0.01nm) for two different bias and temperature cases, and (b) measured linewidths of 10 different comb lines. Filled markers: statistical linewidths; open markers: spectral linewidths; smaller markers: LELs.

We characterize the linewidth of individual lines by two different measures: (1) a *statistical* linewidth calculated from the phase difference variance, $\sigma_\phi^2(\tau) = \text{var}[\phi(t) - \phi(t - \tau)]$, at $\tau = 10$ ns, where the linewidth is obtained as $\Delta\nu = \sigma_\phi^2/(2\pi\tau)$ [64]; and (2) a *spectral* linewidth calculated from the normalized field spectrum at -20 dB and converted to the -3dB linewidth, assuming a Lorentzian shape, as $\Delta\nu_{-3dB} = \Delta\nu_{-20dB}/\sqrt{99}$. Figure 3.1(b) shows the calculated linewidths for 10 comb lines for each of the 4 bias cases covering the 6-dB emission window of Case 4. Each point in the figure shows an average of three different measurements, each of 1 million samples (20 μ s duration). Unlike the case for most single-mode semiconductor lasers, we find that the QD-MLL does not show monotonic decrease of linewidths when increasing the current or decreasing the temperature. Instead, for all cases, the spectral widths of comb lines have similar dependence on the wavelength. Also shown in Fig. 3.1(b) are the Lorentzian-equivalent linewidths (LELs) for the corresponding measurements, with the small size markers. LELs are equivalent to the statistical linewidths calculated at a specific sampling frequency ($1/\tau$); 5 GHz was used here. As was shown in Chapter 1, for lasers with non-white FM noise, LELs at high frequencies are better indicators of the laser performance in coherent systems than the actual spectral linewidths. The measured statistical and spectral linewidths show comparable values for all measurements except for the short wavelength region of Case 1. Fig. 3.1(b) also indicates that the measured linewidths can change significantly over the wavelength. For example, Case 2 shows a change of statistic linewidth from 1.5 MHz to 4.8 MHz (220% variation) for the comb lines at 1532.29 and 1539.37 nm. However, the corresponding LELs at 5 GHz show a much smaller variation from 0.75 MHz to 1 MHz (33% variation) across the entire wavelength window of between these comb lines. Figure 3.2(a) displays the FM-noise PSDs of four equally-spaced wavelengths across the 3-dB optical bandwidth of the comb at Case 2.

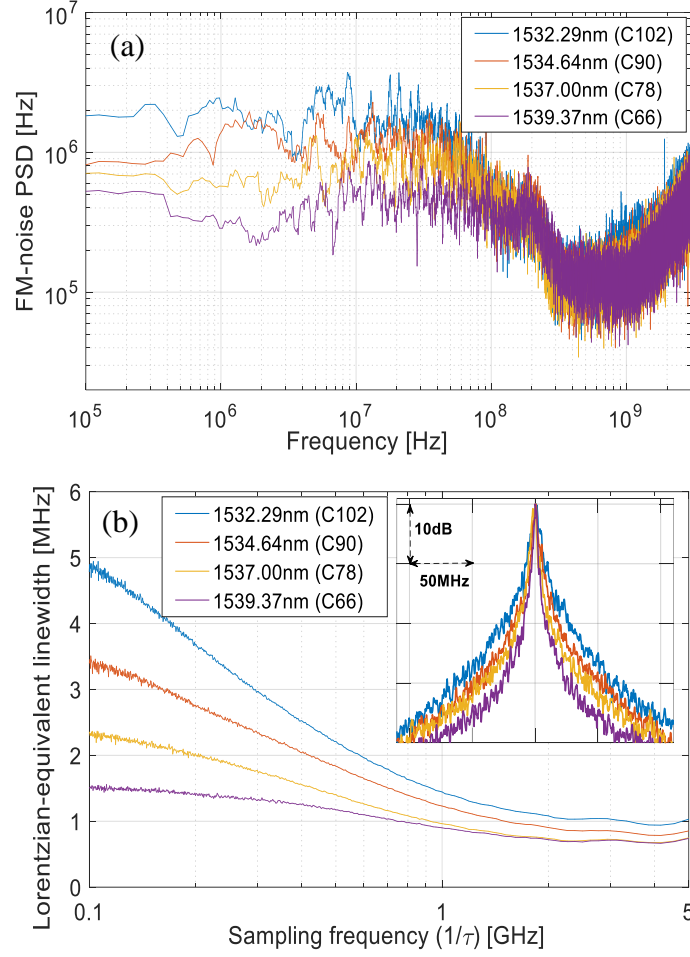


Fig. 3.2. (a) FM-noise PSD of four different comb lines at Case 2 (18°C, 370mA), and (b) corresponding LELs vs. frequency. Cxxx indicate the channel number according to the 25-GHz

Although the FM noise spectral contents in the low frequency region around 10 MHz vary by ~ 7 dB, FM noise at high frequencies above 100 MHz show only very small variations. Figure 3.2(b) shows the corresponding LELs evaluated at different sampling frequencies. In this figure, measured LEL values at 100 MHz and at 5 GHz correspond to the statistical linewidths and the LEL values shown in Fig. 3.1(b) (Case 2), respectively, for the same set of comb lines. The inset shows the corresponding measured field spectra. It can be noticed that the LELs at 100 MHz (representing the spectral linewidths) have a larger variation ($\sim 220\%$) than that of the LELs at 5 GHz ($\sim 33\%$), analogous to the trend found in Fig. 3.2(a) for the FM-noise PSDs, as a function of frequency. Since the impact in a coherent system depends mainly on the high-frequency

components of the FM noise comparable to the symbol rate, all comb lines across the emission band are expected to exhibit comparable performances, with much smaller variation than suggested by their spectral linewidths, as will be shown next.

3.2.2 Performance in Digital Coherent Systems

To investigate and compare the performance in coherent transmission, two different comb lines, at 1532.29 nm and 1540.16 nm, were used as the Tx light sources with statistical linewidths of 4.8 MHz and 1.45 MHz and LELs of 1 MHz and 0.73 MHz, respectively. The QD-MLL bias conditions were set as in Case 2. Figure 3.3 shows the schematic of the experimental setup. Comb line selection and coherent receiver used in the system experiments were the same as those described above, except that the signal was I/Q modulated, and extra optical noise was loaded before the coherent receiver to change the OSNR. The 16-QAM signal was differentially pre-coded and Nyquist pulse-shaped with a roll-off factor of 0.1. The I and Q components from the coherent receiver were captured at 25 GS/s and processed offline with the basic coherent receiver DSP stages comprising resampling, frequency compensation, matched filtering, symbol timing, equalization, CPR, and hard-decision symbol-to-bit de-mapping. A single-stage blind phase search was used for CPR with 64 test phase points, and the optimum half-window length of 6 was used [4].

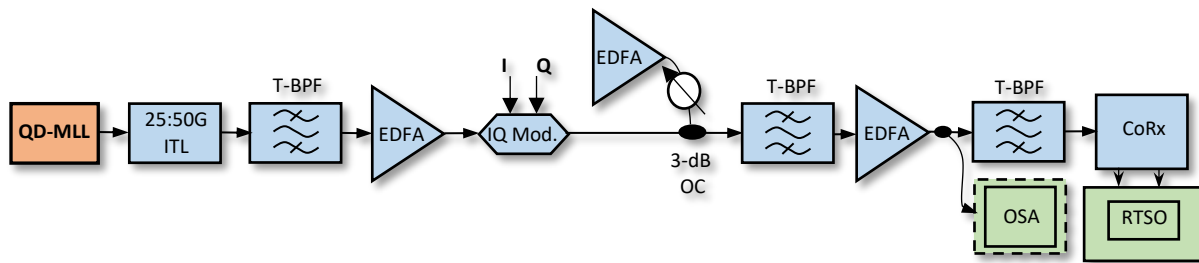


Fig. 3.3. Schematic of the B2B coherent transmission experimental setup.

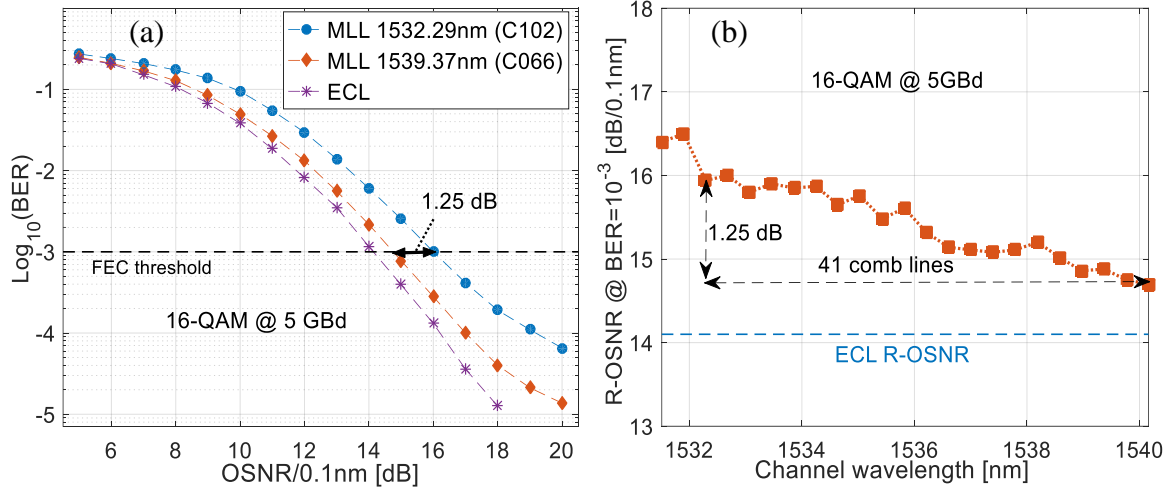


Fig. 3.4. (a) Experimental BER vs. OSNR, and (b) experimental R-OSNR at 10^{-3} BER.

Figure 3.4(a) shows the measured OSNR performance of a coherent system with single-polarization 16-QAM modulation at 5 GBd. The required OSNRs (R-OSNR) to achieve the conventional FEC BER threshold of 10^{-3} were 15.95 dB and 14.7 dB for the 1532.29 nm and the 1540.16 nm comb lines, respectively, with a difference of only 1.25 dB. An ECL was also used as the Tx light source for comparison, which shows a R-OSNR of 14.1 dB at the same BER threshold. We then measured the R-OSNR of every other comb line across the 8.2-nm emission band. The I/Q modulator control and the optical input power to the coherent receiver were monitored throughout the experiment to avoid any wavelength-dependent performance dissimilarities in the setup. The results in Fig. 3.4(b) show that the R-OSNR varies only by 1.25dB across the wavelength window, which is much smaller than one would expect from the large linewidth variation of these comb lines.

With increasing the symbol rate, the sensitivity of performance to low-frequency FM noise is expected to drop. To observe this, we used measured waveforms of the complex envelopes of unmodulated comb lines, to simulate the system performance at different symbol rates [64] for the captured comb lines shown as in Fig. 3.2. The simulation setup is shown in Fig. 3.5.

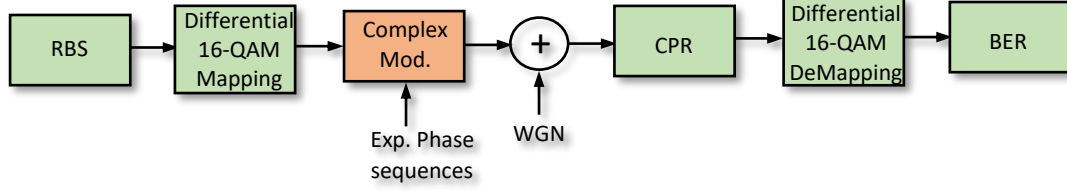


Fig. 3.5. Simulation setup used to measure the performance at different symbol rates from the measured phase noise waveforms.

In the simulation, the 16-QAM data symbols were carried by the experimental complex waveforms of the comb lines, and white Gaussian noise (WGN) was added to change the per-bit signal to noise ratio (E_b/N_0) before BPS CPR (no. of test points $B=64$) and demodulation. Optimum averaging window length was used for each case. Figure 3.6 shows the required E_b/N_0 to achieve a threshold BER of 10^{-3} . At 5 GBd, the penalty difference between the comb lines of shortest and longest wavelengths is 1.14 dB of ROSNR, which agrees reasonably well with the experimental results (the 1.25 dB for the R-OSNR difference between these lines). The required E_b/N_0 difference reduces drastically with increasing the symbol rate. Negligible performance difference is observed when using all these comb lines at 10 GBd symbol rate and above. For comparison, the unfilled markers represent the case where computer-generated white phase noise is used for each comb line, in which the white FM noise was generated as a Weiner process with Lorentzian linewidths equal to the measured statistical linewidth and LEL (gray and colored unfilled markers, respectively) for each comb line of the QD-MLL. The results of the statistical linewidths show a much bigger variation of SNR performance compared to the phase noise from the QD-MLL, at all symbol rates; whereas the results of the LELs show reasonably accurate predictions at both 10 and 16.67 GBd rates. This indicates that measured statistical and spectral linewidths of the comb lines from a QD-MLL, with their high variability, are not reliable indicators in assessing the impact of phase noise of these light sources in coherent transmission. Instead, LELs show very accurate

predictions and could be used to predict the phase noise impact of these lasers at practical symbol rates when compared to lasers with white FM noise profiles such as DFB lasers.

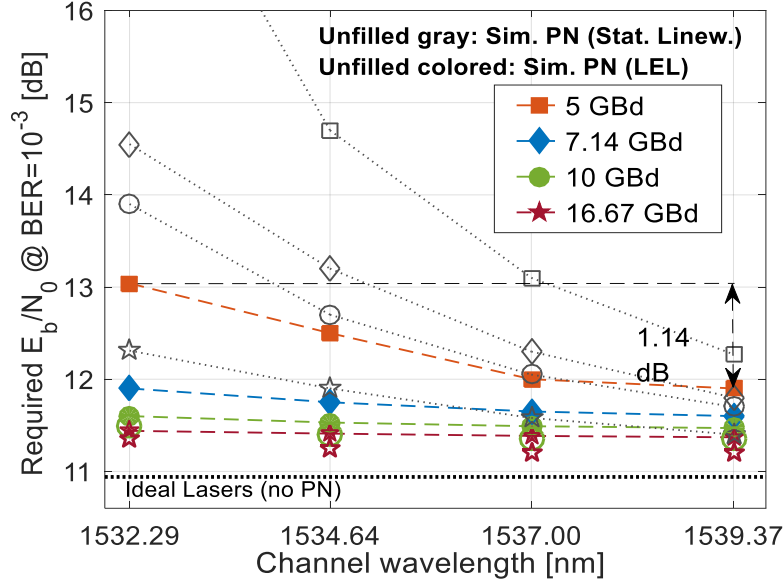


Fig. 3.6. Semi-numerical simulations of required E_b/N_0 for differential 16-QAM at different system baud. Sim. PN: simulated phase noise.

3.3 Differential Phase Noise Properties in QD-MLL and its Performance in Coherent Transmission Systems

While the phase noise from individual comb lines has linewidths of a few MHz, the DPN between adjacent spectral lines is much lower, with a linewidth on the order of kHz [107]. This is attributed to the mutual coherence between adjacent spectral lines, which is an attractive property of DQ-MLLs, which can be utilized in self-coherent systems. For example, an unmodulated adjacent spectral line can be used as the LO to perform heterodyne detection at a self-coherent receiver, as will be shown in Chapter 4, where the DPN will become the effective phase noise source.

In this section we show that DPN in a QD-MLL exhibits a contrary property to that of individual lines, hereinafter referred to as the common-mode phase noise (CMPN) to discriminate it from the DPN. Although the apparent linewidth of DPN is quite narrow, its impact in the system performance can be substantial due to the relatively strong high frequency components of FM-

noise PSD. We show that DPN affects system performance more than what is estimated by the FWHM linewidths.

3.3.1 Experimental Procedure and DPN Characterization

Two single-section InAs/InP QD-MLLs with 11 GHz and 25 GHz repetition frequencies are used in our experiment, hereinafter referred to as 11GHz-MLL and 25GHz-MLL, respectively. Both lasers operate in the C-band with an approximately 10 nm spectral bandwidth, with about 110 and 50 total spectral lines, respectively. The lasers were biased at 430 mA for the 11GHz-MLL and 350 mA for the 25GHz-MLL, at room temperature. A phase-diversity coherent receiver was used to down-convert the optical fields to the electrical domain with the exact setup shown in Fig. 2.3 in Chapter 2. An external cavity laser (ECL) with <50 kHz linewidth was used as the LO. A 1nm bandwidth tunable optical filter was used to select several spectral lines from the QD-MLLs, followed by a polarization controller to maximize the mixing efficiency with the LO. A real-time sampling oscilloscope operating at 50 GS/s (23 GHz analog bandwidth) was used to capture the I and Q components of the down-converted complex optical field. A second ECL, also with <50 kHz linewidth, was used for comparison. Multiple data sets, each with 10^7 sample points (0.2ms in period), were recorded from each laser for characterization and performance assessment through computer processing.

In offline processing, the coherently detected complex optical fields were frequency-shifted and bandlimited to select individual comb lines. The unwrapped phase noise sequences $\varphi(n)$, where n is the sample index, from each line were then obtained. The DPN between two adjacent lines, $\delta\varphi(n)$, from each QD-MLL were obtained by mixing one line with the complex conjugate of its neighbor. Figure 3.7(a) shows the FM-noise PSD, $S_{FM}(f)$, of the CMPN from the 11GHz-MLL, the DPN for both MLLs, and the beat tone of the two ECLs for comparison. It is

evident that the CMPN exhibits strong low frequency components extending up to ~100-MHz, as was shown in the previous section and Chapter 2. In contrast, the FM-noise PSDs of DPN are 3 orders of magnitude lower than that of CMPN at the low frequency region; but they exhibit relatively strong high frequency components for both QD-MLLs. In comparison, the ECL has a relatively flat FM-noise PSD profile. The narrow $\Delta\nu$ of DPN is predominately determined by the low frequency components of FM-noise.

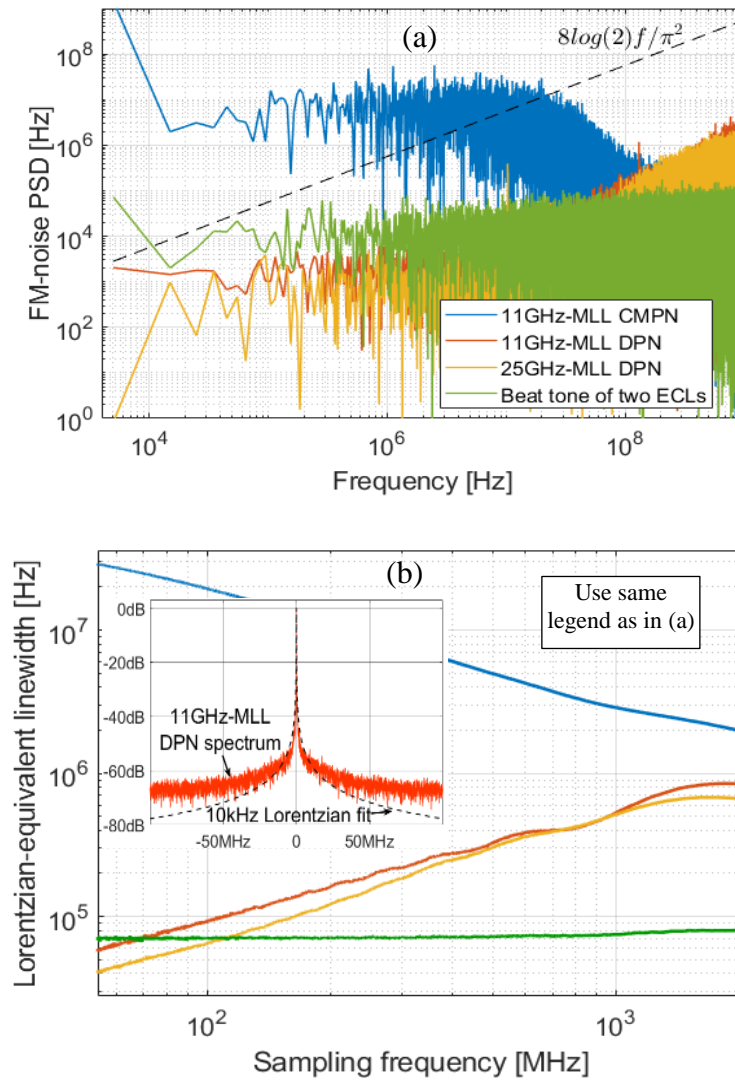


Fig. 3.7. (a) FM-noise PSD profiles of DPN compared to CMPN and ECLs; and (b) Lorentzian-equivalent linewidths at different sampling frequencies.

Figure 3.7(b) shows the LELs of these phase noise profiles at different sampling frequencies. The CMPN and DPN exhibit contrasting trends with changing the sampling frequency, due to their different $S_{FM}(f)$ profiles. Actual FWHM linewidths $\Delta\nu$ are comparable to the LELs at lowest sampling frequencies. The inset in Fig. 3.7(b) shows the spectrum of the 11GHz-MLL DPN with a Lorentzian fitting of 10kHz FWHM linewidth; however, the actual PSD is higher at high frequencies due to the high frequency components of $S_{FM}(f)$.

3.3.2 Performance of DPN in Digital CPR

To assess the impact of DPN in coherent systems employing digital CPR algorithms, the DPN sequences were resampled at the signal baud rate and used as the combined Tx-Rx laser phase noise. The simulation setup is similar to that used in Fig. 3.5. Differentially-mapped 16-QAM and 64-QAM symbols were encoded on the measured optical phases of the 11GHz-MLL and ECL beat tone of Fig 3.7(a) at 5 and 10 GBd, respectively. The E_b/N_0 was varied by loading additive white Gaussian noise to the signal before CPR and symbol-to-bit de-mapping. Perfect frequency offset compensation with ideal symbol synchronization is assumed, so that laser phase noise is the only effect to investigate. The M th-power [70] and the single-stage blind phase search [4] algorithms were used for CPR of the 16-QAM and the 64-QAM signals, respectively.

Figure 3.8 shows the BER versus E_b/N_0 using the 11GHz-MLL. BER curves without phase noise and using ECLs as the light sources are also shown for comparison. Despite the narrow linewidth of DPN (~ 10 kHz) it results in higher penalty compared to the ECLs with higher combined Tx-Rx linewidth (~ 80 kHz).

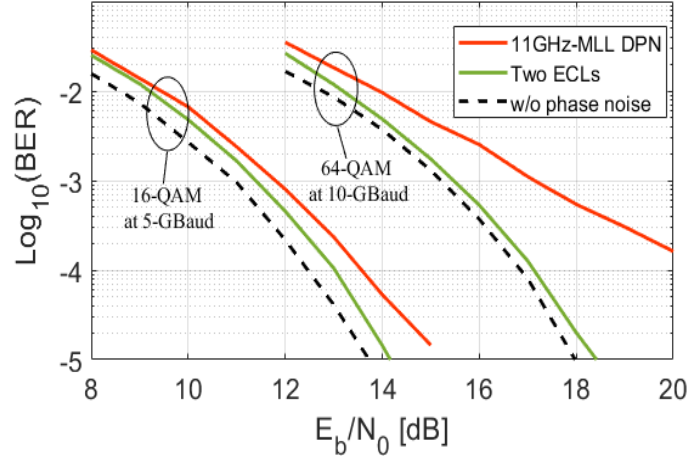


Fig. 3.8. BER vs. E_b/N_0 for the 11GHz-MLL DPN and ECLs with 16-QAM at 5 GBd and 64-QAM at 10 GBd.

In conclusion, we have shown that the differential phase noise in QD-MLLs exhibits high FM-noise PSD components at high frequencies; thus, imposing stronger impact on coherent system performance than what would be estimated by the relatively narrow spectral linewidths. However, it will be shown in the next chapter that the DPN from QD-MLL has practically low phase noise compared to the differential phase noise between two independent single-mode lasers, like the DFB lasers. Therefore, the QD-MLLs can be utilized in generating multiple channels in SSB self-coherent applications.

3.4 Coherent Multi-Heterodyne for Phase Noise Characterization of Frequency Comb Sources

Common-mode and differential-mode phase noises have been characterized and analyzed for various types of mode-locked lasers. Passively mode-locked fiber lasers and diode-pumped solid state lasers such as Ti:Sapphire and Nd:YAG lasers usually have repetition rates lower than 100 MHz, allowing a large number of discrete optical spectral lines to be mixed and measured within the electrical bandwidth of a wideband photodiode and RF spectrum analyzer. In this way relative phase variations and mutual coherence between different spectral lines have been measured

[108,109]. Passively mode-locked diode lasers based on quantum-dash or quantum dot (QD) semiconductor materials have also been characterized [110]. Because of the short optical cavity length, the repetition rate of such a laser is typically a few to tens of GHz. While this is desirable as a channel spacing in WDM applications, it makes characterization based on the same technique as diode-pumped solid-state lasers difficult as the required electrical bandwidth beggars that of available instrumentation. As a result, the phase relation with distant lines cannot be evaluated with this standard method. By way of solution, two tunable laser frequency references, have been mixed with two spectral lines of a diode-comb in an SOA using a nonlinear four-wave mixing process [111]. This provides frequency translation so that spectral lines with large frequency separation can be detected by a photodiode and displayed by an RF spectrum analyzer. Alternatively, two tunable lasers have been mixed with the two spectral lines of a QD diode laser comb using an I/Q intradyne coherent detection [107]. This allows the complex optical fields of the two selected lines to be simultaneously converted into the electric domain for analysis. Both these techniques measure and compare only two selected spectral lines at a time. Characterization of a large number of spectral lines requires a series of independent measurements. The technique reported here is a multi-heterodyne detection method that allows simultaneous downshift of many optical spectral lines from a QD-MLL into the electrical domain. CMPN and DPN are obtained by analysis of electric domain waveforms. Although multi-heterodyne detection has been used to characterize phase profiles of frequency stabilized semiconductor comb sources [112,113], it has not to our knowledge been used to characterize differential-mode phase correlations among many mode locked spectral lines of QD-MLLs.

3.4.1 Theoretical Background

It has been predicted theoretically that the phase noise of each optical spectral line in a passively mode-locked diode laser can be expressed as [114]

$$\varphi_n(t) = \varphi_r(t) + \Delta\varphi_{r,n}(t) = \varphi_r(t) + (r - n)\delta\varphi(t) \quad (3.1)$$

where $\varphi_r(t)$ is a time-varying common-mode phase of a specific spectral line with line index r , $\Delta\varphi_{r,n}(t)$ is the differential phase between spectral line n and r where n is a variable, and $\delta\varphi(t)$ is the intrinsic differential-mode phase (IDMP) which is defined as the differential phase between adjacent spectral lines. For an optical frequency comb with the phase noise described by Eq. (3.1), the spectral linewidth of the n th spectral line can be expressed by [110]

$$\Delta v_n = \Delta v_r + \Delta v_{diff} \left(\frac{\lambda - \lambda_r}{\frac{F\lambda_r^2}{c}} \right)^2 \quad (3.2)$$

where Δv_r is a *common-mode spectral linewidth* of the reference spectral line r at wavelength λ_r , and Δv_{diff} is the intrinsic differential linewidth attributed to the IDMP noise between adjacent spectral lines separated by the pulse repetition frequency F . While the common-mode linewidth in a passively mode-locked diode laser originates from spontaneous emission and can be predicted by the modified Schawlow–Townes formula [115], differential linewidth is mainly attributed to the inter-pulse timing jitter.

Theoretically, if there is no correlation between the common-mode and the differential mode phase noises, the timing jitter $\delta t_j(t)$ is linearly proportional to the IDMP, $\delta\varphi(t)$, as [114]

$$\delta t_j(t) = \frac{\delta\varphi(t)}{2\pi F} \quad (3.3)$$

This indicates that the timing jitter $\delta t_j(t)$ is also a Gaussian random walk. The statistical nature of the timing jitter can be quantified by its standard deviation σ_j which is proportional to the square

root of the observation time T . That is $\sigma_j(T) = \sqrt{D \cdot T}$, where D is commonly referred to as the *diffusion constant* [114].

3.4.2 Comb Source Characterization with Multi-Heterodyne Technique

When a frequency comb signal from a comb source under test (CUT) with frequency repetition of F is mixed with a single-mode LO using the coherent receiver technique presented in Sec. 2.3, the resulting electrical signal will represent a down-converted version of the optical spectrum with same line spacing. Therefore, the maximum number of captured spectral lines will be limited by the available electrical bandwidth of the system B_e , $N_{max} \leq \lfloor B_e/F \rfloor$, as illustrated in Fig. 3.9(a), which limits the usefulness of this technique when the CUT has spectral spacing $F > 10$ GHz.

This bandwidth limitation can be avoided to allow the measurement of time-dependent phase relations among a large number of spectral lines. This is accomplished in a multiheterodyne technique, which uses a reference frequency comb as the LO in coherent heterodyne detection as illustrated in Fig. 3.9(b). The reference comb with an optical bandwidth B_o has a repetition frequency $F + \delta f$ which differs slightly from F of the CUT. Assume the first spectral line of the reference comb b_1 is a frequency Δ away from the closest spectral lines a_1 of the CUT, coherent mixing between b_n and a_n will create an RF spectral line e_n at frequencies $[\Delta + (n - 1)\delta f]$ (with $n = 1$ to 7 in the example shown in Fig. 3.9) on the positive frequency side of the RF spectrum. Meanwhile, mixing between b_n and $a_n + 1$ will create an RF spectral line d_n at frequencies $[(n - 1)\delta f - \Delta] - F$ on the negative frequency side as shown in Fig. 3.9(b). This coherent multiheterodyne mixing translates the CUT with line spacing F into an RF comb of line spacing $\delta f < F$. In order to avoid frequency aliasing, optical bandwidth $B_o \leq F^2/\delta f$ is required, and the maximum number of spectral lines that can be measured is $N_{max} \leq \lfloor B_e/\delta f \rfloor$ assuming that the single-side electric bandwidth of the coherent receiver is $B_e \geq F$. Note that if a simple coherent

detection is used with a single photodiode, only the amplitude of the optical field is detected. In such a case the maximum number of spectral lines that can be measured in the RF domain without spectral aliasing is determined by $N_{max} \leq \lfloor F/2\delta f \rfloor$ [116], which is only half compared to that using coherent I/Q detection.

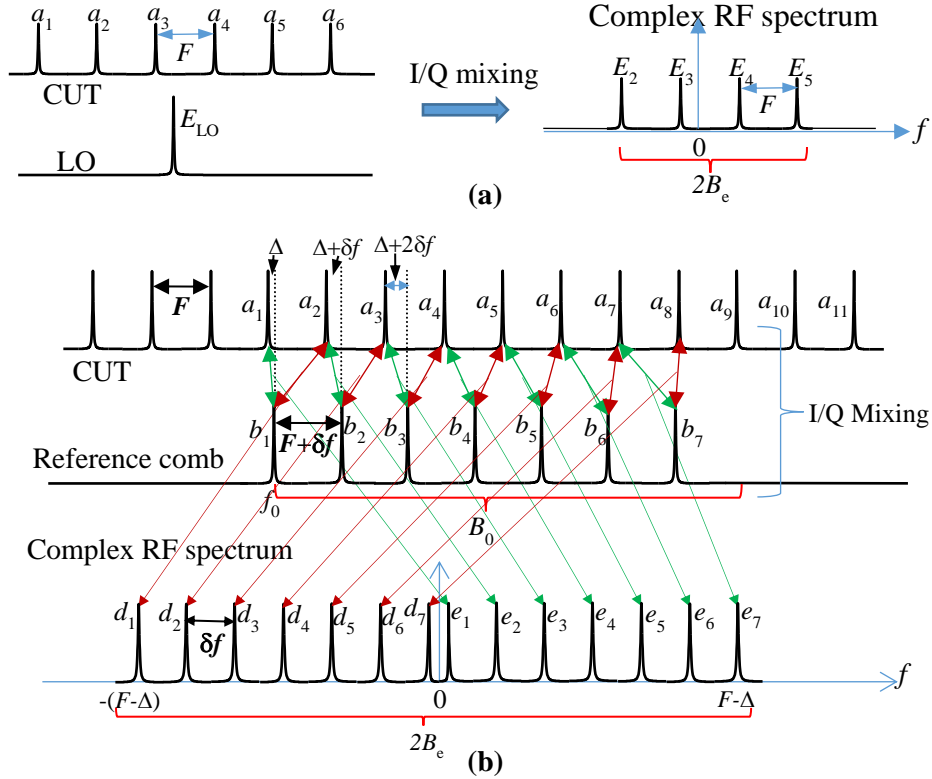


Fig. 3.9. (a) Illustration of coherent I/Q mixing between CUT with a repetition frequency F and a LO with a single spectral line. (b) Coherent I/Q mixing between CUT and a reference comb with a repetition frequency $F + \delta f$. Double-ended arrows indicate mixing between spectral lines and single-ended arrows indicate locations of resultant spectral lines in the RF domain.

For a more general analysis, the complex optical fields of the CUT and the reference comb, respectively, can be written as the superposition of discrete frequency components, i.e.,

$$A(t) = \sum_{n=1}^N a_n \exp\{j[2\pi f_{A_n} t + \varphi_{A_n}(t)]\} \quad (3.4)$$

$$B(t) = \sum_{n=1}^N b_n \exp\{j[2\pi f_{B_n} t + \varphi_{B_n}(t)]\} \quad (3.5)$$

where, a_n and b_n , are real amplitudes, f_{A_n} and φ_{A_n} are frequency and phase of the n^{th} spectral line of the CUT, and f_{B_n} and φ_B , are frequency and phase of the n^{th} spectral line of the reference comb where we assumed that φ_B is stable and independent of line number n . N is the total number of spectral lines of the reference comb. With coherent I/Q mixing, the photocurrents are $i_I(t) \propto \text{Re}(A^*B)$ and $i_Q(t) \propto \text{Im}(AB^*)$ for the I and Q channels, respectively. With coherent I/Q detection, two photocurrents are obtained, which can be combined to form complex RF waveforms and further decomposed into discrete frequency components as:

$$i_1(t) = i_I(t) - ji_Q(t) = \xi A^*B$$

$$= \xi \sum_{n=1}^N \sum_{k=1}^N a_n b_k \exp\{j[2\pi(k-n)Ft + 2\pi\Delta + 2\pi(k-1)\delta ft - \varphi_{A_n}(t) + \varphi_B(t)]\} \quad (3.6)$$

$$i_2(t) = i_I(t) + ji_Q(t) = \xi AB^*$$

$$= \xi \sum_{n=1}^N \sum_{k=1}^N a_n b_k \exp\{j[2\pi(n-k)Ft - 2\pi\Delta - 2\pi(k-1)\delta ft + \varphi_{A_n}(t) - \varphi_B(t)]\} \quad (3.7)$$

where, ξ is a proportionality constant, δf is the constant repetition frequency difference between the CUT and the reference comb, F is the repetition frequency of the CUT, and Δ is a frequency offset at $n = k = 1$.

Double-sided spectra can be obtained from Fourier transforms of photocurrents $i_1(t)$ and $i_2(t)$ of Eqs. (3.6) and (3.7), respectively. As illustrated in Fig. 3.9(b), each spectral line in the RF domain is a frequency-downshifted optical spectral line of the CUT. On the positive RF sideband of Fig. 3.9(b), each line is the mixing between A_n and B_n ($k = n$ in Eq. (3.6)), while on the negative side of the RF spectrum in Fig. 3.9(b), each line is the mixing between A_{n+1} and B_n ($k = n+1$ in Eq. (3.6)). For $k > n$ and $k < n-1$, the RF spectral lines will have frequencies higher than F and they are normally outside the bandwidth of the receiver.

Without loss of generality, consider the m^{th} spectral line (set $k = n = m$ in Eq. (3.6)) on the positive side of the RF frequency, which is the Fourier Transform of

$$i_{1m}(t) = \xi a_m b_m \exp[2\pi(m-1)\delta f t + 2\pi\Delta - \varphi_{A_m}(t) + \varphi_B(t)] \quad (3.8)$$

Decomposing the phase noise $\varphi_{A_m}(t)$ into a common-mode phase $\varphi_r(t)$ and a differential phase $\Delta\varphi_{r,n}(t)$ as defined in Eq. (3.1) for the CUT, Eq. (3.8) becomes

$$i_{1m}(t) = \xi a_m b_m \exp[2\pi(m-1)\delta f t + 2\pi\Delta - \varphi_r(t) - \Delta\varphi_{r,m}(t) + \varphi_B(t)] \quad (3.9)$$

Similarly, let $k = n$, Eq. (3.7) is modified to

$$i_2(t) = \xi \sum_{n=1}^N a_n b_n \exp\{j[-2\pi(n-1)\delta f t - 2\pi\Delta + \varphi_r(t) + \Delta\varphi_{r,n}(t) - \varphi_B(t)]\} \quad (3.10)$$

where $\Delta\varphi_{r,m}(t)$ and $\Delta\varphi_{r,n}(t)$ are differential phases between spectral lines m and r , and n and r , respectively, for the CUT.

As both $i_1(t)$ and $i_2(t)$ obtained from the coherent receiver can be digitized and recorded; DSP such as filtering and mixing can be performed in the digital domain offline. Selecting the m^{th} spectral component $i_{1m}(t)$ from the positive frequency side of the RF spectrum with a digital filter, mixing it with the negative frequency side of the spectrum $i_2(t)$, the complex conjugate of the mixing products will be

$$\{i_{1m}(t)i_2(t)\}^* = \xi^2 a_m b_m \sum_{n=1}^N a_n b_n \exp\{j[2\pi(n-m)\delta f t + \Delta\varphi_{mn}(t)]\} \quad (3.11)$$

where $\Delta\varphi_{mn}(t) = \Delta\varphi_{r,m}(t) - \Delta\varphi_{r,n}(t)$ is phase difference between the n^{th} and m^{th} spectral lines.

This digital mixing process allows us to separate the DPN from the CMPN.

3.4.3 Experimental Setup and Results

In the experiment a laser frequency comb source is used as the CUT, which is a single-section InAs/InP QD-MLL with a pulse repetition frequency of 11 GHz. The laser emits phase locked

discrete spectral lines ranging from 1540 nm to 1550 nm. A detailed description of the laser structure can be found in Ref. [88]. Although not hermetically sealed by telecommunications standard, this QD-MLL is packaged with standard temperature control and low noise current control, and the optical output is coupled to a polarization-maintaining (PM) fiber pigtail through an optical isolator. Device temperature, injection current, and the average output optical power can be monitored through a computer interface. The optical spectrum shown in Fig. 3.10(a) was measured with an optical spectrum analyzer OSA (RBW = 0.01 nm). All experiments reported in this section were performed with 400 mA constant bias current on the laser, and the optical power at the output of the PM fiber pigtail was approximately 10 mW. This operation point was chosen to obtain an optimally flat optical spectrum in the wavelength window from 1540 nm to 1550 nm. Different bias conditions can result in different phase noise characteristics, as may be found by comparing the results presented here and in elsewhere in this dissertation, for the same device.

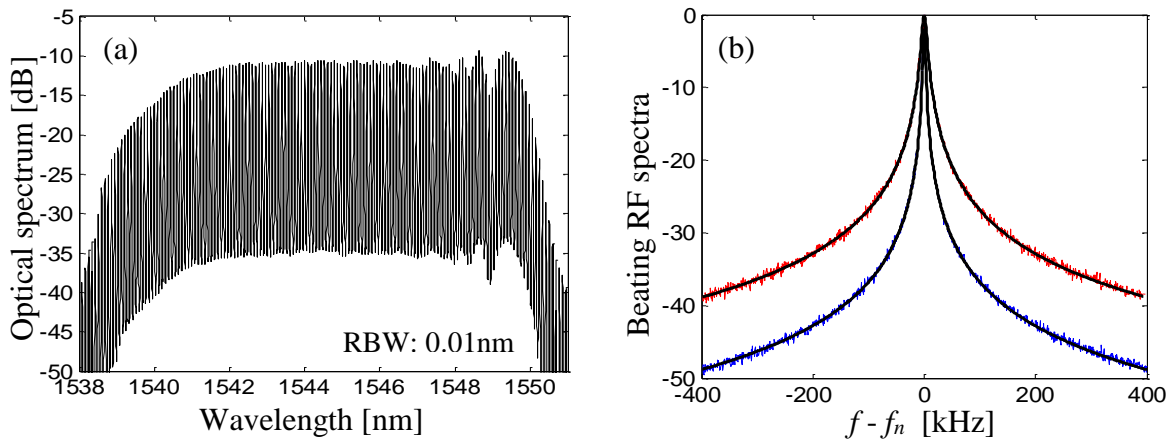


Fig. 3.10. (a) Optical spectral density of the QD-MLL measured with 0.01nm resolution bandwidth, and (b) RF spectra of the 1st and the 2nd order beating notes and Lorentzian fitting, where the frequency has been shifted by the central frequency f_n ($n = 1, 2$) of each peak.

The beat signal of adjacent spectral lines was first measured with direct detection in a high-speed photodiode and an ESA [109]. Figure 3.10(b) shows the 1st and 2nd order beating spectra recorded by the ESA with 25 GHz RF bandwidth. The central frequency of each peak has been

downshifted to 0 for comparison. The peak of the 1st order beating tone at $f_1 = 11$ GHz is the mixing between all adjacent spectral lines, and the 2nd order beating at frequency $f_2 = 22$ GHz is the mixing between all next-nearest lines. These mixing spectra can be fitted to a Lorentzian line shape (given by Eq. (2.4) in Chapter 2). The continuous lines in Fig. 3.10(b) show the Lorentzian fits with the FWHM linewidths of 2.9 kHz and 9.1 kHz for the 1st order and the 2nd order mixing peaks, respectively. The narrow RF linewidths shown indicate that adjacent optical spectral lines of the QD-MLL are highly correlated with low IDMP noise. However, the optical phase noise of individual lines can be much larger, some multiple megahertz in the linewidth.

The spectral linewidths were then measured using coherent heterodyne detection by mixing the QD-MLL output with an external-cavity tunable laser (<50 kHz spectral linewidth) in an *I/Q* coherent receiver. I and Q photocurrents were digitized and recorded by a dual-channel real-time oscilloscope at 50 GS/s sampling rate. Complex RF spectra are derived from Fourier transformation of these photocurrents. An example of the measured RF spectrum is shown in Fig. 3.11(a). As illustrated in the inset, assume that there are three spectral lines a_1 , a_2 and a_3 of the QD-MLL near the optical frequency of the local oscillator E_{LO} . The optical frequency of the local oscillator is set approximately 2.9 GHz away from the nearest spectral line (a_2) of the QDLFC, and the coherent *I/Q* receiver downshifts the optical spectrum into the RF domain with three RF spectral lines $a_1 E_{LO}$, $a_2 E_{LO}$, and $a_3 E_{LO}$ at -8.1 GHz, 2.9 GHz and 13.9 GHz, respectively. The complex nature of the composite photocurrent obtained from coherent *I/Q* detection avoids spectral aliasing about the zero frequency. The FWHM of each RF spectral line can be evaluated from the recorded *I/Q* photocurrent signals based on the PSD. The inset of Fig. 3.11(b) shows an example of the measured PSD of the phase, $S_{\Delta\phi}(f)$, with the characteristic -20 dB/dec slope with respect to frequency so that $f^2 S_{\Delta\phi}(f)$ should be relatively independent of the frequency. Hence

the linewidth can be obtained by averaging the values of $2\pi f^2 S_{\Delta\phi}(f)$ between 100 kHz and 10MHz.

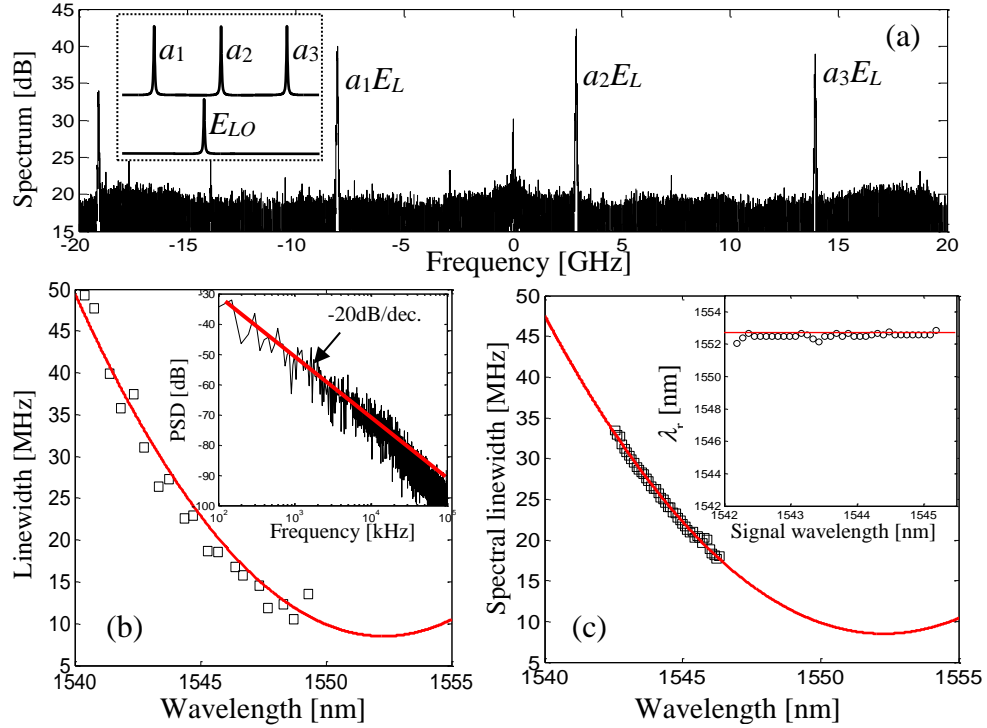


Fig. 3.11. (a) Example of measured spectrum of heterodyne detection using a tunable external cavity laser as the local oscillator, (b) measured spectral linewidths (square markers) of spectral lines at different wavelengths by tuning the LO wavelength across the window, and parabolic fitting (solid line); inset in (b) is an example of phase noise PSD and -20dB/dec. fitting, and (c) spectral linewidth extracted from the phase of each spectral line in (a) below in multiheterodyne measurement. Solid line is the same parabolic fit as that in (b). Inset in (c) shows wavelength of minimum linewidth predicted by minimum correlation between common-mode and IDMP noises.

By tuning the wavelength of the LO from 1540 nm to 1549.5 nm, the linewidths of different spectral lines of the QD-MLL were measured across that range. Results are shown as square markers in Fig. 3.11(b). The solid line in the figure shows fitted parabolic dependence with wavelength as defined in Eq. (3.2) with $\Delta\nu_r = 8.5$ MHz as the minimum linewidth extrapolated at wavelength $\lambda_r = 1552.3$ nm, which lies outside the comb emission spectrum, and $\Delta\nu_{diff} = 2.1$ kHz as the linewidth attributed to the IDMP noise between adjacent spectral lines separated by $F = 11$ GHz. The parabolic shape of linewidth as the function of wavelength shown in Fig. 3.11(b)

agrees with those previously reported in Refs. [110,114]. The location of minimum linewidth outside the emission spectrum is unusual, but this observation is supported also by multi-heterodyne measurements reported below. The offset of the minimum linewidth spectral line from the center of the optical spectrum is attributed to the temporally asymmetric chirped pulses, as was suggested in Ref. [110].

In order to measure a large number of spectral lines of the QD-MLL simultaneously and investigate phase relations between these lines, a multi-heterodyne measurement setup was implemented, in which a reference comb was created by means of a recirculating loop. Figure 3.12 shows the block diagram of the experimental setup with the details of reference comb implementation. An electro-optic I/Q modulator inside a re-circulating loop performs carrier-suppressed single-sideband modulation on the input optical signal [117]. This modulator is driven by an RF oscillator at frequency $F + \delta f$, with $F = 11$ GHz. The RF oscillator determines the repetition frequency of the reference comb. $\delta f = 200$ MHz sets the frequency difference between the reference comb and the QDLFC. A tunable external cavity semiconductor laser at an optical frequency f_o serves as seed. It has a spectral linewidth < 50 kHz. Two intra-loop EDFAs compensate for the power loss of optical components and modulation efficiency of the I/Q modulator. On every loop roundtrip, the optical signal is frequency shifted by $F + \delta f$. A 4-nm optical bandpass filter (O-BPF) limits the optical bandwidth of the reference comb. The alignment of spectral lines in multi-heterodyne detection is illustrated in Fig. 3.9(b), and experimentally the optical frequency of the first spectral line of the reference comb, f_o , can be adjusted with respect to the frequency of a particular spectral line of the QD-MLL. The mode spacing difference, δf , can be adjusted with the RF drive on the I/Q modulator. The two combs are mixed in a coherent

receiver with balanced photodetectors which provide the I/Q photocurrents. A polarization controller is used to match the state of polarizations between the reference comb and the QD-MLL.

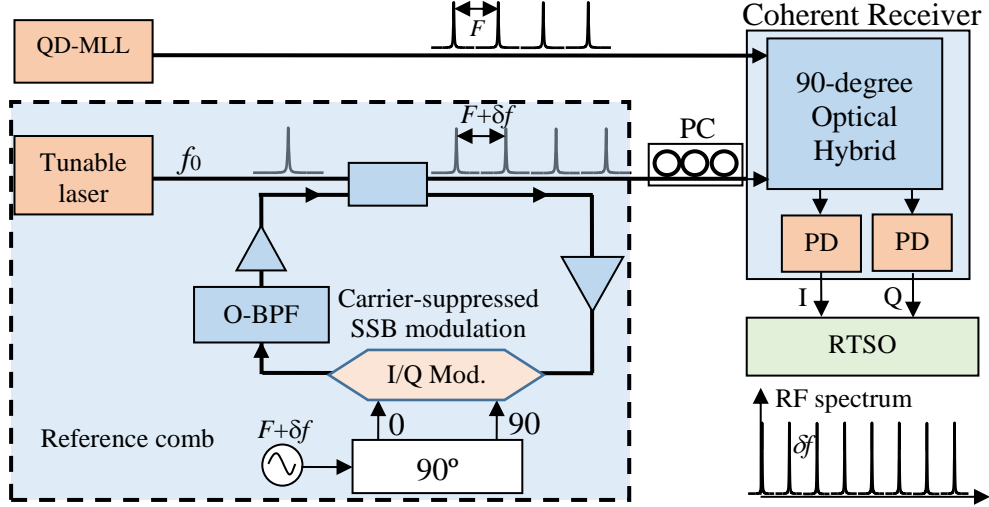


Fig. 3.12. Experimental setup for multi-heterodyne experiment, where a reference comb is generated by a re-circulating loop resonator.

A dual-channel RTSO at 50 GS/s sampling rate was used to record the I and Q components, and a complex multi-heterodyne RF spectrum with frequency spacing δf between adjacent RF spectral lines is obtained through a Fourier Transform. $\delta f = 200$ MHz was chosen in the experiment to avoid spectral overlap between adjacent spectral lines in the RF domain. Within the available RF bandwidth of 11 GHz (set by the QD-MLL mode spacing), the maximum number of spectral lines N_{max} was about 55. Figure 3.13 shows the optical spectra of the QD-MLL together with the reference comb generated by the re-circulating loop resonator with a bandpass optical filter (1542.3-1546.5 nm) at a repetition frequency of 11.2 GHz. Within the 4.-nm (~ 525 GHz) optical bandwidth, the reference comb has approximately 50 spectral lines. Owing to its comparative narrow linewidth (< 50 kHz vs. ~ 10 MHz for the QD-MLL) we treat the reference comb as an “ideal” frequency reference with negligible phase noise. The magnitude variation of the reference comb lines across the wavelength is mainly caused by polarization mode dispersion

(PMD) as the loop is composed of a mixture of PM fiber (pigtailed of I/Q modulator) and non-PM fiber (EDFAs), which created wavelength-dependent polarization rotation. Amplified spontaneous emission (ASE) noise also accumulates in the loop, degrading optical signal-to-noise ratio (OSNR), especially in the long wavelength side. However, as long as the SNR of each spectral line in the RF spectrum is high enough, phase retrieval will not be affected significantly by the flatness of the line amplitudes.

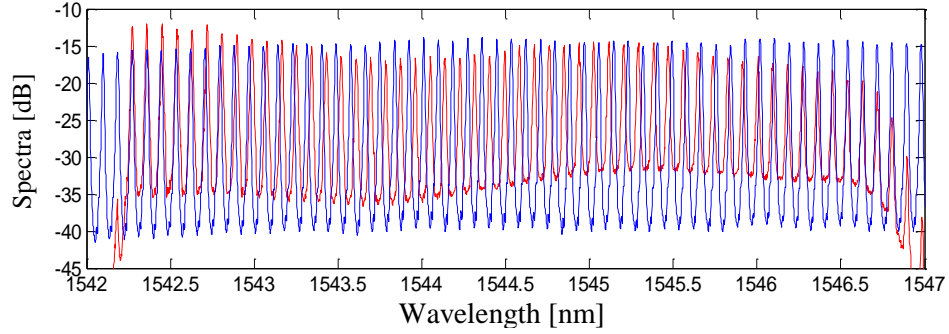


Fig. 3.13. Measured optical spectra of the comb laser source (blue) plotted together with the reference comb (red) in the 1542.3-1546.5-nm wavelength window.

Figure 3.14 shows the double-sided spectra obtained from Fourier transforms of photocurrents $i_1(t)$ and $i_2(t)$ of Eqs. (3.6) and (3.7), respectively. On the positive sideband of Fig. 3.14(a), each line is the mixing between A_n and B_n ($k = n$ in Eq. (3.6)), while on the negative side of the spectrum in Fig. 3.14(a), each line is the mixing between A_{n+1} and B_n ($k = n - 1$ in Eq. (3.6)). The spectrum shown in Fig. 3.14(b) is the complex conjugate of that shown in Fig. 3.14(a).

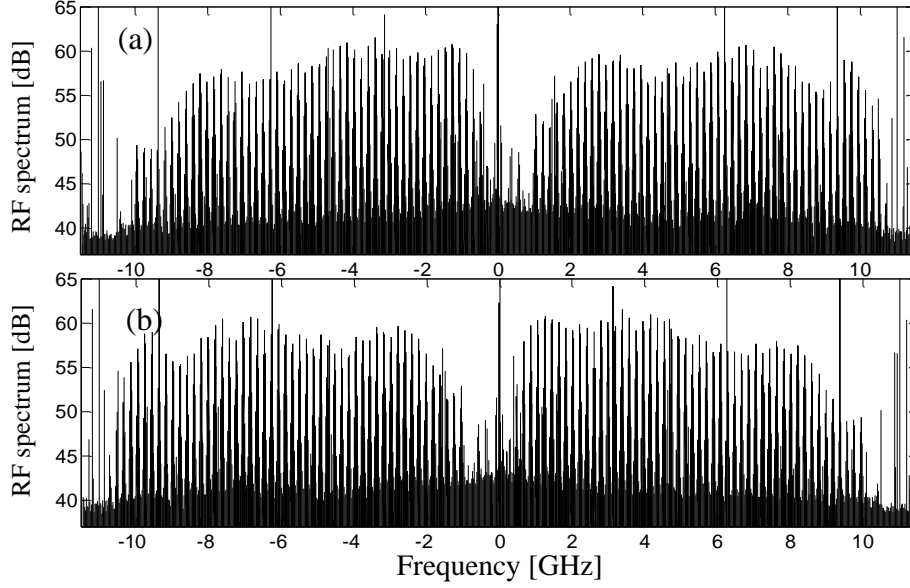


Fig. 3.14. RF spectra obtained by Fourier transform of (a) $i_I(t) - ji_Q(t)$ and (b) $i_I(t) + ji_Q(t)$.

As each RF spectral line shown in Fig. 3.14 is a frequency-downshifted optical spectral line of the QD-MLL, it includes both CMPN and DPN. In order to separate the contributions of common-mode and differential phases as the function of time, we used RF mixing technique in the digital domain as described by Eqs. (3.9)-(3.11). For convenience, Fig. 3.15(a) shows the positive frequency side of Fig. 3.14(a) which includes about 55 spectral lines of QD-MLL in the window from 1542.3 nm to 1546.5 nm. RF mixing using the m^{th} spectral line as the phase reference can remove the contribution of $\varphi_r(t)$ from the multi-heterodyne spectrum, and the impact of the reference comb phase $\varphi_B(t)$ is also removed as indicated in Eq. (3.11). For Fig. 3.15(b), the lowest index spectral line is used as the phase reference ($m = 1$) corresponding to the optical spectral line at 1542.3 nm. As a result, it has the narrowest spectral linewidth and the highest peak spectral density. Due to the differential phase noise with respect to this reference spectral line, linewidth increases and peak spectral density decreases with the increase of the line index $|n|$. Figure 3.15(c) shows the spectrum in which the phase reference is chosen in the middle of the band with $m = 25$, corresponding to an optical wavelength of approximately 1544.5 nm. Thus, the relative frequency

is zero at the 25th spectral line counting from the left side of the spectrum, which has the narrowest linewidth and the highest peak spectral density.

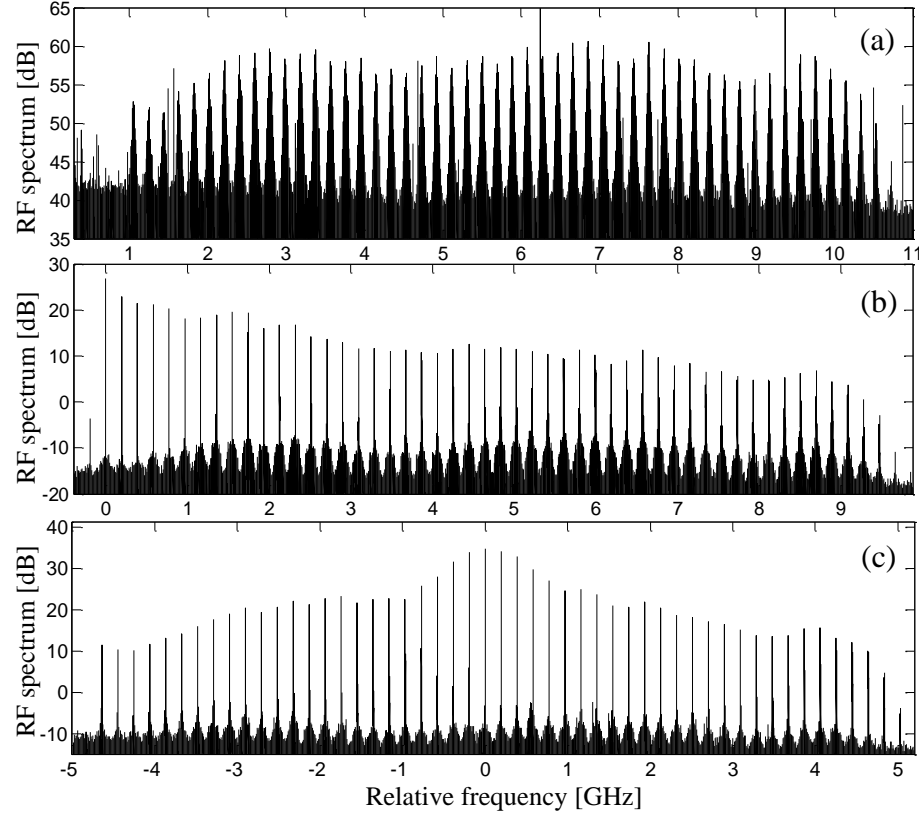


Fig. 3.15. Positive-frequency side of the multi-heterodyne RF spectrum, (b) Spectrum obtained after removing the common-mode phase noise using the first spectral line ($m = 1$) as the reference, (c) same as (b) but the 25th spectral line ($m = 25$) is used as the phase reference.

The cancelation of common-mode optical phase noise through RF mixing allows evaluation of differential phase noise, which determines mutual coherence between different spectral lines. Figure 3.16(a) shows the waveforms of differential phase as a function of time for the spectral lines of $n = 1, 10, 20, 30$, and 40 with the first line ($m = 1$) used as the reference line. These differential phase waveforms were obtained by shifting the central frequency of the target spectral line, n , in Fig. 3.15(b) to zero and extracting phase information $\Delta\phi_{mn}(t)$ by digital processing. In this process, the average differential phase within the observation time window has been set to zero. It is apparent that waveforms of differential phase of different spectral lines are

highly correlated with a correlation factor of $>97\%$ for all traces shown in Fig. 3.16(a). Figure 3.16(b) shows the differential phase waveforms of lines $n = 1, 10, 20, 30$, and 40 normalized by the line separation from the reference line m , this results in the IDMP $\delta\varphi(t) = \Delta\varphi_{mn}(t)/(n - m)$, for $n \neq m$, which is the differential phase between adjacent spectral lines. The result of almost identical waveforms of $\delta\varphi(t)$ obtained from a large number of spectral lines shown in Fig. 3.16(b) suggests that they were originated from a common perturbation source, which is the timing jitter.

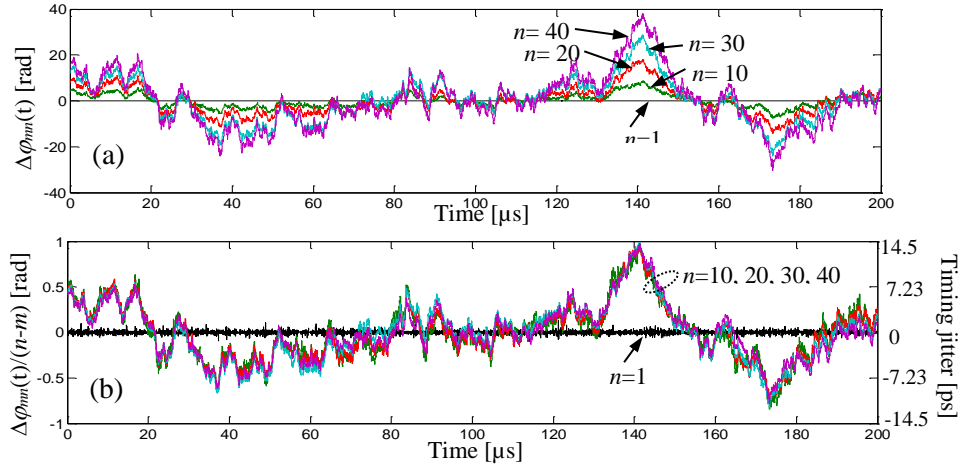


Fig. 3.16. (a) Differential phase $\Delta\varphi_{mn}(t)$ of lines 1, 10, 20, 30 and 40 as the function of time with $m = 1$ as the reference line, and (b) differential phase normalized by line separation with the reference line m .

To demonstrate that Eq. (3.11) is valid independent of the selection of the reference line, Fig. 3.17(a) and (b) show the differential phase $\Delta\varphi_{mn}(t)$ and the IDMP $\delta\varphi(t)$, respectively where $m = 25$ is the chosen reference line (at the middle of the spectral window). Figure 3.17 shows that differential phases move to opposite directions for spectral lines on the left ($n < m$) and the right ($n > m$) sides of the reference line m as anticipated by $\Delta\varphi_{mn}(t) = \delta\varphi(t)(n - m)$, where $\delta\varphi(t)$ remains independent of n and m . The observed n -independence of the IDMP $\delta\varphi(t)$ is consistent with a timing jitter interpretation. The right y-axes of Figs. 3.16(b) and 3.17(b) indicate the corresponding timing jitter values, which are linearly related to $\delta\varphi(t)$ as defined by Eq. (3.3). Within the 200 μs observation time, the timing jitter can reach as much as ± 14 ps. The standard

deviation of $\delta\varphi(t)$ can be found as $\sigma_j = 4.4$ ps within this observation time, corresponding to a diffusion constant $D = 9.7 \times 10^{-5}$ fs. The diffusion constant is more than 2 orders of magnitude less than reported elsewhere for a similar laser [114].

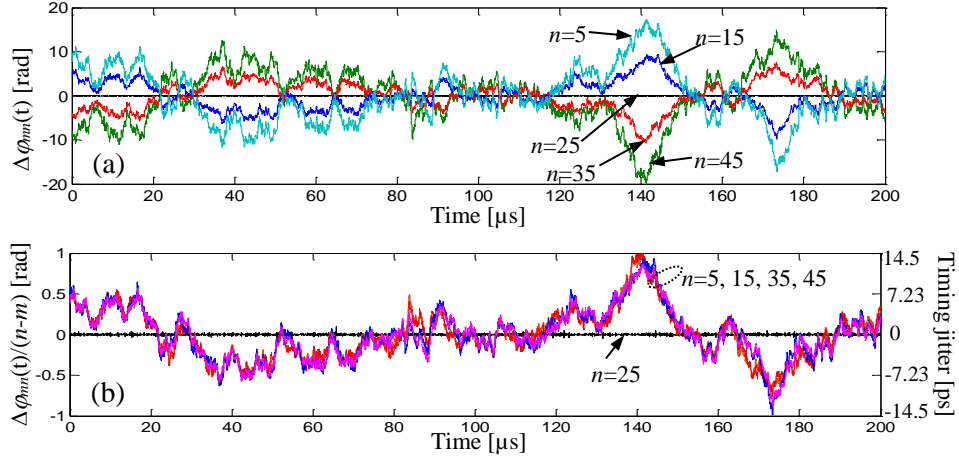


Fig. 3.17. Same as Fig. 3.16, except that $m = 25$ is chosen as the reference line.

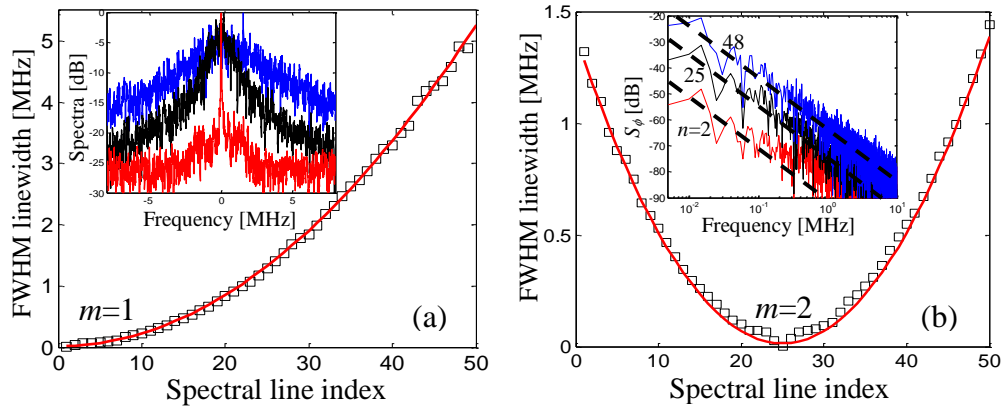


Fig. 3.18. FWHM spectral linewidth as the function of the spectral line index for reference line chosen as $m = 1$ (a) and $m = 25$ (b). Examples of spectral line shapes (inset in (a)), and phase noise power spectral densities (insets in (b)) of $n = 2$ (red), 25 (black), and 48 (blue). Both insets were obtained with $m = 1$ as the reference line.

Once a reference spectral line is assigned, the spectral linewidth of the differential phase noise can be obtained from the power spectral densities of these differential phase waveforms $\Delta\varphi_{mn}(t)$ (shown in Figs. 3.16(a) and 3.17(a)) as $\Delta\nu = 2\pi f^2 S_{\Delta\varphi_{mn}}(f)$. Figure 3.18 shows the measured

differential phase noise linewidth as the function of n . With $m = 1$ used as the reference in Fig. 3.15(b) the linewidth increases monotonically as the line index increases, and reaches ~ 5 MHz at the maximum line index of $n = 49$, a frequency separation of 520 GHz (~ 4.2 nm) from the reference. When $m = 25$ is chosen as the reference as shown in Fig. 3.15(c), linewidths increase parabolically on either side of the reference as shown in Fig. 3.18(b).

Solid lines in both Figs. 3.18(a) and 3.18(b) show parabolic fitting to the differential linewidth as the function of the line index n by

$$\Delta v_n = \Delta v_{am} + (n - m)^2 \Delta v_{pm} \quad (3.12)$$

where, $m = 1$ and $m = 25$ are the indices of reference spectral lines used in Figs. 3.18(a) and 3.18(b), respectively. $\Delta v_{am} = 15$ kHz and $\Delta v_{pm} = 2.1$ kHz are used to best fit the measured results in both figures. As the RF power spectral density is the autocorrelation of the optical field in this measurement, amplitude noise has a contribution to the measured spectral linewidth, which is represented by Δv_{am} , and is independent of the line index n . Whereas Δv_{pm} is the same as Δv_{diff} defined in Eq. (3.2), which originates from timing jitter and introduces differential phase noise between spectral lines, and thus the differential linewidth increases quadratically as the line index moving away from the reference line [118]. The inset in Fig. 3.18(a) show examples of spectral line shapes with $n = 2, 25$ and 48 with $m = 1$ as the reference line. The corresponding power spectral densities of the phase noise $S_{\Delta\phi}(f)$ of these three spectral lines are shown in the inset of Fig. 3.18(b), with dashed straight lines representing the -20 dB/dec slope, indicating classic Gaussian statistics of the phase noise. Notice that for $n = 2$, high frequency components of the phase noise are increased due to the reduced SNR in the measured differential phase waveform when the phase variation is small. The intrinsic differential linewidth Δv_{pm} of 2.1 kHz measured here is much narrower than that previously reported 48.5 kHz for a passively mode-locked

semiconductor quantum-dash laser [114]. This explains why the diffusion constant D measured here is more than two orders of magnitude smaller than that reported in Ref. [114].

For a passively mode-locked semiconductor laser, optical phase noise consists of a common-mode component originated from spontaneous emission, and a differential-mode component attributed to the timing jitter, as predicted by Eq. (3.1). These two components should be uncorrelated since they arise from different physical processes. Equation (3.1) suggests that there exists a mode index r at which all phase noise is common-mode, and the phase noise of line r is substantially uncorrelated with the IDMP noise.

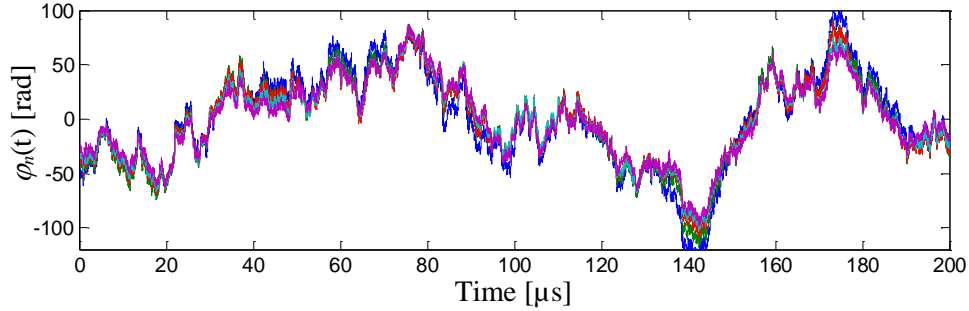


Fig. 3.19. Optical phase of spectral lines $n = 5, 10, 20, 30$ and 40 shown in the spectrum of Fig. 3.15(a) without common-mode phase noise cancellation.

Figure 3.19 shows the optical phases noise $\varphi_n(t)$ as the function of time for spectral lines $n = 5, 10, 20, 30$, and 40 extracted from the spectrum shown in Fig. 3.15(a) without common-mode phase noise cancellation. The optical spectral linewidths can be obtained from the PSD of the optical phase $\varphi_n(t)$ of each spectral line. These results are shown in Fig. 3.11(c). The solid line in Fig. 3.11(c) is the same parabolic fitting as used to obtain Fig. 3.11(b) based on Eq. (3.2) with $\Delta\nu_r = 8.5$ MHz, $\lambda_r = 1552.3$ nm, $\Delta\nu_{diff} = 2.1$ kHz, and $F = 11$ GHz.

Using Eq. (3.1) we search for an integer value r which minimizes the correlation between $[\varphi_n(t) - (n - r)\delta\varphi(t)]$ and $\delta\varphi(t)$ for each measured spectral line n . Then, the optical frequency corresponding to the spectral line r can be found by $f_r = f_n + (r - n)F$. The inset in Fig.

3.11(c) shows the wavelength $\lambda_r = c/f_r$ that corresponds to the minimum optical spectral linewidth predicted by a group of measured spectral lines in the 1542.3 nm-1544.5 nm band. The average of these measurements points to $\lambda_r = 1552.3$ nm which agrees with the optical linewidth measurements and parabolic fitting shown in Figs. 3.11(b) and (c). For this particular device, λ_r is outside the mode-locking bandwidth of the QD-MLL and the common-mode phase noise waveform cannot be directly measured at that location. However, with the knowledge of the line index r corresponding to the wavelength of λ_r , the common-mode optical phase noise waveform $\varphi_r(t)$ can be extracted based on Eq. (3.1) as shown in Fig. 3.20 (red curve). The black curve in Fig. 3.20 is the IDMP noise $\delta\varphi(t)$ magnified by a factor of 65 for display purposes. The correlation between $\varphi_r(t)$ and $\delta\varphi(t)$, is -3×10^{-4} .

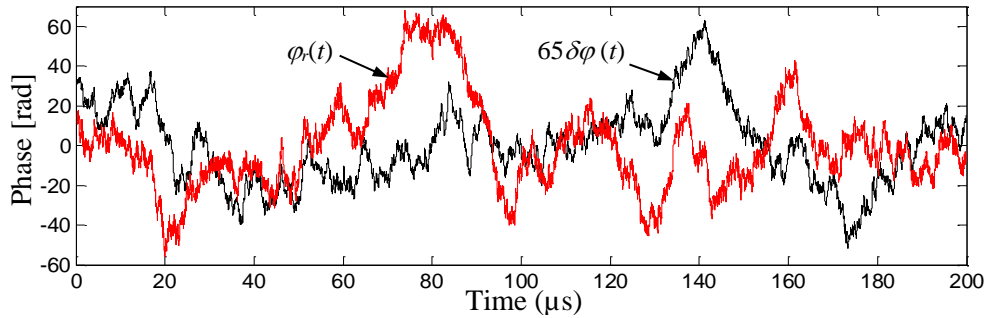


Fig. 3.20. Comparison between common-mode phase noise (red) and IDMP noise (black) waveforms.

This page intentionally left blank

Chapter 4

Optical Comb-Based SSB Superchannel Generation with Kramers-Kronig Reception

For their capability of electronic dispersion compensation, transmission systems based on direct detection of single-sideband (SSB) signals are attractive candidates as energy-efficient and cost-effective alternative solutions to intradyne digital coherent systems for inter-data-center and metro applications. The Kramers-Kronig (KK) receiver scheme has been shown to provide superior performance compared to other schemes in signal-to-signal beat interference (SSBI) cancellation in these direct-detection systems. In this chapter, we propose a low-complexity and cost-effective scheme of generating an optical superchannel comprising multiple SSB channels, based on a single quantum-dot mode-locked laser source (QD-MLL). The proposed system does not require additional photonic or RF components at the transmitter to generate the required SSB signal with a continuous wave (CW) carrier. It also preserves the full digital-to-analog converters' bit resolution for data modulation, in contrast to other methods based on digital generation of the CW component. Simulations of system performance with KK receiver, based on measured laser output field show that the proposed system can achieve BER below the hard-decision forward error correction threshold for 16-QAM Nyquist SSB signals after transmission through 3 amplified spans of single-mode fiber in a 240 km link. Using 8 KK channels at 23 GBd each, the proposed scheme will be able to achieve a transmission rate of 736 Gb/s with noncoded spectral efficiency

of 2.45 b/s/Hz. The impacts of carrier-to-signal power ratio, per channel launch power into the fiber, and component frequency drifting on transmission system performance are also discussed.

4.1 Introduction

The increasing demand for high data rate and high interface density optical links for metro, long reach data center interconnect (DCI) and backhaul applications has brought increased interest in developing cost-effective and energy-efficient transmission schemes to operate at ≥ 100 Gb/s. The optical links in such applications may extend from several tens to a few hundred kilometers, making electronic dispersion compensation (EDC) an essential requirement. Direct-detection (DD) optical receivers with a single photodiode (PD) and an analog-to-digital converter (ADC) are attractive candidates for these applications for their low cost and low complexity, compared to coherent detection. As was explained in Sec. 1.3.2 in Chapter 1, to enable complex field modulation and EDC in DD systems, the signal must be transmitted in SSB so that the complex optical field can be translated to the electric domain at the receiver for digital processing.

The CW tone required for SSB transmission can be added either at the receiver side or at the transmitter side, and the ratio of this CW power to the SSB signal power must be sufficient to satisfy the minimum phase condition required for linear reconstruction of the complex envelope of the SSB optical signal [28]. The first option is equivalent to a coherent optical receiver as a tunable laser source has to be available at the receiver which makes the hardware more complicated [52]. In comparison, generating the CW tone at the transmitter side is more practical for a simpler receiver structure. There are different techniques used to generate the CW tone at the transmitter, each has its own intrinsic advantages and disadvantages. The CW component can be generated by biasing an electro-optic I/Q modulator above the null point and driving its inputs with the I and Q components of a SSB signal generated by digital subcarrier modulation (SCM) of the baseband

data [29,53]. In this case, the maximum optical SSB signal bandwidth is equal to the analog bandwidth B of the digital-to-analog converters (DACs) and the I/Q modulator. For the same DAC and modulator bandwidth B , the optical signal bandwidth can be doubled by utilizing carrier-suppressed complex double-sideband modulation. The CW tone can then be added at either side of the spectrum, either digitally, known as the digital virtual carrier [54], or in the analog domain by adding an RF local oscillator signal directly to the optical I/Q modulator driving signals [55,56]. For these two bandwidth-efficient carrier insertion techniques, the first method has the disadvantage of reduced DAC resolution available for data signals by at least 50% because of the increased dynamic range of the signal (by a factor of ≥ 2) to achieve the minimum phase condition, which affects system's performance for high order modulation formats, hence limits the SE [41]. The second method adds complexity to the system as an additional RF LO and wideband and sharp analog diplexers would be required to combine signals from LO and DACs without imposing significant power losses. In comparison, directly inserting a CW optical tone after the modulator may provide a better solution as it allows full utilization of the analog bandwidth of DACs and optical modulator and preserves the full bit resolution of the DACs for the information-bearing signals. Nonetheless, generating an independent CW optical tone with a precise frequency shift from the modulated optical signal will require another optical frequency-locked laser source. Otherwise, carrier-suppressed single sideband optical modulation can be used to generate a frequency-shifted optical carrier to be added to the modulated SSB signal through an optical coupler [56,119]. This added complexity to the transmitter can be significant when multiple wavelength channels are used for WDM, which is the practical case in the intended applications of metro and DCI networks.

In this work, we propose a simple and energy-efficient scheme of generating multiple SSB signals in a superchannel configuration [120] based on a single QD-MLL optical comb source and dual SCM of SSB channels. Unlike the methods mentioned above, in our proposed scheme no additional optical or RF components are needed for the generation of the CW tones. The dual SSB channel modulation allows for ~93% utilization of the DACs and I/Q modulator analog bandwidth for high baud rate systems (~20 GBd) and does not reduce the available DAC bit resolution for data modulation. Individual spectral lines from a QD-MLL comb source usually exhibit higher intensity and phase noises compared to single-wavelength sources used in communication applications, like DFB lasers. Phase noise from individual comb lines from a QD-MLL is higher than that of a typical DFB laser (as was shown in Chapter 3). However, our proposed scheme utilizes the mutual coherence between adjacent spectral lines of a QD-MLL, which usually has very low differential phase noise equivalent to a linewidth of only a few tens to a few hundred kHz [78,107]. This will reduce the receiver penalty due to laser phase noise compared to typical DFB lasers. Equivalent results can only be obtained from high quality and relatively expensive ECLs if the CW component is to be added from a separate laser source. System performance simulations, based on experimentally-recorded complex optical field of QD-MLL, show that even in the presence of relatively high intensity noise the proposed system performs well below the hard-decision forward error correction (HD-FEC) threshold BER with 16-QAM modulation for up to 240 km of standard single-mode fiber (SSMF). This makes this system an attractive solution for long-reach DCI and metro applications.

The rest of the chapter is organized as follows: Section 4.2 provides an overview of the KK scheme, the impacts of laser phase noise and intensity noise, and presents the proposed superchannel generation scheme. Section 4.3 presents the details of the experimental setup and the

results of QD-MLL characterization. Results of system performance analysis based on semi-numerical simulations are presented in Sec. 4.4, and Sec. 4.5 provides the conclusions.

4.2 SSB-Modulated Superchannel Generation

4.2.1 The Kramers-Kronig Self-Coherent Scheme

The KK field reconstruction algorithm is based on an essential condition of minimum phase, where the phase of an optical signal satisfying this condition can be recovered from the detected intensity [28]. Ideally, in the absence of phase noise and intensity noise, the complex envelope of the optical signal at the PD can be expressed as

$$E(t) = E_c + S(t) \exp(j\pi Bt), \quad (4.1)$$

and the photocurrent generated at the output of the PD, assuming a unit responsivity, is then given by

$$\begin{aligned} i(t) &= |E(t)|^2 \\ &= E_c^2 + |S(t)\exp(j\pi Bt)|^2 + E_c^* \cdot S(t) \exp(j\pi Bt) + E_c \cdot S^*(t) \exp(-j\pi Bt) \end{aligned} \quad (4.2)$$

where E_c is a CW carrier component, $S(t)$ is the QAM modulated signal with total bandwidth B , and x^* represents the complex conjugate of x . $\exp(j\pi Bt)$ in Eq. (4.1) indicates that $S(t)$ is frequency shifted from the carrier tone E_c by $B/2$ Hz, or equivalently, the carrier component E_c is sitting at the edge of the spectrum of $S(t)$. On the right-hand side of Eq. (4.2), the first term is a constant DC term, the second term represents SSBI, and the third term is the useful signal-carrier beat term containing $S(t)$. The last term is the complex conjugate of the useful signal on the opposite side of the spectrum as $i(t)$ is real. The carrier-to-signal power ratio (CSPR) of $E(t)$ in Eq. (4.1) is defined as $CSPR = E_c^2 / \langle |S(t)|^2 \rangle$, which must be high enough to satisfy the minimum phase condition required for the KK field reconstruction [28]. $\langle \cdot \rangle$ denotes time averaging.

With the KK algorithm, the reconstructed complex field signal can be obtained by

$$E_{rec}(t) = \sqrt{i(t)} \exp[j \cdot \phi_E(t)], \quad \phi_E(t) = \mathcal{H} \left\{ \log \left(\sqrt{i(t)} \right) \right\} \quad (4.3)$$

where $\mathcal{H}\{\cdot\}$ represents the Hilbert Transform. This reconstructed signal can be expressed as $E_{rec}(t) = E_{DC} + S_{rec}(t) \exp(j\pi Bt)$, where E_{DC} is a DC component. The baseband complex data signal $S_{rec}(t)$ can be recovered by subcarrier demodulation as

$$S_{rec}(t) = \{E_{rec}(t) - E_{DC}\} \cdot \exp(-j\pi Bt) \quad (4.4)$$

where E_{DC} can be practically estimated for the real and imaginary components in DSP as the mean value of the corresponding components of $E_{rec}(t)$ over a sufficient number of samples.

To include the effects of phase and intensity noises from laser source(s), Eq. (4.1) can be re-written as

$$E(t) = [1 + n_c(t)]E_c e^{j\phi_c(t)} + [1 + n_m(t)]S(t) e^{j\phi_m(t)} e^{j\pi Bt}, \quad (4.5)$$

where $n_c(t)$ and $n_m(t)$ are zero-mean random processes with variances determined by the RIN of the CW carrier and the signal sideband, respectively, and $\phi_c(t)$ and $\phi_m(t)$ are their phase noise components. In this case, the carrier-signal beat term (third term in Eq. (4.2)) can be expressed as

$$\begin{aligned} & [1 + n_c(t)]E_c e^{-j\phi_c(t)} \cdot [1 + n_m(t)]S(t) e^{j\phi_m(t)} e^{j\pi Bt} \\ & \approx E_c S(t) e^{j[\phi_m(t) - \phi_c(t) + \pi Bt]} + [n_c(t) + n_m(t)]E_c S(t) e^{j[\phi_m(t) - \phi_c(t) + \pi Bt]} \end{aligned} \quad (4.6)$$

Following the KK reconstruction procedure in Eqs. (4.3) and (4.4), the recovered baseband signal can be expressed as

$$S_{rec}(t) = S(t) e^{j[\phi_m(t) - \phi_c(t)]} + [n_c(t) + n_m(t)]S(t) e^{j[\phi_m(t) - \phi_c(t)]} + n'_c(t) e^{j\phi'_c(t)} \quad (4.7)$$

where the first term shows that the effective phase noise in the received signal is the *differential phase noise* (DPN) between the CW tone and the signal sideband $[\phi_m(t) - \phi_c(t)]$, the second term represents the effects of carriers' intensity noises on the received signal. The third term represents the noise imposed on the received signal through the imperfect KK field reconstruction.

This is because the first term of $i(t)$ in Eq. (4.2) is no longer a simple DC term; instead, it includes a noise component that will result in both phase, $n'_c(t)$, and intensity, $\phi'_c(t)$, fluctuations affecting the baseband constellation points after KK field reconstruction. It is evident from Eqs. (4.3) & (4.6) that the noise parameters n'_c and ϕ'_c will have variances proportional to the variance of $n_c(t)$. The second term in Eq. (4.7) shows that the RINs of the CW tone and the signal sideband have equal contributions to transmission performance degradation. However, the RIN of the CW tone ($n_c(t)$) usually has stronger impact in the transmission performance than that of the optical carrier used for SSB modulation ($n_m(t)$) (see Eq. (4.6)). This is a consequence of using high CSPR (which is usually ≥ 6 dB) to satisfy the minimum phase condition for conventional QAM signals. The analytical model presented above is derived for the back-to-back configuration with a purpose to show the impact of laser noises on the quality of the recovered signal with the KK detection. As the proposed system is based on QD-MLLs, which are known to have higher phase and intensity noises compared to typical ECL and DFB lasers, the impact of laser phase noise and intensity noise is the main focus of this section. A general analytical model for KK systems including the effects of phase-to-amplitude noise conversion through fiber chromatic dispersion and equalization-enhanced phase noise can be found in [121]. Nonetheless, noise contributions from these effects can also be mapped into the general noise term (third term) in Eq. (4.7) in the model presented here.

4.2.2 The Proposed SSB Superchannel Generation Scheme

The schematic diagram of the proposed superchannel transmitter based on QD-MLL as the light source is shown in Fig. 4.1. A QD-MLL generates a large number of equally-spaced spectral lines, known as a frequency comb, with a free-spectral range (FSR) ΔF . The QD-MLL is selected as the comb source for this system for its higher energy efficiency compared to four-wave-mixing-based

ring resonator comb sources [122]; and its practical frequency spacing, compared to passively mode-locked fiber lasers [123].

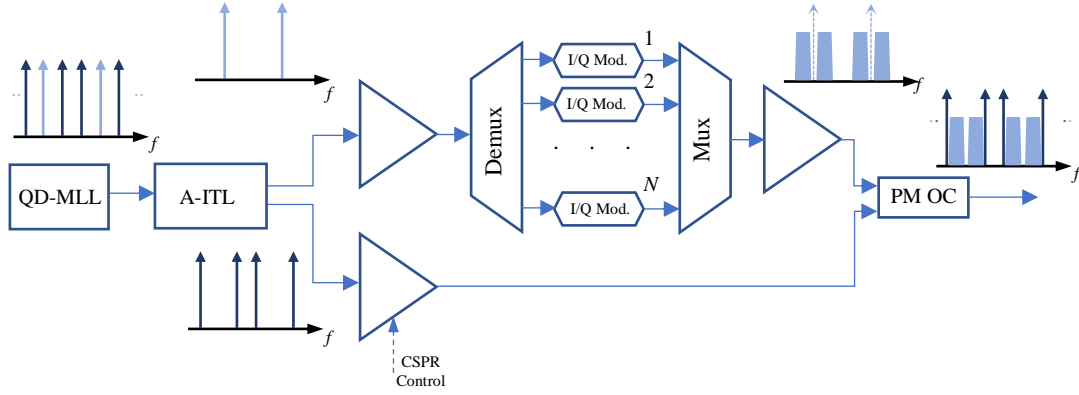


Fig. 4.1. Schematic of the proposed SSB superchannel transmitter. A-ITL: asymmetric interleaver. PM OC: polarization-maintaining optical combiner. Amp: optical amplifier.

In the proposed system, the output of QD-MLL is first fed to an optical asymmetric interleaver (A-ITL) [124-126] with an FSR of $3\Delta F$ and 30%/70% frequency band assignments for the odd and even channels as illustrated in Fig.4.2, where $\Delta F = 25$ GHz is assumed. The “30% port” of the interleaver selects spectral lines spaced by $3\Delta F$, and the “70% port” selects pairs of adjacent spectral lines spaced by ΔF . The spacing between the closest lines of two neighboring pairs is $2\Delta F$. As shown in the insets of Fig. 4.1, the $3\Delta F$ -spaced line pairs are amplified and demultiplexed for data modulation. Every demultiplexed carrier is modulated with two Nyquist SCM channels, one on each side of the optical carrier, through an optical I/Q modulator. These two subcarrier-modulated sidebands can carry independent Nyquist QAM signals multiplexed in the transmitter DSP, so that the I and Q RF signals driving each modulator contain data of two independent SCM channels. The modulator must be biased at the null point so that the optical carrier is suppressed, as shown in the inset of Fig. 4.1, where the suppressed carriers after optical modulation are shown as dashed arrows for the purpose of illustration. After multiplexing and amplifying the modulated channels, the CW pairs from the “70% port” output of the A-ITL are

amplified and re-combined with the modulated signals. The CSPR can be simultaneously set for all channels by controlling the gain of the optical amplifier for the CW tones. It is of high importance to ensure that the modulated optical signals and the CW tones are co-polarized when they combine. One way to ensure this is to use polarization maintaining optical connections and components in the transmitter. The optical amplifiers in this transmitter can be in the form of semiconductor optical amplifiers (SOAs). With the recent advances in photonics integration, this transmitter structure may be realized in an integrated planar lightwave circuit (PLC), allowing for small footprint and low cost [127-130].

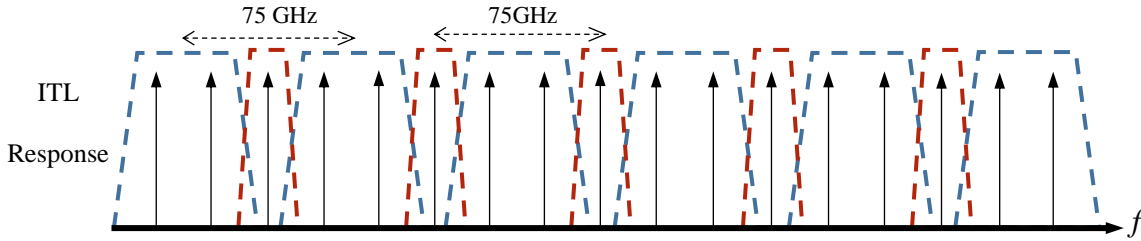


Fig. 4.2. Ideal transfer function of the 37.5GHz-75GHz asymmetric (30%/70%) de-interleaver used to separate comb lines.

The asymmetric channel configuration of the resulting superchannel uses N I/Q modulators to support $2N$ independent data channels, and the frequency spacing between adjacent channel pairs is ΔF . This provides relaxed requirements on the optical filters used to select individual channels at the receiver. A similar channel plan was proposed in [131], where, in contrast to our proposed system, each WDM channel was generated individually using a dedicated laser source and an I/Q modulator. For a conventional WDM frequency grid with equal channel spacing filled by the SSB modulated signal on one side of each CW carrier, spectral components of adjacent channel can create significant crosstalk if the optical filter is not sharp enough. For the superchannel frequency arrangement in the proposed system in Fig. 4.1, however, spectral guard band (ΔF) reserved between each pair of channels (25 GHz in this example) helps relaxing the spectral selectivity

requirements of receiver optical filters. Crosstalk from the nearest channel (see Fig. 4.5(a)) only creates high frequency components ($>\Delta F$) when mixing with the CW carrier, which does not affect the SSB condition. Therefore, only a very small guard band can be sufficient between the two channels in a pair to avoid their interference, which compensates for the relatively wide gap ΔF between channel pairs and results in an overall superchannel noncoded spectral efficiency of $\frac{2}{3}\eta \log_2(M)$ b/s/Hz, where η is the system baud to ΔF ratio, and M is the QAM modulation order. Furthermore, with this channel allocation grid channel selection at the receiver may be done by using de-interleavers with offset center frequencies and equal FSRs followed by conventional low-cost arrayed waveguide grating (AWG) filters, as was proposed in [56,131].

4.3 Experimental Setup and QD-MLL Characterization

To demonstrate the practicality of adopting the QD-MLL comb sources in the transmission of a SSB superchannel in the proposed transmitter scheme for KK reception, we first characterize the phase and intensity noise properties of a single-section InAs/InP QD-MLL with 25 GHz FSR. The driving current of the laser was set to 400 mA at an operating temperature of 19 °C. This MLL operates in the lower half of the C-band with a 3-dB spectral bandwidth of 1.35 THz in the wavelength range of 1532.0-1542.5 nm, consisting of 54 equally spaced spectral lines with 25 GHz channel spacing. The optical spectrum of the laser output is shown in Fig. 4.4(a), which was measured by an OSA with 0.01 nm RBW. To characterize the phase and intensity noises of individual spectral lines, a coherent I/Q receiver was employed with a tunable ECL as the LO, which has a FWHM linewidth of <50 kHz. A 1-nm tunable optical band-pass filter was used to select a set of comb lines with the state of polarization aligned to that of the LO through a polarization controller to maximize the mixing efficiency. The complex beat tones between the

LO and the nearest two comb lines of the QD-MLL were recorded using a digital storage oscilloscope operating at 50 GS/s with 23 GHz of analog bandwidth. The measured electrical SNR after sampling was 57 dB in a resolution bandwidth of 50 kHz. The recorded waveforms were processed offline for evaluating the phase and intensity noises of the comb lines. Optical transmission system performance was then evaluated numerically using the measured complex field of the MLL comb lines as the optical sources. Schematic diagrams of the experimental and simulation setups of this work are shown in Fig. 4.3.

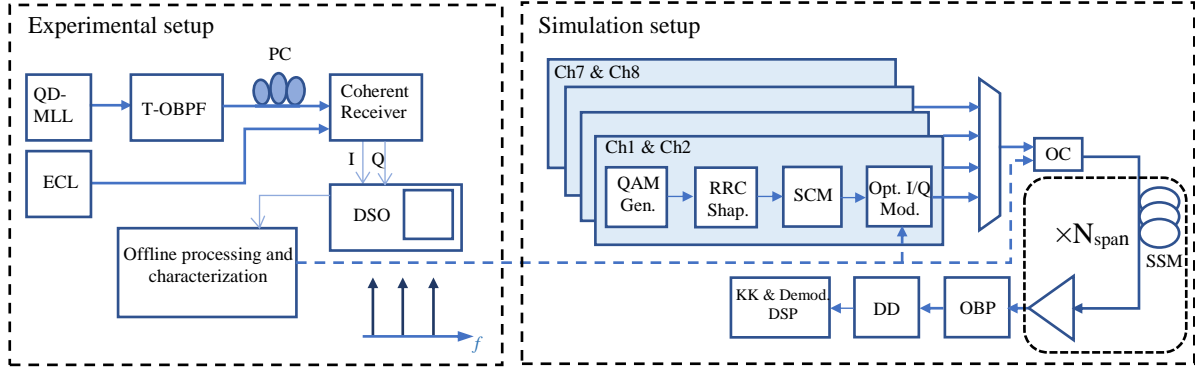


Fig. 4.3. Experimental and simulation setup schematics. T-OBPF: tunable optical bandpass filter. PC: polarization control. ECL: external cavity laser. DSO: digital storage oscilloscope. RRC: root-raised cosine. SCM: sub-carrier modulation. OC: optical combiner. DD: direct detection.

In the process of characterizing phase noise and RIN of QD-MLL comb lines, the recorded coherent detection waveforms were used, which represent a downshifted version of the complex optical field of QD-MLL spectral lines into the RF domain. An ideal BPF with 2 GHz bandwidth was applied to select the spectral line under consideration and limit the broadband receiver noise. For phase noise measurement, the linewidth of each selected comb line was calculated from the variance of the phase difference between field samples spaced at $\tau = 10$ ns as $\Delta\nu = \sigma^2 / (2\pi\tau)$, where σ^2 is the variance of the phase difference sequence. As shown in Fig. 4.4(a), the linewidths were found to vary between 0.9 MHz and 4.5 MHz within the spectral window of the QD-MLL depending on the wavelength, similar to what was found in [78,107] for the same type of MLLs.

The spectra of two adjacent spectral lines are shown in Fig. 4.4(b) which can be best fitted by the Lorentzian function with 2 MHz FWHM linewidth. Also shown in the same figure is the spectrum of the differential phase between these two comb lines, which was obtained by multiplying one of the tones with the complex conjugate of the other in the time domain. The differential phase was found to have a variance equivalent to 300 kHz of FWHM Lorentzian linewidth. Note that the accuracy of determining the differential phase noise is not affected by the linewidth of the LO as it is common for both spectral lines. Fig. 4.4(c) shows the measured RIN spectral profiles of four comb lines, obtained by extracting the perturbations in the magnitude of the field envelope through time averaging and mean subtraction. Unlike the case of the phase noise, comb lines of different wavelengths have very similar RIN characteristics with a higher spectral density at the low frequency region extending to 1 GHz. No correlation was found between intensity noises of adjacent comb lines.

The small differential phase noise between adjacent comb lines is a key feature of QD-MLL sources that makes them suitable for the proposed scheme in this work. As was shown in Sec. 4.2.1, the effective phase noise in KK transmission is determined by the phase difference between the modulated signal sidebands and the CW tone. Therefore, despite the relatively broad linewidths of individual spectral lines, QD-MLL sources are expected to perform well in this transmission scheme. To verify this property, the measured optical fields of two adjacent comb lines (1532 and 1532.2 nm) both with linewidths of approximately 4.5 MHz were used in the simulation to generate one SSB channel of 23 GBd 16-QAM signal together with the required CW tone for KK detection in a back-to-back configuration. Figure 4.4(d) shows the OSNR penalty calculated at the BER level of 10^{-4} after noise loading compared to the ideal case in the absence of phase noise. Details of the simulation procedure are provided in the next section. As shown in Fig.

4.4(d), the QD-MLL exhibits a very small penalty (<0.1 dB) compared to the case of using independent lasers. In this simulation, the phase noise in the case of independent lasers was generated as a Wiener process with variance of $\sigma^2 = 2\pi\Delta\nu T_s$, where T_s is the sampling (symbol) period. Equal linewidths for the modulated signal and the CW tone were assumed for every point in Fig. 4.4(d).

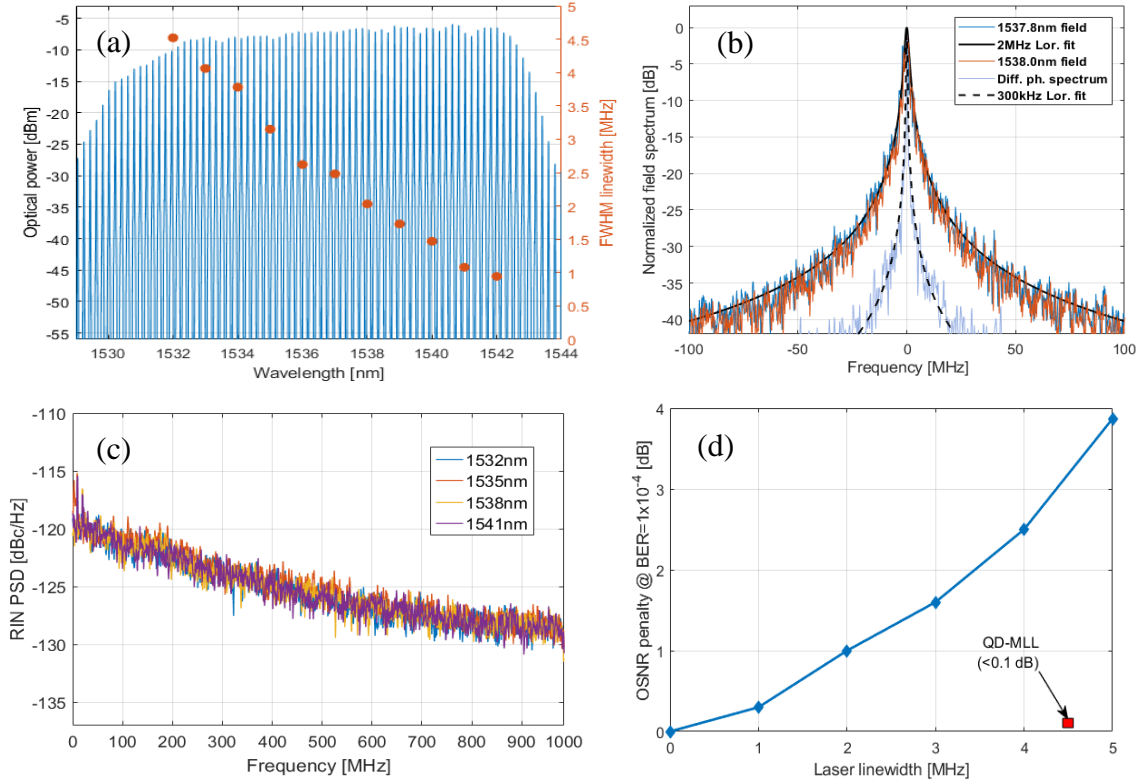


Fig. 4.4. (a) Optical spectrum of the 25GHz QD-MLL and linewidth of some selected comb lines, (b) field spectra of two adjacent comb lines from the middle of the comb band with a Lorentzian fitting corresponding to their average linewidth, and their differential phase spectrum, (c) RIN spectral profiles of some selected wavelengths, and (d) simulated OSNR penalty from laser phase noise in 23 GBd 16-QAM KK transmission using the QD-MLL measured phase noise waveforms, compared to using independent lasers with different linewidths.

Systems of relatively low baud rates are more susceptible to laser phase noise; and maintaining a low phase noise is important to limit phase noise penalty [4]. Lasers with very low phase noise are usually of high cost, that might exceed the feasible system design budget for applications such as access and mobile backhauling networks. It is worth mentioning that the

phase-noise-induced system penalty after fiber transmission is not only limited to the penalties presented in Fig. 4.4(d), but will also include SNR penalties from phase-to-amplitude conversion and equalization-enhanced effects [121], which will inherently be included in the numerical simulations presented in Sec. 4.4.

4.4 System Performance Semi-Numerical Simulation Results

In the QD-MLL characterization, the captured complex waveforms from the coherent I/Q receiver preserve the full information of the phase and intensity noises. As the complex optical fields of adjacent optical spectral lines are captured simultaneously, their phase relation is also captured. Therefore, they can be used for accurate transmission performance evaluation through computer simulation with practical system parameters and numerical models implemented in MATLAB. The block diagram of simulation setup is shown in Fig. 4.3. Eight independent 16-QAM data channels were generated at 23 GBd from random binary data sets, up-sampled and Nyquist-pulse-shaped by a root-raised cosine (RRC) filter with a roll-off factor of 0.05. The binary data were differentially mapped into the 16-QAM constellation points, where the first two bits in a nibble were used to differentially determine the quadrant with Gray coding, and the other two bits were used to determine the symbol in that assigned quadrant [4]. Next, four SCM channel pairs were formed, each pair consists of two data channels of ~ 23 GHz bandwidth, and they are mixed with subcarriers at ± 13.25 GHz, so that the spacing between them is ~ 3.5 GHz. The four pairs of data channels were complex I/Q modulated into optical domain with different quasi-optical carrier frequencies spaced by 75 GHz ($3\Delta F$) as shown in Fig. 4.5(a). The DACs were assumed to have a frequency-independent resolution of 8 bits throughout the simulation steps. The captured complex optical field containing two adjacent comb lines of the QD-MLL were demultiplexed, normalized, and resampled to match the simulation sampling rate. One of them was used to carry Ch5 and Ch6,

and the other one on the left edge of Ch5 is used as the CW tone for KK detection of Ch5. Optical carriers of all other channels, as crosstalk channels, are ideal without noise. This results in a 250 MHz of guard-band between the Nyquist channel and its corresponding CW tone in the optical domain, and a value of $\eta = 0.92$. The overall superchannel noncoded spectral efficiency is 2.45 b/s/Hz ($8 \text{ channels} \times 23 \text{ GBd} \times 4 \text{ bits} / 300 \text{ GHz} = \frac{2}{3}\eta\log_2(M)$, $\eta = 0.92$, $M = 16$) with total superchannel noncoded (line) transmission rate of 736 Gb/s.

For KK detection, the receiver simulation uses a 3rd order super-Gaussian bandpass filter with 35 GHz bandwidth, which is centered at 10.35 GHz ($0.45 \times \text{baud}$) from the CW tone of Ch5 (shown in purple dashed line in Fig. 4.5(a)) to represent a WDM demultiplexer. This is followed by an ideal PD [132] and an ADC of 8-bit resolution. After the ADC, the KK field reconstruction (Eqs. (4.3)) was implemented at a sampling rate of 6 Sam/Sym, followed by down-sampling to 2 Sam/Sym, DC removal and frequency down-conversion (Eq. (4.4)). EDC is then applied, in case of fiber transmission, and the signal is sent to demodulation DSP. The demodulation DSP comprises a matched RRC filter followed by a feed-forward blind equalizer for sample re-timing and signal quality improvement, carrier phase recovery based on constellation partitioning and the 4th power algorithm [70], and a hard-decision symbol-to-bit differential de-mapping.

System performance was first tested in back-to-back configuration with noise loading. The BER was calculated by error counting for different values of CSPR by changing the power of added noise to vary the OSNR. At least 2 million symbols (8 million bits) were transmitted for every BER point for all the results presented in this work. The OSNR is defined here as the power ratio of the SSB modulated signal without the CW tone to the power of ASE noise in a 0.1 nm bandwidth. Figure 4.5(b) shows that with CSPR of $< 6 \text{ dB}$, the transceiver performance is degraded with BER floors at high OSNR values because the minimum phase condition is not satisfied. On

the other hand, increasing the CSPR beyond 8 dB, the performance also deteriorates as shown in dashed-curves in Fig. 4.5(b). This is attributed to the strong beating between the CW tone and the ASE noise at the opposite side of the carrier, which violates the SSB condition. With higher CSPR values ≥ 13 dB, the BER performance could not achieve the 7% HD-FEC conventional threshold of 3.8×10^{-3} even for high OSNR values of up to 32 dB (shown in dashed-dotted curves in Fig. 4.5(b)). Comparing the BER performances corresponding to CSPR of 6 and 7 dB, one finds that they exhibit optimality in different regions of OSNR values. This would suggest that CSPR should be optimized for the specific OSNR of the system to achieve the optimum performance. However, the difference in BERs is very small for a wide range of OSNRs (22~28 dB) achieving BER performance above the FEC threshold; and choosing a fixed CSPR value at the system design stage would achieve acceptable performance without the complexity of required Rx-to-Tx feedback control loop. Figure 4.5(c) shows the required OSNR at the HD-FEC threshold for different values of CSPR. The optimum CSPR value was found to be at 6 dB. All CSPR values below 6 dB violate the minimum phase condition. CSPR values of higher than 6 dB will introduce linear degradation due to the high-power of CW tone which mixes with the ASE noise on both sides of the spectrum around the CW tone. It is also clear that the required OSNR varies only for less than 0.5 dB for CSPRs spanning the range from 5 to 8 dB.

To simulate system performance with fiber transmission, the superchannel was sent through a fiber link consisting of 1, 2, or 3 spans, each of 80 km of SSMF with a dispersion parameter $D=17$ ps/nm/km, a nonlinear parameter $\gamma=1.2$ W⁻¹.km⁻¹, and a loss factor of 0.2 dB/km. Each fiber span is followed by an EDFA with 5 dB noise figure, and the total single span loss was assumed to be of 20 dB to account for splice and connector losses in an actual fiber link. The

symmetric split-step Fourier method was used to simulate signal propagation, so that both dispersion and Kerr nonlinearity impairments are included in the results presented here.

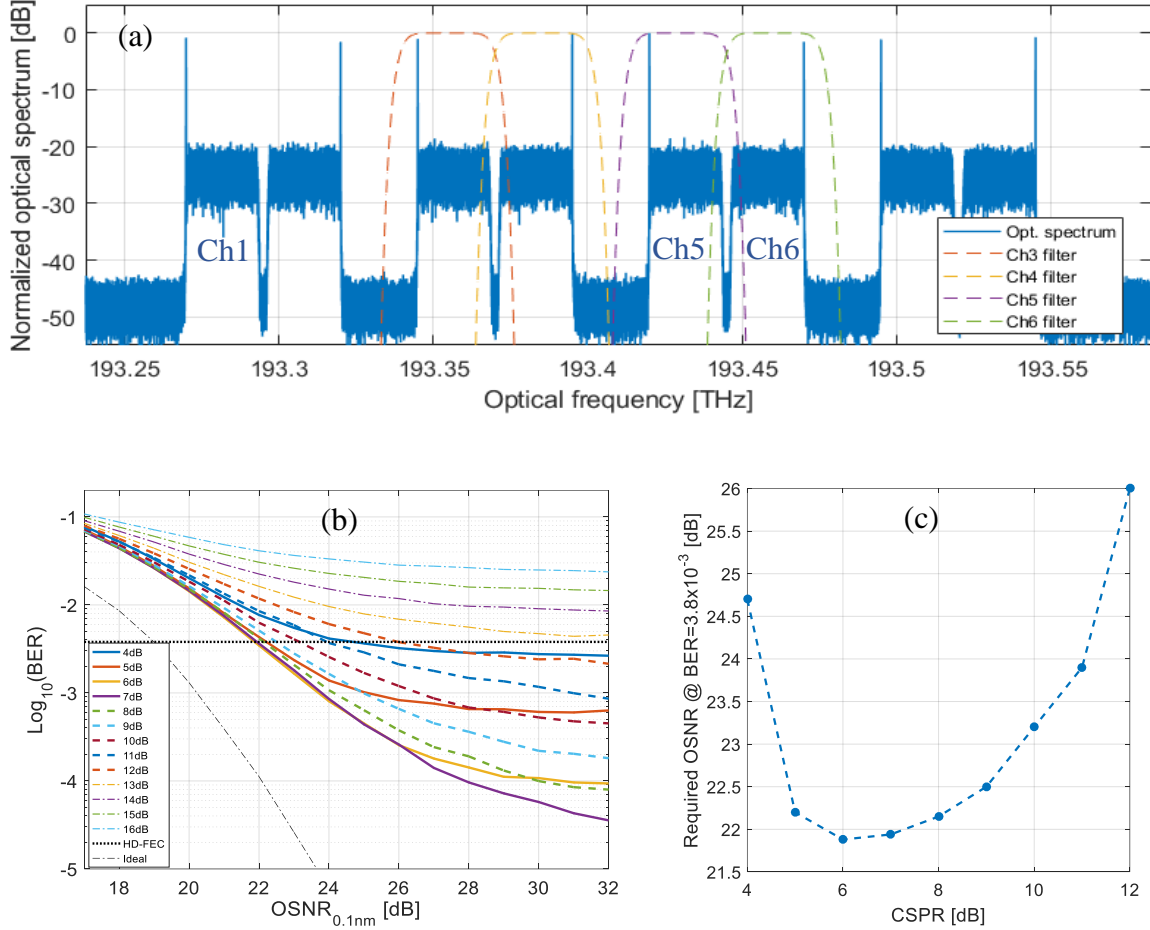


Fig. 4.5. (a) Spectrum of the generated optical superchannel in simulation, (b) B2B BER performance versus OSNR for different values of CSRs, and (c) required OSNR at the 7% HD-FEC threshold (3.8×10^{-3}) for different CSRs values. Dotted-dashed line shown in (b) represents system performance with ideal optical and electrical components at 7-dB CSR.

Figure 4.6(a) shows the BER versus the CSRs values for different number of spans in the fiber link. These BER values were calculated at the optimum launch power per channel including both the signal sideband and CW tone. The optimum CSR value is clearly different from what was found in the back-to-back configuration. In comparison, one finds that this optimum CSR value is about ~2 dB less than what is found in other works (like in [54] or [133], for instance), which is attributed to the high RIN in the CW tone used in our work, as was discussed in Sec.

4.2.1. Nonetheless, the system still achieves BER values below the HD-FEC threshold for the 240 km link over >4 dB window of CSPRs. Figure 4.6(b) shows the dependence of system performance on the launched optical power per WDM channel for the 240 km link. The optimum launched power is found to increase with the increase of the CSPR value. For the optimum CSPR of 8 dB, the optimum power was found to be at 0 dBm. For all 3 CSPR values used in Fig. 4.6(b), varying the launched power for ± 4 dB from the optimum value still keeps the BER value below the HD-FEC threshold.

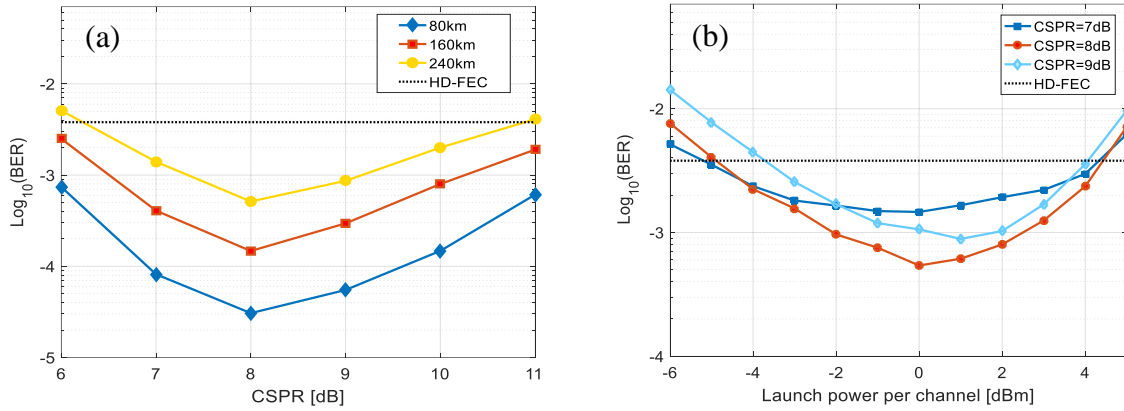


Fig. 4.6. (a) BER versus CSPR at optimum launch power values for different link lengths, and (b) BER versus launch optical power per channel for 3 spans (240 km) at different values of CSPR.

The KK algorithm is known to require an oversampling ratio higher than the typical 2 Sam/Sym due to the broadening of the spectrum caused by the nonlinear logarithm operation, which increases DSP complexity and energy consumption. Some alternative schemes of implementing the KK algorithm were proposed to avoid the logarithm operation, but they still require repetitive or additional operations that add their own computational complexities [28,58]. This oversampling requirement is of high importance in energy-sensitive applications such as DCI. Figure 4.7(a) shows the dependence of receiver BER on oversampling used in the implementation of the KK algorithm in our simulation. The results indicate that an oversampling ratio of 4 Sam/Sym can still achieve acceptable performance with a small BER penalty compared to 6

Sam/Sym for the proposed system with QD-MLL as the optical source. The selection of the KK algorithm implementation scheme in system design will depend on the symbol rate, energy consumption constraints, and the power/OSNR budget of the application.

Finally, the sensitivity to the center frequency drift of the optical filter at the receiver is investigated by changing the center frequency of the 35 GHz super-Gaussian filter with the orders of 3 and 7. The OSNR penalties for $\text{BER}=10^{-3}$ are shown in Fig. 4.7(b). The asymmetry of the penalty with respect to the direction of filter drifting can be explained as follows. Consider Ch5 in Fig.4.5(a), when the bandpass filter shifts to a higher frequency, less amount of ASE noise on the left side of the CW tone is selected, which improves the performance as long as the drift is small enough and the CW tone is not attenuated. Once the positive drift significantly attenuates the CW tone, system performance degrades rapidly. On the other hand, for the filter drifting to the lower frequency, the cutoff of the continuous signal spectrum is gradual, so is the performance degradation. It is also shown in Fig. 4.7(b) that the quality (steepness) of the filter does not improve the performance tolerance to negative frequency drift if the filter is centered at the same frequency relative to the data spectrum. Therefore, the choice of filter center frequency should be optimized for different filter transfer functions and drifting tolerances. It is worth mentioning that as the frequency drifting is relative between the filter and the laser, the penalty caused by QD-MLL frequency drift is also predicted by Fig. 4.7(b). In general, frequency drifts of QD-MLL affect all comb lines equally with little change in the frequency spacing. For instance, in the QD-MLL used in our experimental work the differential frequency drift between adjacent comb lines was only in the order of a few MHz for the common-mode frequency drift of multiple GHz due to temperature changes. This small differential frequency drift can be easily eliminated in receiver DSP by a frequency offset compensation algorithm.

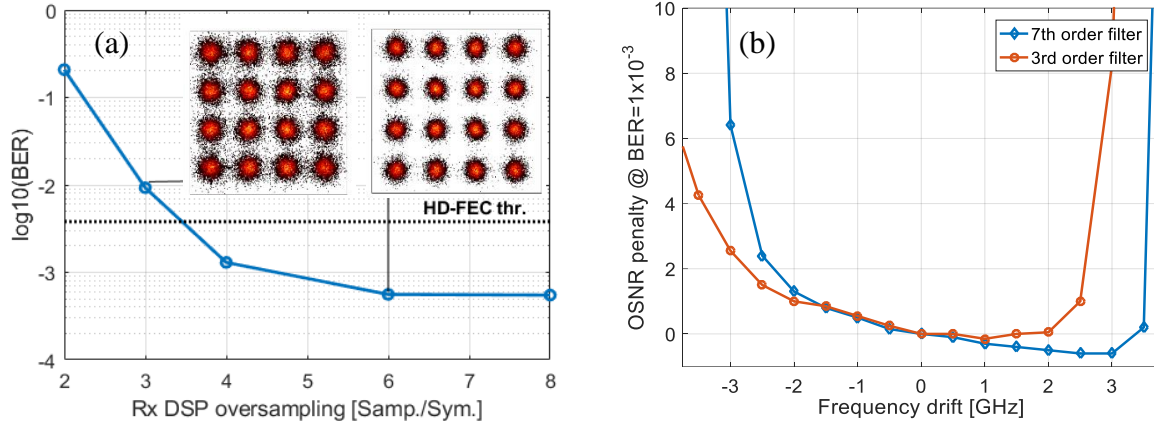


Fig. 4.7. (a) BER versus KK oversampling ratio for 240 km with optimum CSPR (8 dB) and launch power (0 dBm), and (b) OSNR penalty [dB] at $\text{BER}=10^{-3}$ versus receiver optical filter frequency drift for 3rd and 7th order super-Gaussian filter response in B2B configuration with noise loading. EVM values of constellations in insets of (a) are 10.8% and 14.9% for 6 Sam/Sym and 3 Sam/Sym, respectively.

4.5 Conclusions

In this work we have proposed a low-complexity and cost-effective scheme for generating a superchannel of SSB modulation based on a single QD-MLL optical source. By utilizing the mutual coherence between adjacent comb lines, the proposed system has been shown through experimental measurement of a QD-MLL and numerical simulations to exhibit good system performance despite the relatively-high individual linewidths and RIN of QD-MLL comb lines. The system was shown to perform below the HD-FEC threshold for up to 3 spans of SSMF extending up to 240 km with 16-QAM Nyquist-SCM channels, achieving an overall superchannel line spectral efficiency of 2.45 b/s/Hz. Compared to conventional systems of generating WDM SSB channels based on multiple laser sources, our proposed system simultaneously provides optimum utilization of DAC bit resolution and analog bandwidth of DAC and optical I/Q modulators without the need for additional RF or optical components to achieve this result. Furthermore, the adoption of QD-MLL together with the dual channel modulation technique in the proposed system reduce the cost and footprint of the system by using half the number of DACs

and I/Q modulators compared to those required in conventional multichannel generation systems, hence provide higher energy efficiency. With the recent advances of integrated photonics and electro-optic modulators, the transmitter of the proposed system is suitable for integration on PLC platforms.

This page intentionally left blank

Chapter 5

Phase Noise Enhancement in Saturated SOA used for RIN Reduction

This chapter studies the characteristics of relative intensity noise (RIN) reduction and the associated phase noise enhancement of continuous-wave (CW) optical signals passing through a semiconductor optical amplifier (SOA) operating in the saturation regime. We show that although the RIN can be considerably reduced, signal phase noise may be enhanced at the high-frequency region. While this high frequency phase noise enhancement is not shown as an increase of spectral linewidth, it affects system performance when coherent detection is used. System performances of both PAM4 modulation with direct detection and 16-QAM complex modulation with coherent detection have been measured. A single spectral line from a quantum-dot mode-locked laser is used as the light source, which is known to have relatively high RIN (>-120 dB/Hz in the low frequency region). The impacts of using SOA-based RIN reduction in both systems are evaluated experimentally.

5.1 Introduction

Semiconductor optical amplifiers (SOAs) have small size, low power consumption, wide gain bandwidth, and can be integrated in photonic integrated circuits (PIC) [134,135]. SOAs can provide a low-cost alternative to erbium-doped fiber amplifiers (EDFAs) in fiber-optic communication systems [136-139], notably in short reach interconnect applications based on PIC

[140]. SOAs also find use in all-optical signal processing through nonlinear saturation and nonlinear wave mixing [141,142]. Furthermore, the reduction of relative intensity noise (RIN) of unmodulated continuous wave (CW) optical signals has been demonstrated when the signal passes through a saturated SOA [143-145]. Recently, multi-wavelength optical sources such as quantum-dot(dash) mode-locked lasers (QD-MLLs) have been studied in WDM and multi-lane interconnect applications [93,140,144-145]. Each spectral line of a QD-MLL usually has relatively low power and high RIN on the order of -120 dB/Hz in the low frequency region of up to 100MHz. An SOA can provide power amplification and RIN reduction. SOA-based RIN reduction also has lower complexity compared to other techniques based on, e.g., injection locking [146].

RIN affects the performance of IMDD systems, often used in short-reach and optical interconnection applications. RIN may also have strong impact in coherent systems. For coherent systems, although the effect of RIN from the LO can be greatly reduced using balanced photodiode PD detection given high enough common-mode rejection ratio [147], the transmitter side laser RIN can limit the transmission performance, especially when high modulation orders of QAM are employed. RIN also has a direct impact in self-coherent systems with single PD detection [93]. In order to adopt potentially low-cost and small-footprint lasers, such as multi-wavelength QD-MLL with relatively high RIN, better understanding of RIN reduction through SOA is important.

In this work, we show that although a saturated SOA can effectively reduce the RIN of a CW optical signal, it introduces the enhancement of high-frequency phase noise, which impairs system performance when QAM coherent detection is used. Interestingly, this phase noise enhancement has minimal effect on the measured linewidth of the CW signal after the SOA. This is because spectral linewidth is primarily determined by the low frequency components of phase noise. High frequency phase noise measurement must be used to assess the amount of the phase

noise enhancement. To our best knowledge, this non-linewidth-broadening effect has not been reported elsewhere in the literature. We first demonstrate the effect by numerical simulations, and then we report the measured phase noise and intensity noise properties of a CW signal from a QD-MLL before and after passing through a saturated SOA. Then we report results of back-to-back transmission experiments using both IMDD and intradyne coherent detection, with and without an SOA, to assess its impact in the transmission performance of these two types of systems.

5.2 Device Modeling and Simulations

We modeled RIN reduction and the associated phase noise enhancement caused by a saturated SOA. We carried out simulations using numerically-generated CW optical signal with RIN and phase noise, and passed this signal through an SOA model. The nonlinear characteristics and the gain dynamics of the SOA were modeled by the differential equation [148]:

$$\left(1 + \tau_c \frac{d}{dt}\right) h(t) = h_0 - \frac{|E_{in}(t)|^2}{P_{sat}} \{\exp[h(t)] - 1\} \quad (5.1)$$

where $h(t) = \int_0^L g(z, t) dz$ is the power gain integrated along the active length of the device L . $h_0 = \ln G_0$ with G_0 being the small signal gain. τ_c is the carrier lifetime, $E_{in}(t)$ is the input signal complex optical field, and P_{sat} is the saturation output power of the SOA. The complex optical field at the SOA output is given by $E_{out}(t) = E_{in}(t) \exp[(1 - j\alpha)h(t)/2]$, where α is the chirp parameter. P_{sat} and G_0 can be determined in a steady-state measurement by varying the average input power to the SOA and measuring the average output power. τ_c and α can be determined dynamically by measuring and comparing signal waveforms at the input and output of the SOA. A standard 4th-order Runge-Kutta method was used to numerically solve Eq. (5.1) [149]. In our simulations, we used the measured parameter values of the SOA, that is used in our experimental work presented in the next section, as listed in Table 5.1.

Table 5.1. Measured parameters of the SOA device.

Parameter	Quantity	Measured Value
G_0	Small signal gain	16 dB
τ_c	Carrier lifetime	300 ps
P_{sat}	Saturation power	5 dBm
α	Chirp parameter	5

The optical signal input to the SOA was created at 50 GS/s with 5 million points and a RIN of -125 dB/Hz. The phase noise was modeled as a Wiener process with a 3-dB FWHM Lorentzian linewidth of 1 MHz, and the intensity noise was also assumed to be white-Gaussian. It should be noted that these assumptions for the optical signal are for the purpose of showing the impact of the saturated SOA, and the actual phase and intensity noises of the laser signal used for the experiments have non-white spectra as will be shown in the next section. The input power to the SOA was set to -20 dBm and 0 dBm, for the linear and saturated regimes, respectively. Figure 5.1(a) shows the RIN of the signal before and after passing through the SOA. As expected, the RIN does not experience a significant change when the SOA operates in the linear regime. Whereas in the saturated regime the RIN is clearly reduced by approximately 7 dB for frequencies lower than the cutoff frequency determined by [143]

$$f_c = \frac{1}{2\pi\tau_c} \sqrt{G_{cw}^2 b^2 + 2G_{cw}b - 2b^2 - 4b - 1}, \quad b = \frac{\ln(G_0/G_{cw})}{G_{cw} - 1} \quad (5.2)$$

where G_{cw} is the saturated power gain. RIN levels at frequencies higher than f_c remain unaffected. This stems from the high-pass characteristic of the saturated SOA [143,145] and it shows the importance of the carrier lifetime and the saturation depth in determining the RIN reduction efficiency. G_{cw} was found to be equal to 8.2 dB in our simulation at the input power of 0 dBm, resulting in $f_c=1.32$ GHz.

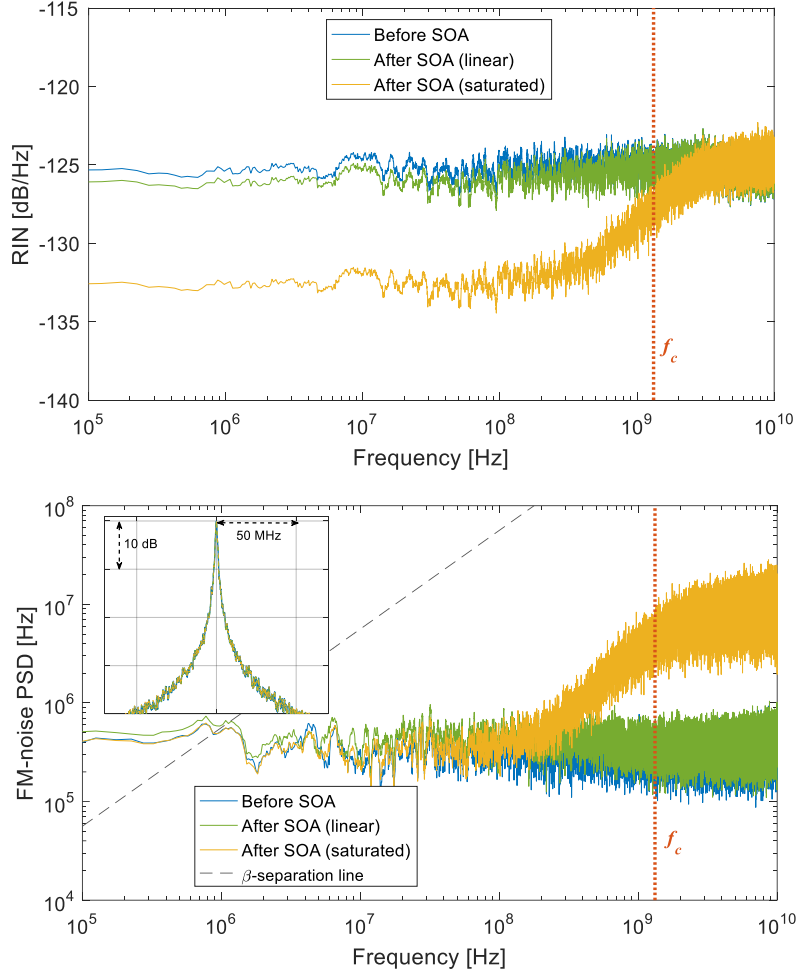


Fig. 5.1. Simulation results for (upper) RIN and (lower) FM-noise PSD before and after passing through SOA with linear ($P_{in} = -20$ dBm) and saturated ($P_{in} = 0$ dBm) operation regimes. The inset in displays the corresponding field spectra, showing no any enhancement to the linewidth.

The RIN of the optical signal introduces carrier density modulation of the SOA which results in a modulation of the refractive index, and thus the phase of the optical signal is modulated by the RIN through the chirp of the SOA [135,148]. As the FM noise is often used to describe the spectral properties of the phase noise, the latter can be converted into the FM noise through:

$$S_{FM}(f) = \left| FFT \left[\frac{\Delta\varphi(\tau)}{2\pi\tau} \right] \right|^2 \frac{f^2}{4\sin^2(\pi f\tau)} \quad (5.3)$$

where $\Delta\varphi(\tau)$ is the phase variation of the complex optical field sampled at a time interval τ . Figure 5.1(b) shows the FM-noise PSDs of the same optical signals of Fig. 5.1(a). After passing through

the SOA, the FM noise PSD of the optical signal is the superposition of the original FM noise of the laser source and the extra FM noise generated at the SOA. At low frequencies below f_c , the phase noise PSD is flat due to the low pass characteristic of the carrier density modulation, and thus the SOA-induced FM noise increases as a function of f^2 as indicated by Eq. (5.3). The increase of FM noise as the function of frequency ceases for $f > f_c$, due to the reduced efficiency of carrier density modulation. The example in Fig. 5.1(b) shows that the FM noise generated at the SOA is higher than that of the input signal for frequencies higher than ~ 500 MHz, after which there is an observable ~ 15 dB enhancement, and the FM noise after the SOA is no longer white.

As the FWHM linewidth of an unmodulated optical signal is determined mainly by the low frequency components of the FM noise PSD, typically below the intersection with a so-called *β -separation line* [83], the high-frequency phase noise enhancement does not affect the measurable linewidth of the CW signal. The inset in Fig. 5.1(b) shows the optical field spectra before and after the SOA, and the spectral shape is unaffected by the SOA even for frequencies at which the normalized spectral density is as low as -40 dB. However, a coherent system performance depends heavily on the high frequency components of the FM-noise PSD, and the phase noise of a CW signal with non-white FM noise is better quantified by a *Lorentzian-equivalent linewidth* (LEL) rather than the traditional -3 dB or -20 dB linewidth measures, as was shown in Chapter 2. LEL is determined by the FM noise at a specified sampling frequency. In our simulation, the LEL evaluated at a sampling frequency of 5 GHz was found to be enhanced from 1 MHz to nearly 15 MHz after the saturated SOA. This large enhancement is a result of the assumed white RIN spectrum extending beyond f_c , which may not be realistic for practical lasers. Thus, phase noise enhancement in the high frequency region for practical lasers with lower high-frequency RIN PSDs could be much lower.

5.3 Experimental Setup and Results

The experimental setup used for RIN and phase noise characterization and transmission experiments is shown in Fig. 5.2, where the dashed-outlined blocks are used only for the coherent transmission. We use a single-section InAs/InP QD-MLL [145] operating in the 1550 nm wavelength window as the light source, which has a relatively high RIN (>-120 dB/Hz at the low frequency, and an average RIN [145] of -28.4 dB in the 25kHz-5GHz frequency window). The device temperature was stabilized at 18.5 °C and the bias current was set to 360 mA. This laser simultaneously emits approximately 50 spectral lines with 25 GHz line spacing, and we selected a single spectral line with two narrowband optical filters at 1537.33nm. The signal is optically amplified to approximately 0 dBm by an EDFA inserted between the two optical filters. Then the optical signal is coupled into an SOA. The SOA is biased at 240 mA injection current, resulting in $G_0=16$ dB small signal gain. With the 0 dBm input power, the SOA operates in the saturation regime. The optical signal before and after the SOA is down-shifted to the RF domain through a phase diversity coherent receiver employing an ECL as the LO with <50 kHz spectral linewidth and <-140 dB/Hz RIN. Thus, the impacts of both phase noise and RIN of the LO on the measurement are negligible compared to those of QD-MLL. The I and Q components of the complex RF signal are captured and stored by a RTSO at 50 GS/s with 2×10^6 sample points (duration of 40 μ s) and processed offline by MATLAB. The optical power input to the coherent receiver was kept constant for all measurements so that the instrumentation noise contribution is equal for all cases. The RIN is obtained by extracting the magnitude perturbations of the complex envelope (after frequency down-shifting to the origin) and calculating the spectrum. Figure 5.3(a) shows the RIN with and without passing through the saturated SOA, with a clear reduction of 6~7

dB at low frequencies, with measured average RIN reduction from -28.4 dB to -35 dB over the frequency range from 25 kHz to 5 GHz.

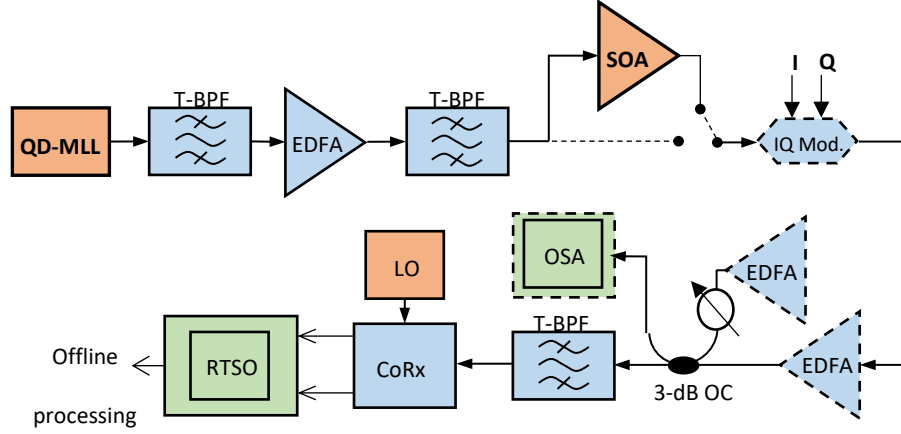


Fig. 5.2. Schematic of the experimental setup used for phase and intensity noise measurements and back-to-back coherent transmission. Dashed-outlined blocks are used only for the coherent transmission setup. QD-MLL: quantum-dot mode-locked laser; T-BPF: tunable bandpass filter; CoRx: coherent receiver; RTSO: real-time sampling oscilloscope.

The measured FM-noise PSDs are shown in Fig. 5.3(b). Note that the QD-MLL inherently has non-white FM noise spectral profile before the SOA (blue), and the high-frequency spectral region near 1 GHz has about a decade lower FM noise PSD compared to that at lower frequencies, as was shown in Chapter 3. FM-noise PSD is enhanced after passing through the SOA (orange) with similar high-pass characteristic explained above in the previous section. The FM-noise PSD enhancement starts to reduce for frequencies higher than 1 GHz due to the reduced high frequency RIN PSD shown in Fig. 5.3(a). The field spectra, displayed in the inset, show only a negligible 8% linewidth enhancement (36 MHz to 39 MHz at -20 dB). On the other hand, the Lorentzian-equivalent linewidth measured at 5 GHz sampling frequency was found to be enhanced by 155% (from 0.95 MHz to 2.43 MHz). As will be shown next, this enhancement will have noticeable performance impact in coherent transmission.

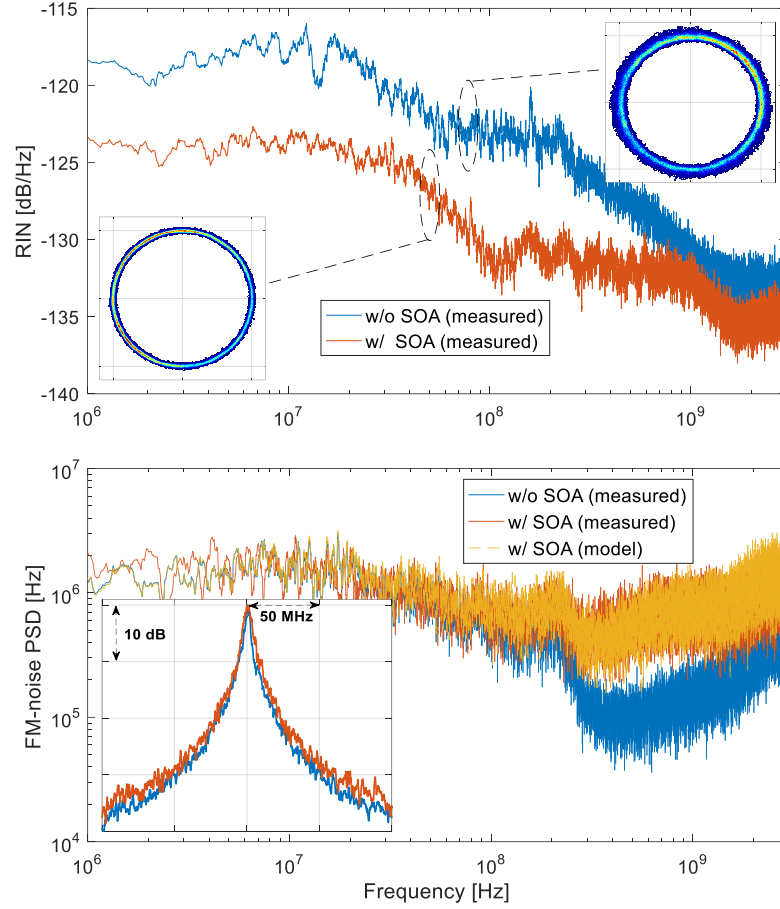


Fig. 5.3. Measured (upper) RIN and (lower) FM-noise PSDs before and after passing through the SOA with saturated ($P_{in} = 0$ dBm) gain. The insets in (a) display the complex-plane scatter plots of the normalized complex envelopes without and with passing through the SOA, within 5 GHz bandwidth. The inset in the lower plot shows the corresponding measured field spectra.

To evaluate the performance of an IMDD system, the CW optical signal, with or without the SOA, is modulated by a LiNbO₃ Mach-Zehnder modulator (MZM) driven by a 10 GBd PAM4 signal from an arbitrary waveform generator (AWG) at 25 GS/s sample rate, followed by a driver amplifier. The setup is shown in Fig. 5.4. The MZM is biased at the quadrature point. The signal from the AWG included raised-cosine pulse shaping, with a roll-off factor of 0.1, and pre-equalization to compensate Tx-Rx frequency roll-off. The optical power of the modulated signal was changed through a variable attenuator before direct detection in a PD. The PD output is captured by the RTSO at 25 GS/s and processed offline with filtering, resampling, symbol-timing

synchronization, and hard-decision symbol-to-bit Gray decoding. Figure 5.5 shows the BER as a function of the received signal power P_{RX} . The receiver sensitivity is improved by >2.5 dB at 10^{-3} BER when the signal passes through the SOA for RIN reduction. While the experimental setup was not calibrated for optimum receiver sensitivity, an ECL with -140dB/Hz RIN is used as the transmitter light source for comparison.

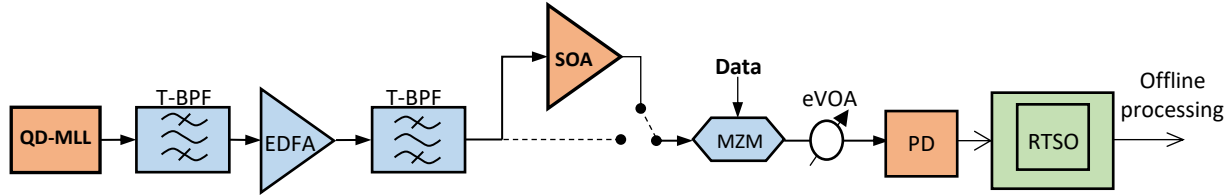


Fig. 5.4. IMDD performance experimental setup.

In the coherent 16-QAM transmission, the I/Q modulator is driven by 5 GBd Nyquist (RRC roll-off of 0.1) signal at 21.4 GS/s. The received signal is digitally captured at 25 GS/s and processed offline. The signal processing included normalization, resampling to 2 Sa/Sy, matched filtering, frame and symbol synchronization, adaptive equalization, carrier phase recovery with the blind phase search (BPS), and symbol-to-bit hard decision for BER calculation. The BPS window half-length was optimized for each case (8 for ECL and 6 for QD-MLL). Despite the RIN reduction, Fig. 5.5 shows that the OSNR performance is degraded by about 1.5 dB at $BER=10^{-3}$ when the signal passes through the SOA. A computer simulation based on the measured CW waveforms reveals that RIN reduction alone would improve the required OSNR by about 0.2 dB, while the enhancement of high-frequency FM noise introduced a 1.7 dB OSNR degradation. This degradation can be more severe if a higher order modulation is used such as 32- or 64-QAM. Nonetheless, the overall effect will depend on the system symbol rate.

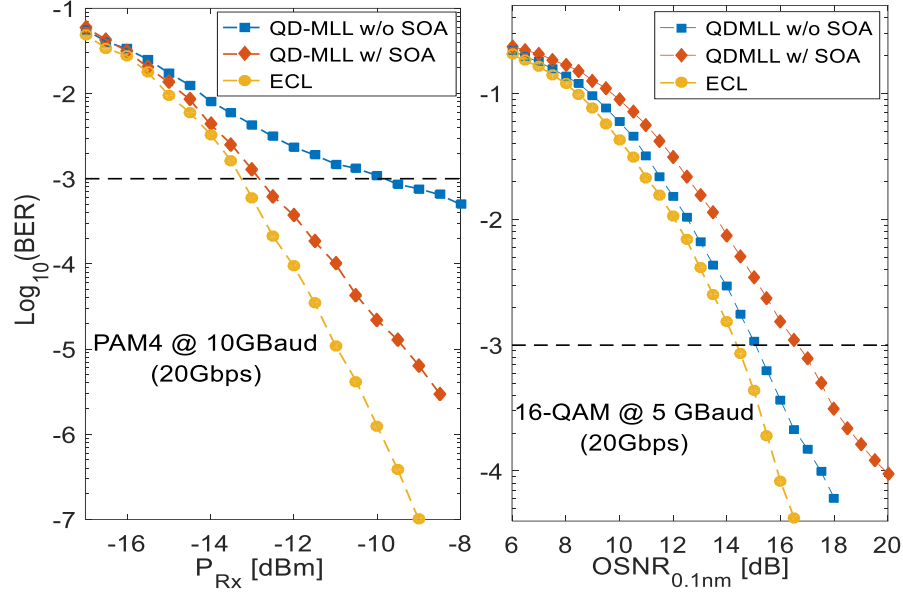


Fig. 5.5. (Left): BER as a function of received optical power for PAM4 at 10 GBd; and (right): BER as a function of OSNR for a 16-QAM coherent link at 5 GBd, both with and without SOA-based RIN reduction. ECL with RIN < -140 dB/Hz was used as the transmitter CW source for comparison.

We perform semi-numerical simulations to investigate the dependence of the overall impact of the opposing results of RIN reduction and phase noise enhancement on the symbol rate and the radial and angular cardinality of the QAM constellations. Figure 5.6 shows the results of simulations of 16- and 64-QAM signals based on using the measured complex waveforms of the beat tone with and without the SOA (shown in Fig. 2(b) & (c)) at different symbol rates. The simulation setup is similar to that shown in Fig. 3.5 in Chapter 3. The results are presented in terms of the difference of the required E_b/N_0 in dB to achieve a threshold BER of 10^{-3} , which shows a performance improvement for the 64-QAM at the symbol rate of 65 GBd despite the enhanced phase noise. This is due to the fact that the enhanced phase noise has slow variations compared to the symbol rate, whereas the intensity noise reduction can significantly introduce performance improvement for the 64-QAM constellation with the high radial cardinality.

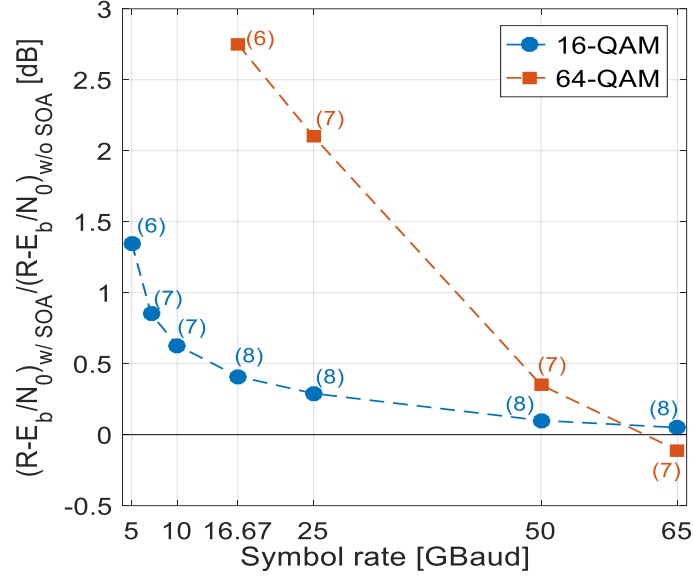


Fig. 5.6. Simulation results of the difference of required E_b/N_0 with and without SOA-based RIN reduction as a function of symbol rate. Parenthetical numbers show the optimum half-window length used in the BPS CPR.

5.4 Conclusion

We have investigated the phase and intensity noise properties of a CW optical signal passing through a saturated SOA. A QD-MLL is used as the laser source which has a relatively high RIN (> -120 dB/Hz) at the low frequency region. We showed that although the signal linewidth remains unchanged, this RIN reduction through the SOA introduces an increase of high-frequency FM noise, which may impact the performance of coherent systems. The performance of the SOA has been analyzed through a rate equation model, and simulated results agree well with the measured FM noise spectra when the signal passes through the SOA. The translation of an optical signal RIN into the increase of high-frequency FM noise is attributed to the RIN-induced carrier density modulation and the chirp effect of the semiconductor material. The performance impact of RIN reduction in an IMDD system, and the high-frequency FM noise increase in a coherent system has been measured experimentally. The trade-off between RIN reduction and high-frequency FM

noise enhancement should be optimized for phase-sensitive transmission applications through the joint design of the SOA and system power budget.

This page intentionally left blank

Chapter 6

Proposed Future Work

The major topics presented in this dissertation studied the most challenging impairment to the implementation of digital coherent receivers at relatively low symbol rates: the phase noise. As the cost effectiveness, energy efficiency, and transmission latency are major concerns in the design of optical interconnection systems, we propose the following research directions as extensions to the current work:

- 1- Investigating and developing hardware-efficient CPR algorithms that exhibit effectiveness in tracking the low-frequency parts of the FM noise to reduce the penalty overhead resulting from these low-frequency perturbations. This could be a combined FOC and CPR algorithm design. Averaging window length adaptation could also be investigated for improved performance. The application of Kalman filters in frequency and phase tracking may be investigated for as well, with a focus on the spectral properties of the tracking mechanism.
- 2- As the *SNR* performance is not the major concern in short-reach applications, we proposed investigating different modulation constellations that may exhibit high resilience to phase noises and require easier CPR algorithms with less DSP efforts.
- 3- As an extension to the work presented in Chapter 4, we propose investigating the implementation of SSB modulation using only analog circuits. This can be implemented by employing true log amplifiers with 90° electrical hybrid couplers to emulate Hilbert

transform required for the SSB modulation, as was done in Ref. [150] but with high-SE modulation formats. At the receiver, the analogue implementation of the KK receiver could also be investigated. True log amplifiers could be built as integrated circuits to help implement the KK phase reconstruction process. The analog implementation at the Tx and Rx side will not only reduce the energy consumption, but also reduces the transmission latency by avoiding the DSP processing delays resulting from the parallelized implementations.

- 4- The opto-electronic analog implementation of KK receivers can also be investigated. The nonlinear functions required for the KK field reconstruction may be implemented in the optical domain. For instance, the log function could be implemented in a nonlinear electro-optic device such as a specifically-designed SOA.

References

- [1] G.709 : Interfaces for the optical transport network. Online link: "<http://www.itu.int/rec/T-REC-G.709/>," The International Telecommunication Union.
- [2] IEEE P802.3cd 50 Gb/s, 100 Gb/s and 200 Gb/s Ethernet Task Force. Online link: "<http://www.ieee802.org/3/cd/baselines/index.html>"
- [3] IEEE P802.3bs 200 Gb/s and 400 Gb/s Ethernet Task Force. Online link: "<http://www.ieee802.org/3/bs/>"
- [4] T. Pfau, S. Hoffmann and R. Noe, "Hardware-Efficient Coherent Digital Receiver Concept with Feedforward Carrier Recovery for M-QAM Constellations," in *Journal of Lightwave Technology*, vol. 27, no. 8, pp. 989-999, Apr. 2009.
- [5] E. Ip and J. M. Kahn, "Feedforward Carrier Recovery for Coherent Optical Communications," in *Journal of Lightwave Technology*, vol. 25, no. 9, pp. 2675-2692, Sept. 2007.
- [6] William Shieh and Keang-Po Ho, "Equalization-enhanced phase noise for coherent-detection systems using electronic digital signal processing," in *Opt. Express*, vol. 16, pp. 15718-15727, 2008.
- [7] K. Fukuchi, T. Kasamatsu, M. Morie, R. Ohhira, T. Ito, K. Sekiya, D. Ogasahara, and T. Ono, "10.92-Tb/s (273 x 40-Gb/s) triple-band/ultra-dense WDM optical-repeated transmission experiment," in *Optical Fiber Communication Conference and International Conference on Quantum Information*, 2001, paper PD24.
- [8] Alan H. Gnauck, R. W. Tkach, A. R. Chraplyvy, and T. Li, "High-Capacity Optical Transmission Systems," in *J. Lightwave Technol.*, vol. 26, pp. 1032-1045, 2008.
- [9] N. S. Bergano, J. Aspell, C. R. Davidson, P. R. Trischitta, B. M. Nyman and F. W. Kerfoot, "Bit error rate measurements of 14000 km 5 Gbit/s fibre-amplifier transmission system using circulating loop," in *Electronics Letters*, vol. 27, no. 21, pp. 1889-1890, 1991.
- [10] R. A. Linke and A. H. Gnauck, "High-capacity coherent lightwave systems," in *Journal of Lightwave Technology*, vol. 6, no. 11, pp. 1750-1769, 1988.
- [11] T. Otani, K. Goto, H. Abe, M. Tanaka, H. Yamamoto and H. Wakabayashi, "5.3 Gbit/s 11300 km data transmission using actual submarine cables and repeaters," in *Electronics Letters*, vol. 31, no. 5, pp. 380-381, 1995.
- [12] T. Tokle, C. R. Davidson, M. Nissov, J. X. Cai, D. Foursa and A. Pilipetskii, "6500 km transmission of RZ-DQPSK WDM signals," in *Electronics Letters*, vol. 40, no. 7, pp. 444-445, 2004.
- [13] R. Griffin and A. C. Carter, "Optical differential quadrature phase-shift key (oDQPSK) for high capacity optical transmission," in *Optical Fiber Communications Conference (OFC)*, 2002, paper WX6.
- [14] Guifang Li, "Recent advances in coherent optical communication," in *Adv. Opt. Photon.*, vol. 1, pp. 279-307, 2009.

- [15] Pak S. Cho *et al.*, "Investigation of 2-b/s/Hz 40-gb/s DWDM transmission over 4×100 km SMF-28 fiber using RZ-DQPSK and polarization multiplexing," *IEEE Photon Technology Letters*, vol. 16, no. 2, pp. 656-658, 2004.
- [16] J. M. Kahn, A. H. Gnauck, J. J. Veselka, S. K. Korotky and B. L. Kasper, "4-Gb/s PSK homodyne transmission system using phase-locked semiconductor lasers," in *IEEE Photonics Technology Letters*, vol. 2, no. 4, pp. 285-287, April 1990.
- [17] M. G. Taylor, "Coherent detection method using DSP for demodulation of signal and subsequent equalization of propagation impairments," in *IEEE Photonics Technology Letters*, vol. 16, no. 2, pp. 674-676, Feb. 2004.
- [18] Yan Han and Guifang Li, "Coherent Optical Communication Using Polarization Multiple-Input-Multiple-Output," in *Opt. Express*, vol. 13, pp. 7527-7534, 2005.
- [19] R. Noe, "PLL-free synchronous QPSK polarization multiplex/diversity receiver concept with digital I&Q baseband processing," in *IEEE Photonics Technology Letters*, vol. 17, no. 4, pp. 887-889, 2005.
- [20] K. Kikuchi, "Phase-diversity homodyne detection of multilevel optical modulation with digital carrier phase estimation," in *IEEE Journal of Selected Topics in Quantum Electronics*, vol. 12, no. 4, pp. 563-570, 2006.
- [21] E. Agrell *et al.*, "Roadmap of optical communications," in *Journal of Optics*, vol. 18, no. 6, May, 2016.
- [22] Peter J. Winzer, David T. Neilson, and Andrew R. Chraplyvy, "Fiber-optic transmission and networking: the previous 20 and the next 20 years [Invited]," in *Opt. Express*, vol. 26, pp. 24190-24239, 2018.
- [23] K. Kikuchi, "Fundamentals of Coherent Optical Fiber Communications," in *Journal of Lightwave Technology*, vol. 34, no. 1, pp. 157-179, 1 2016.
- [24] S. Randel, D. Piliori, S. Chandrasekhar, G. Raybon, and P. Winzer, "100-Gb/s discrete-multitone transmission over 80-km SSMF using single-sideband modulation with novel interference-cancellation scheme," in *Proc. Eur. Conf. Opt. Commun.*, 2015, Paper Mo.4.5.2.
- [25] Z. Li *et al.*, "Two-stage linearization filter for direct-detection subcarrier modulation," in *IEEE Photon. Technol. Lett.*, vol. 28, no. 24, pp. 2838–2841, 2016.
- [26] Z. Li *et al.*, "Reach enhancement for WDM direct-detection subcarrier modulation using low-complexity two-stage signal-signal beat interference cancellation," in *Proc. Eur. Conf. Opt. Commun.*, 2016, Paper M.2.B.1.
- [27] K. Zou, Y. Zhu, F. Zhang, and Z. Chen, "Spectrally efficient terabit optical transmission with Nyquist 64-QAM half-cycle subcarrier modulation and direct-detection," in *Opt. Lett.*, vol. 41, no. 12, pp. 2767–2770, 2016.
- [28] Antonio Mecozzi, Cristian Antonelli, and Mark Shtaif, "Kramers-Kronig coherent receiver," *Optica*, vol. 3, pp. 1220-1227, 2016.
- [29] Z. Li *et al.*, "SSBI Mitigation and the Kramers-Kronig Scheme in Single-Sideband Direct-Detection Transmission with Receiver-Based Electronic Dispersion Compensation," in *Journal of Lightwave Technology*, vol. 35, no. 10, pp. 1887-1893, 2017.

- [30] Rongqing Hui and Maurice O’Sullivan, *Fiber Optic Measurement Techniques*, by Academic Press, 2009, (ISBN-978-0-12-373865-3).
- [31] Rongqing Hui, *Introduction to Fiber-Optic Communications*, by Academic Press, 2019, (ISBN- 9780128053454).
- [32] B. J. C. Schmidt, A. J. Lowery and J. Armstrong, “Experimental Demonstrations of Electronic Dispersion Compensation for Long-Haul Transmission Using Direct-Detection Optical OFDM,” in *Journal of Lightwave Technology*, vol. 26, no. 1, pp. 196-203, 2008.
- [33] A. H. Gnauck and P. J. Winzer, "Optical phase-shift-keyed transmission," in *Journal of Lightwave Technology*, vol. 23, no. 1, pp. 115-130, 2005.
- [34] S. Chandrasekhar and X. Liu, “Enabling components for future highspeed coherent communication systems,” in *Proc. of OFC*, 2011, Paper OMU5.
- [35] M. S. Faruk and S. J. Savory, "Digital Signal Processing for Coherent Transceivers Employing Multilevel Formats," in *Journal of Lightwave Technology*, vol. 35, no. 5, pp. 1125-1141, 2017.
- [36] M. P. Yankov, D. Zibar, K. J. Larsen, L. P. B. Christensen and S. Forchhammer, "Constellation Shaping for Fiber-Optic Channels with QAM and High Spectral Efficiency," in *IEEE Photonics Technology Letters*, vol. 26, no. 23, pp. 2407-2410, 2014.
- [37] T. Fehenberger, A. Alvarado, G. Böcherer and N. Hanik, "On Probabilistic Shaping of Quadrature Amplitude Modulation for the Nonlinear Fiber Channel," in *Journal of Lightwave Technology*, vol. 34, no. 21, pp. 5063-5073, 2016.
- [38] Junwen Zhang, Jianjun Yu, Nan Chi, and Hung-Chang Chien, "Time-domain digital pre-equalization for band-limited signals based on receiver-side adaptive equalizers," in *Opt. Express*, vol. 22, no. 17, pp. 20515-20529, 2014.
- [39] P. W. Berenguer *et al.*, "Nonlinear Digital Pre-distortion of Transmitter Components," in *Journal of Lightwave Technology*, vol. 34, no. 8, pp. 1739-1745, 2016.
- [40] A. Napoli *et al.*, "Digital Compensation of Bandwidth Limitations for High-Speed DACs and ADCs," in *Journal of Lightwave Technology*, vol. 34, no. 13, pp. 3053-3064, 2016.
- [41] C. Laperle and M. O’Sullivan, "Advances in High-Speed DACs, ADCs, and DSP for Optical Coherent Transceivers," in *Journal of Lightwave Technology*, vol. 32, no. 4, pp. 629-643, 2014.
- [42] Seb J. Savory, “Digital coherent optical receivers: algorithms and subsystems,” in *IEEE Journal of Selected Topics in Quantum Electronics*, vol. 16, no. 5, pp. 1164-1179, 2010.
- [43] T. Tanimura, S. Oda, T. Tanaka, T. Hoshida, Z. Tao, and J. Rasmussen, “A simple digital skew compensator for coherent receiver,” in *Proc. Eur. Conf. Opt. Commun.*, Sep. 2009, paper 7.3.2.
- [44] E. M. Ip and J. M. Kahn, "Fiber Impairment Compensation Using Coherent Detection and Digital Signal Processing," in *Journal of Lightwave Technology*, vol. 28, no. 4, pp. 502-519, 2010.
- [45] I. Fatadin, D. Ives and S. J. Savory, "Compensation of Frequency Offset for Differentially Encoded 16- and 64-QAM in the Presence of Laser Phase Noise," in *IEEE Photonics Technology Letters*, vol. 22, no. 3, pp. 176-178, 2010.
- [46] R. Koma, M. Fujiwara, R. Igarashi, T. Kanai, J. Kani and A. Otaka, "Wide Range Carrier Frequency Offset Estimation Method using Training Symbols with Asymmetric Constellations for

Burst-Mode Coherent Reception," in *Optical Fiber Communications Conference and Exposition (OFC)*, 2018, paper M3B.5.

[47] Meng Qiu, Qunbi Zhuge, Xian Xu, Mathieu Chagnon, Mohamed Morsy-Osman, and David V. Plant, "Simple and efficient frequency offset tracking and carrier phase recovery algorithms in single carrier transmission systems," in *Opt. Express*, vol. 21, no. 7, pp. 8157-8165, 2013.

[48] Jianing Lu, Xiang Li, Songnian Fu, Ming Luo, Meng Xiang, Huibin Zhou, Ming Tang, and Deming Liu, "Joint carrier phase and frequency-offset estimation with parallel implementation for dual-polarization coherent receiver," in *Opt. Express*, vol. 25, no. 5, pp. 5217-5231, 2017.

[49] OIF-ITLA-MSA-01.1, Integrable Tunable Laser Assembly MSA, Optical internetworking forum (OIF), 2005.

[50] A. F. Elrefaie, R. E. Wagner, D. A. Atlas and D. G. Daut, "Chromatic dispersion limitations in coherent lightwave transmission systems," in *Journal of Lightwave Technology*, vol. 6, no. 5, pp. 704-709, 1988.

[51] A. F. Elrefaie and R. E. Wagner, "Chromatic dispersion limitations for FSK and DPSK systems with direct detection receivers," in *IEEE Photonics Technology Letters*, vol. 3, no. 1, pp. 71-73, 1991.

[52] Y. Zhu, K. Zou, X. Ruan and F. Zhang, "Single Carrier 400G Transmission with Single-Ended Heterodyne Detection," in *IEEE Photonics Technology Letters*, vol. 29, no. 21, pp. 1788-1791, 2017.

[53] M. S. Erkilinc *et al.*, "Spectrally Efficient WDM Nyquist Pulse-Shaped 16-QAM Subcarrier Modulation Transmission with Direct Detection," in *Journal of Lightwave Technology*, vol. 33, no. 15, pp. 3147-3155, 2015.

[54] S. T. Le *et al.*, "1.72-Tb/s Virtual-Carrier-Assisted Direct-Detection Transmission Over 200 km," in *Journal of Lightwave Technology*, vol. 36, no. 6, pp. 1347-1353, 2018.

[55] B. J. C. Schmidt, A. J. Lowery and L. B. Du, "Low Sample Rate Transmitter for Direct-Detection Optical OFDM," *2009 Conference on Optical Fiber Communication - includes post deadline papers*, 2009, paper OWM4.

[56] X. Chen *et al.*, "Kramers–Kronig Receivers for 100-km Datacenter Interconnects," in *Journal of Lightwave Technology*, vol. 36, no. 1, pp. 79-89, 2018.

[57] C. Füllner *et al.*, "Complexity Analysis of the Kramers–Kronig Receiver," in *Journal of Lightwave Technology*, vol. 37, no. 17, pp. 4295-4307, 2019.

[58] Tianwai Bo and Hoon Kim, "Kramers-Kronig Receiver Operable Without Digital Upsampling," in *Optics Express*, vol. 26, no. 11, pp. 13810-13818, 2018.

[59] T. Bo and H. Kim, "Toward Practical Kramers-Kronig Receiver: Resampling, Performance, and Implementation," in *Journal of Lightwave Technology*, vol. 37, no. 2, pp. 461-469, 2019.

[60] J. L. Gimlett and N. K. Cheung, "Effects of phase-to-intensity noise conversion by multiple reflections on gigabit-per-second DFB laser transmission systems," in *Journal of Lightwave Technology*, vol. 7, no. 6, pp. 888-895, 1989.

[61] T. Okoshi, K. Kikuchi, and A. Nakayama, "Novel Method for High Resolution Measurement of Laser Output Spectrum," in *Electronics Letters*, vol. 16, no. 16, pp. 630-631, 1980.

- [62] Moshe Nazarathy, Wayne V. Sorin, Douglas M. Baney, and Steven A. Newton, "Spectral Analysis of Optical Mixing Measurements," in *Journal of Lightwave Technology*, vol. 7, no. 7, pp. 1083-1096, 1989.
- [63] Thomas Duthel, Georg Clarici, Chris R. S. Fludger, Jonas C. Geyer, Christoph Schulien, and Stefan Wiese, "Laser Linewidth Estimation by Means of Coherent Detection," in *IEEE Photonics Technology Letters*, vol. 21, no. 20, pp. 1568-1570, 2009.
- [64] Kazuro Kikuchi, "Characterization of semiconductor-laser phase noise and estimation of bit-error rate performance with low-speed offline digital coherent receivers," in *Opt. Express*, vol. 20, no. 5, pp. 5291-5302, 2012.
- [65] D. Lavery, S. Erkilinc, P. Bayvel and R. I. Killey, "Recent Progress and Outlook for Coherent PON," *2018 Optical Fiber Communications Conference and Exposition (OFC)*, 2018, paper M3B.1.
- [66] M. S. Erkilinc *et al.*, "Comparison of Low Complexity Coherent Receivers for UDWDM-PONs (λ -to-the-User)," in *Journal of Lightwave Technology*, vol. 36, no. 16, pp. 3453-3464, 2018.
- [67] J. Cheng, C. Xie, Y. Chen, X. Chen, M. Tang, and S. Fu, "Comparison of Coherent and IMDD Transceivers for Intra Datacenter Optical Interconnects," in *Optical Fiber Communication Conference (OFC)*, 2019, paper W1F.2.
- [68] M. Seimetz, "Laser Linewidth Limitations for Optical Systems with High Order Modulation Employing Feed Forward Digital Carrier Phase Estimation," in *Optical Fiber Communication Conference (OFC)*, 2008, paper OTuM2.
- [69] M. G. Taylor, "Phase Estimation Methods for Optical Coherent Detection Using Digital Signal Processing," in *Journal of Lightwave Technology*, vol. 27, no. 7, pp. 901-914, 2009.
- [70] I. Fatadin, D. Ives and S. J. Savory, "Carrier Phase Recovery for 16-QAM Using QPSK Partitioning and Sliding Window Averaging," in *IEEE Photonics Technology Letters*, vol. 26, no. 9, pp. 854-857, 2014.
- [71] X. Zhou, "An Improved Feed-Forward Carrier Recovery Algorithm for Coherent Receivers With M -QAM Modulation Format," in *IEEE Photonics Technology Letters*, vol. 22, no. 14, pp. 1051-1053, 2010.
- [72] X. Li, Y. Cao, S. Yu, W. Gu and Y. Ji, "A Simplified Feedforward Carrier Recovery Algorithm for Coherent Optical QAM System," in *Journal of Lightwave Technology*, vol. 29, no. 5, pp. 801-807, 2011.
- [73] J. Li, L. Li, Z. Tao, T. Hoshida and J. C. Rasmussen, "Laser-Linewidth-Tolerant Feed-Forward Carrier Phase Estimator with Reduced Complexity for QAM," in *Journal of Lightwave Technology*, vol. 29, no. 16, pp. 2358-2364, 2011.
- [74] M. Magarini *et al.*, "Pilot-Symbols-Aided Carrier-Phase Recovery for 100-G PM-QPSK Digital Coherent Receivers," in *IEEE Photonics Technology Letters*, vol. 24, no. 9, pp. 739-741, 2012.
- [75] S. M. Bilal, C. R. S. Fludger and G. Bosco, "Multi-stage CPE algorithms for 64-QAM constellations," in *Optical Fiber Communication Conference (OFC)*, 2014, paper M2A.8.

- [76] S. M. Bilal, G. Bosco, J. Cheng, A. P. T. Lau and C. Lu, "Carrier Phase Estimation Through the Rotation Algorithm for 64-QAM Optical Systems," in *Journal of Lightwave Technology*, vol. 33, no. 9, pp. 1766-1773, 2015.
- [77] Mustafa AL-QADI, Govind Vedala, and Rongqing Hui, "Performance of Lasers with Excess Low-Frequency FM-Noise Profiles in Digital Coherent Optical Systems," in *Optical Fiber Communication Conference (OFC)*, 2019, paper W4B.3.
- [78] Govind Vedala, Mustafa AL-QADI, Maurice O'Sullivan, John Cartledge, and Rongqing Hui, "Phase Noise Characterization of a QD-Based Diode Laser Frequency Comb," in, vol. 25, no. 14, pp. 15890-15904, 2017.
- [79] Mustafa AL-QADI, Govind Vedala, and Rongqing Hui, "Phase Noise of Diode Laser Frequency Comb and its Impact in Coherent Communication Systems," in *Conference on Lasers and Electro-Optics (CLEO)*, 2018, paper JTu2A.35.
- [80] Tam N. Huynh, Seán P. Ó Dúill, Lim Nguyen, Leslie A. Rusch, and Liam P. Barry, "Simple Analytical Model for Low-Frequency Frequency-Modulation Noise of Monolithic Tunable Lasers," in *Applied Optics*, vol. 53, no. 5, pp. 830-835, 2014.
- [81] Tam N. Huynh, L. Nguyen and L. P. Barry, "Phase Noise Characterization of SGDBR Lasers Using Phase Modulation Detection Method with Delayed Self-Heterodyne Measurements," in *Journal of Lightwave Technology*, vol. 31, no. 8, pp. 1300-1308, 2013.
- [82] Mustafa AL-QADI, Maurice O'Sullivan, Chongjin Xie, and Rongqing Hui, "Differential Phase Noise Properties in QD-MLL and its Performance in Coherent Transmission Systems," in *Conference on Lasers and Electro-Optics (CLEO)*, 2019, San Jose, CA, paper SW3O.2.
- [83] Gianni Di Domenico, Stéphane Schilt, and Pierre Thomann, "Simple Approach to the Relation Between Laser Frequency Noise and Laser Line Shape," in *Applied Optics*, vol. 49, no. 25, pp. 4801-4807, 2010.
- [84] Nikola Bucalovic *et al.*, "Experimental validation of a simple approximation to determine the linewidth of a laser from its frequency noise spectrum," in *Appl. Opt.*, vol. 51, pp. 4582-4588, 2012.
- [85] Qian Zhou, Jie Qin, Weilin Xie, Zhangweiyi Liu, Yitian Tong, Yi Dong, and Weisheng Hu, "Power-area method to precisely estimate laser linewidth from its frequency-noise spectrum," in *Appl. Opt.* vol. 54, pp. 8282-8289, 2015.
- [86] Rongqing Hui and Maurice O'Sullivan, "Characterization of optical devices," in *Fiber Optic Measurement Techniques*, Burlington, MA, USA: Academic Press, 2009, pp. 259-276.
- [87] Robert Maher and Benn Thomsen, "Dynamic linewidth measurement technique using digital intradyne coherent receivers," in *Optics Express*, vol. 19, no. 26, pp. B313-B322, 2011.
- [88] Z.G. Lu, J.R. Liu, S. Raymond, P.J. Poole, P.J. Barrios, and D. Poitras, "312-fs Pulse Generation from a Passive C-Band InAs/InP Quantum Dot Mode-Locked Laser," in *Optics Express*, vol. 16, no. 14, pp. 10835-10840, 2008.
- [89] Alvaro Moscoso-Mártir, et al., "8-channel WDM Silicon Photonics Transceiver with SOA and Semiconductor Mode-Locked Laser," in *Optics Express*, vol. 26, no. 19, pp. 25446-25459, 2018.

- [90] J. N. Kemal *et al.*, "32QAM WDM transmission using a quantum-dash passively mode-locked laser with resonant feedback," in *Optical Fiber Communications Conference and Exhibition (OFC)*, Los Angeles, CA, 2017, paper TH5C.3.
- [91] N. Eiselt, *et al.*, "Real-Time 200 Gb/s (4×56.25 Gb/s) PAM-4 Transmission over 80 km SSMF using Quantum-Dot Laser and Silicon Ring-Modulator," in *Optical Fiber Communication Conference (OFC)*, 2017, paper W4D.3.
- [92] J. N. Kemal *et al.*, "WDM transmission using quantum-dash mode-locked laser diodes as multi-wavelength source and local oscillator," in *Optical Fiber Communications Conference and Exhibition (OFC)*, 2017, paper Th3F.6.
- [93] M. AL-QADI, G. Vedala, M. O'Sullivan, C. Xie and R. Hui, "QD-MLL-Based Single-Sideband Superchannel Generation Scheme with Kramers–Kronig Direct Detection Receivers," in *IEEE Photonics Journal*, vol. 11, no. 4, pp. 1-13, 2019.
- [94] K. Sam Shanmugan and Arthur M. Breipohl, *Random Signals: Detection, Estimation and Data Analysis*, Wiley Publications, 1988.
- [95] H. Cramér, *Mathematical Methods of Statistics*. Princeton University Press, Mar. 23, 1999.
- [96] F. Rice, B. Cowley, B. Moran and M. Rice, "Cramér-Rao lower bounds for QAM phase and frequency estimation," in *IEEE Transactions on Communications*, vol. 49, no. 9, pp. 1582-1591, 2001.
- [97] E. Maniloff, S. Gareau, and M. Moyer, "400G and Beyond: Coherent Evolution to High-Capacity Inter Data Center Links," in *Optical Fiber Communication Conference (OFC) 2019*, paper M3H.4.
- [98] J. Cheng, C. Xie, M. Tang, and S. Fu, "A Low-Complexity Adaptive Equalizer for Digital Coherent Short-Reach Optical Transmission Systems," in *Optical Fiber Communication Conference (OFC) 2019*, paper M3H.2.
- [99] J. K. Perin, A. Shastri and J. M. Kahn, "Design of Low-Power DSP-Free Coherent Receivers for Data Center Links," in *Journal of Lightwave Technology*, vol. 35, no. 21, pp. 4650-4662, 2017.
- [100] Ali Shahpari, Ricardo M. Ferreira, Ruben S. Luis, Zoran Vujicic, Fernando P. Guiomar, Jacklyn D. Reis, and António L. Teixeira, "Coherent Access: A Review," in *Journal of Lightwave Technology*, vol. 35, pp. 1050-1058, 2017.
- [101] Q. Zhou, J. He, S. Shen, R. Zhang, S. Yao, Y. Alfadhli, Y. Chen, and G. Chang, "Symmetric Long-Reach 16-QAM Transmission using Lite Coherent Receiver for Next-Generation Optical Access Network," in *Optical Fiber Communication Conference (OFC) 2019*, paper Th2A.29.
- [102] Z. G. Lu, J. R. Liu, C. Y. Song, J. Weber, Y. Mao, S. D. Chang, H. P. Ding, P. J. Poole, P. Barrios, D. Poitras, S. Janz, and M. O'Sullivan, "An InAs/InP quantum dot C-band coherent comb laser," in *Optical Fiber Communication Conference (OFC)*, 2018, paper Th1I.4.
- [103] V. Vujicic *et al.*, "Quantum Dash Mode-Locked Lasers for Data Centre Applications," in *IEEE Journal of Selected Topics in Quantum Electronics*, vol. 21, no. 6, pp. 53-60, Art no. 1101508.

- [104] K. Zanette, J. C. Cartledge, R. Hui and M. O'Sullivan, "Phase Noise Characterization of a Mode-Locked Quantum-Dot Coherent Optical Frequency Comb Source Laser," *Optical Fiber Communications Conference (OFC)*, 2018, paper Th2A.17.
- [105] J. Pfeifle *et al.*, "Simultaneous Phase Noise Reduction of 30 Comb Lines from a Quantum-Dash Mode-Locked Laser Diode Enabling Coherent Tbit/s Data Transmission," in *Optical Fiber Communication Conference (OFC)*, 2015, paper Tu3I.5.
- [106] Z. G. Lu, J. R. Liu, P. J. Poole, C. Y. Song, and S. D. Chang, "Ultra-narrow linewidth quantum dot coherent comb lasers," in *Optical Fiber Communication Conference (OFC)*, 2018, paper Th1I.5.
- [107] K. Zanette, J. C. Cartledge, and M. O'Sullivan, "Correlation properties of the phase noise between pairs of lines in a quantum-dot optical frequency comb source," in *Optical Fiber Communications Conference (OFC)*, 2017, paper Th3I.6.
- [108] H. Tsuchida, "Wideband phase-noise measurement of mode-locked laser pulses by a demodulation technique," in *Optics Letters*, vol. 23, no. 4, pp. 286-288, 1998.
- [109] A. Finch, X. Zhu, P. N. Kean, W. Sibbett, "Noise Characterization of Mode-Locked Color-Center Laser Sources," in *IEEE J. Quantum Electronics*, vol. 26, no. 6, pp. 1115-1123, 1990.
- [110] T. Habruseva, S. O'Donoghue, N. Rebrova, F. K  f  lian, S. P. Hegarty, and G. Huyet, "Optical linewidth of a passively mode-locked semiconductor laser," in *Optics Letters*, vol. 34, no. 21, pp. 3307-3309, 2009.
- [111] R. Watts, R. Rosales, F. Lelarge, A. Ramdane, and L. Barry, "Mode coherence measurements across a 1.5 THz spectral bandwidth of a passively mode-locked quantum dash laser," in *Optics Letters*, vol. 37, no. 9, pp. 1499-1501, 2012.
- [112] A. Klee, J. Davila-Rodriguez, C. Williams, and P. J. Delfyett, "Characterization of Semiconductor-Based Optical Frequency Comb Sources Using Generalized Multiheterodyne Detection," in *IEEE J. Sel. Top. Quantum Electron.*, vol. 19, no. 4, paper 1100711, 2013.
- [113] A. Klee, J. Davila-Rodriguez, C. Williams, and P. J. Delfyett, "Generalized Spectral Magnitude and Phase Retrieval Algorithm for Self-Referenced Multiheterodyne Detection," in *J. Lightwave Technologies*, vol. 30, no. 23, pp. 3758-3764, 2013.
- [114] R. Rosales, K. Merghem, A. Martinez, F. Lelarge, A. Accard, and A. Ramdane, "Timing jitter from the optical spectrum in semiconductor passively mode locked lasers," in *Opt. Express*, vol. 20, no. 8, pp. 9151–9160, 2012.
- [115] R. Paschotta, "Noise of mode-locked lasers (Part II): and other fluctuations," *Appl. Phys. B*, vol. 79, no. 2, pp. 163–173, 2004.
- [116] I. Coddington, N. Newbury, and W. Swann, "Dual-comb spectroscopy," in *Optica*, vol. 3, no. 4, pp. 414–426, 2016.
- [117] J. Li, X. Zhang, F. Tian, and L. Xi, "Theoretical and experimental study on generation of stable and high-quality multi-carrier source based on re-circulating frequency shifter used for Tb/s optical transmission," in *Opt. Express*, vol. 19, no. 2, pp. 848–860, 2011.
- [118] D. von der Linde, "Characterization of the noise in continuously operating mode-locked lasers," in *Appl. Phys. B*, vol. 39, no. 4, pp. 201–217, 1986.

- [119] X. Chen *et al.*, "218-Gb/s single-wavelength, single-polarization, single photodiode transmission over 125-km of standard single mode fiber using Kramers-Kronig detection," in *Proc. Opt. Fiber Commun. Conf. (OFC)*, 2017, Paper Th5B.6.
- [120] X. Liu and S. Chandrasekhar, "Superchannel for Next-Generation Optical Networks," in *Optical Fiber Communication Conference (OFC)*, 2014, paper W1H.5.
- [121] S. T. Le, K. Schuh and H. Nguyen Tan, "A Closed-Form Expression for Direct Detection Transmission Systems with Kramers-Kronig Receiver," in *IEEE Photonics Technology Letters*, vol. 30, no. 23, pp. 2048-2051, 2018.
- [122] Mark A. Foster, Jacob S. Levy, Onur Kuzucu, Kasturi Saha, Michal Lipson, and Alexander L. Gaeta, "Silicon-based monolithic optical frequency comb source," in *Optics Express*, vol. 19, pp. 14233-14239, 2011.
- [123] Brian R. Washburn, Scott A. Diddams, Nathan R. Newbury, Jeffrey W. Nicholson, Man F. Yan, and Carsten G. Jorgensen, "Phase-locked, erbium-fiber-laser-based frequency comb in the near infrared," in *Optics Letters*, vol. 29, pp. 250-252, 2004.
- [124] S. Cao, J. Chen, J. N. Damask, C. R. Doerr, L. Guiziou, G. Harvey, Y. Hibino, H. Li, S. Suzuki, K.-Y. Wu, and P. Xie, "Interleaver technology comparisons and applications requirements," in *J. of Light. Tech.*, vol. 22, no. 1, pp. 281-289, 2004.
- [125] Huai-Wei Lu, Kai-Jun Wu, Yun Wei, Bao-Ge Zhang, Guan-Wei Luo, "Study of all-fiber asymmetric interleaver based on two-stage cascaded Mach-Zehnder Interferometer," in *Optics Communications*, vol. 285, no. 6, pp. 1118-1122, 2012.
- [126] An example commercial product specification may be found online:
http://www.optoplex.com/Asymmetric_Interleaver.htm.
- [127] Lian-Wee Luo, Salah Ibrahim, Arthur Nitkowski, Zhi Ding, Carl B. Poitras, S. J. Ben Yoo, and Michal Lipson, "High bandwidth on-chip silicon photonic interleaver," in *Optics Express*, vol. 18, pp. 23079-23087, 2010.
- [128] M. Zhang, C. Wang, Xi Chen, M. Bertrand, A. Shams-Ansari, S. Chandrasekhar, P. Winzer, and M. Loncar, "Ultra-High Bandwidth Integrated Lithium Niobate Modulators with Record-Low $V\pi$," in *Optical Fiber Comm. Conf. (OFC)*, 2018, paper Th4A.5.
- [129] H. Park, A. W. Fang, O. Cohen, R. Jones, M. J. Paniccia and J. E. Bowers, "A Hybrid AlGaInAs-Silicon Evanescent Amplifier," in *IEEE Photonics Technology Letters*, vol. 19, no. 4, pp. 230-232, 2007.
- [130] Kasper Van Gasse, Ruijun Wang, and Gunther Roelkens, "27 dB gain III-V-on-silicon semiconductor optical amplifier with > 17 dBm output power," in *Optics Express*, vol. 27, pp. 293-302, 2019.
- [131] X. Chen *et al.*, "4 \times 240 Gb/s Dense WDM and PDM Kramers-Kronig Detection with 125-km SSMF Transmission," in *European Conference on Optical Communication (ECOC)*, 2017, pp. 1-3.
- [132] X. Chen, S. Chandrasekhar, S. Olsson, A. Adamiecki and P. Winzer, "Impact of O/E Front-End Frequency Response on Kramers-Kronig Receivers and its Compensation," in *European Conf. on Optical Comm. (ECOC)*, 2018, pp. 1-3.

- [133] Z. Li *et al.*, "Joint optimisation of resampling rate and carrier-to-signal power ratio in direct-detection Kramers-Kronig receivers," in *European Conference on Optical Communication (ECOC)*, 2017, pp. 1-3.
- [134] M. J. Connelly, *Semiconductor Optical Amplifiers*. Springer Science, New York, 2002.
- [135] Niloy K. Dutta and Qiang Wang, *Semiconductor Optical Amplifiers*, 2nd Edition, World Scientific Publishing, NJ, 2013.
- [136] J. Renaudier *et al.*, "First 100-nm continuous-band WDM transmission system with 115Tb/s transport over 100 km using novel ultra-wideband semiconductor optical amplifiers," in *Proc. Eur. Conf. Opt. Comm. (ECOC)*, 2017, paper Th.PDP.A3.
- [137] A. Ghazisaeidi, "Theory of Coherent WDM Systems Using In-Line Semiconductor Optical Amplifiers," in *Journal of Lightwave Technology*, vol. 37, no. 17, pp. 4188-4200, 2019.
- [138] T. Akiyama *et al.*, "An ultrawide-band (120 nm) semiconductor optical amplifier having an extremely-high penalty-free output power of 23 dBm realized with quantum-dot active layers," *Proc. Opt. Fiber Commun. Conf. (OFC)*, 2004, paper PDP12.
- [139] E. Desurvire, *Erbium-Doped Fiber Amplifiers: Principles and Applications*. Hoboken, NJ, USA: Wiley, 1992.
- [140] M. Alvaro *et al.*, "Silicon Photonics Transmitter with SOA and Semiconductor Mode-Locked Laser," *Scientific Reports*, vol. 7, Article number 13857, 2017.
- [141] A. Mecozzi and J. Mørk, "Saturation induced by picosecond pulses in semiconductor optical amplifiers," in *Journal of the Optical Society of America B*, vol. 14, no. 4, pp. 761-770, 1997.
- [142] A. V. Uskov, *et al.*, "On ultrafast optical switching based on quantum-dot semiconductor optical amplifiers in nonlinear interferometers," in *IEEE Ph. Tech. Letters*, vol. 16, no. 5, pp. 1265-1267, 2004.
- [143] K. Sato and H. Toba, "Reduction of mode partition noise by using semiconductor optical amplifiers," in *IEEE J. Sel. Top. Quantum Electron.*, vol. 7, no. 2, pp. 328-333, 2001.
- [144] M. Gay *et al.*, "Single Quantum Dash mode-locked laser as a comb generator in four-channel 112 Gbit/s WDM transmission," in *Proc. Optical Fiber Communication Conf. (OFC)*, 2014, paper Tu2H.
- [145] J. C. Cartledge and M. O'Sullivan, "Time- and Frequency-Domain Characterization of the Relative Intensity Noise of a Quantum-Dot Frequency Comb Source Laser," in *IEEE J. of Sel. Topics in Quantum Elect.*, vol. 25, no. 6, pp. 1-9, 2019.
- [146] Q. T. Nguyen *et al.*, "Bidirectional 2.5-Gb/s WDM-PON Using FP-LDs Wavelength-Locked by a Multiple-Wavelength Seeding Source Based on a Mode-Locked Laser," in *IEEE Photonics Technology Letters*, vol. 22, no. 11, pp. 733-735, 2010.
- [147] Bo Zhang, Christian Malouin, and Theodore J. Schmidt, "Design of coherent receiver optical front end for unamplified applications," in *Opt. Express*, vol. 20, no. 3, pp. 3225-3234, 2012.
- [148] G. P. Agrawal and N. A. Olsson, "Self-phase modulation and spectral broadening of optical pulses in semiconductor laser amplifiers," in *IEEE J. of Q. Elect.*, vol. 25, no. 11, pp. 2297-2306, 1989.

- [149] X. Li and G. Li, "Joint fiber and SOA impairment compensation using digital backward propagation," in *IEEE Photon. J.*, vol. 2, no. 5, pp. 753–758, 2010.
- [150] M. Sieben, J. Conradi and D. E. Dodds, "Optical single sideband transmission at 10 Gb/s using only electrical dispersion compensation," in *Journal of Lightwave Technology*, vol. 17, no. 10, pp. 1742-1749, 1999.